Title
Integration of Advanced Diffusion Acquisition and Analysis Techniques to Improve Treatment Management of Brain Tumor

Author
Wen, Qiuting

Publication Date
2015

Peer reviewed|Thesis/dissertation

INTEGRATION OF ADVANCED DIFFUSION ACQUISITION AND ANALYSIS TECHNIQUES TO IMPROVE TREATMENT MANAGEMENT OF BRAIN TUMOR

by

Qiuting Wen

DISSERTATION

Submitted in partial satisfaction of the requirements for the degree of

DOCTOR OF PHILOSOPHY

in

Bioengineering

in the

GRADUATE DIVISION

of the

UNIVERSITY OF CALIFORNIA, SAN FRANCISCO

AND

UNIVERSITY OF CALIFORNIA, BERKELEY

Dedicated to My Parents

Jie Liu and Changhong Wen

ACKNOWLEDGEMENT

Above all, to Sarah Nelson, for opening the door of Magnetic Resonance Imaging to me and offering me the opportunity to study in her laboratory, for being such a wonderful mentor with endless guidance, patience, support and encouragement over the years, which have allowed me to grow as both a researcher and an individual.

To Susan Chang for being on my qualifying exam my thesis committees, for explaining to me challenges in MRI from a clinical perspective and providing valuable feedback on my thesis.

To Chris Hess for being on my thesis committee, helping me understand both clinical and technical problems in diffusion imaging, and providing great help and support in hunting for my post-doc position.

To Duan Xu for being on my qualifying exam committee, and for valuable discussions with me throughout the years and always quickly responding to my questions and emails.

To Xiaojuan Li and Steve Connolly for being on my qualifying exam committee and offering so much good advice when I first started my PhD.

To John Kurhanewicz for being my graduate advisor and teaching me spectroscopy.

To Janine Lupo for being the “speak-to” person whenever I needed help with my projects and for all her great advice that spans the entire thesis.

To Yan Li, Maryam Vareth and Wei Bian for the useful discussions about research and course work, their friendship, continual support and encouragement all along.

To Angela Jakary for always being willing to help in scanning and proofreading, for being such a good collaborator in the depression study, and for her warm greetings everyday.

To Douglas Kelley and Suchandrima Banerjee for their engineering expertise and in-depth discussions on the multiband project.

To Jason Crane and Beck Olson for their ingenuity in building the software tools and their patience and helpfulness in debugging software with me throughout these projects.

To Emma Essock-Burns, Ilwoo Park, Eugene Ozhinsky, Adam Elkhaled and Trey Jalbert for being wonderful lab-mates and for their valuable inputs in different aspects of my projects.

To Chris Williams, Sana Vaziri, Marisa Lafontaine, Evan Neill, Manisha Dayal, Wendy Ma and Shauna O'Donnell for their help with patient scans, post-processing and patient consenting.

To Annette Molinaro for her rigorous yet practical statistical models for analyzing clinical data.

To Joanna Philips for her expertise on tumor pathology and for helping me to better understand tumor biology.

To Mary McPolin, Allison Fuller and Bert Jimenez for their great help in the scanner room.

To my parents Jie Liu and Changhong Wen for their unconditional love and support throughout my years, and giving me great guidance for making critical decisions in my life.

To my husband Mengshi Lu for being there for me all the time and always making my laugh.

To my daughter Yihan Emma Lu for being such an angel and making me proud of being her mom.

THANK YOU ALL SINCERELY!

This work was supported by grants from the National Institutes of Health R01CA127612, P01 CA118816, R01HD072074, EB009756 in conjunction with GE Healthcare.

ABSTRACT

Diffusion MRI is a technique that is capable of providing unique contrast that is sensitive to molecular displacement motion at cellular and sub-cellular length scales. By sensitizing MR signal to the random motion of water molecule protons at a microscopic level (of the order of 5–20μm), it is able to probe tissue microstructures in the brain such as axons, dendrites, glial cells, and extra-cellular spaces, in a manner that may provide valuable insights into tumor physiology.

Diffusion imaging is routinely acquired as part of the MR protocol for patients with brain tumors. However, the implications of the parameters being used are often not appreciated by the oncology community. This is especially true when applied to patients with high-grade glioma, where the lesion is highly heterogeneous and changes in diffusion parameters are due to a combination of treatment effects, edema and tumor infiltration. Although advanced diffusion models that aim to distinguish between different types of tissue have the potential for providing information that is complementary to conventional MR imaging, their application has been very limited due to their relatively long acquisition time.

These challenges have become the motivation for this thesis. We first explored the value of standard diffusion imaging methods in characterizing tumor response to therapy. By applying different ways of evaluating changes in the apparent diffusion coefficient (ADC) and examining their association with patient outcomes in clinical trials, we hoped to gain a better understanding of the physiological process behind the patterns of changes that occur, and improve the interpretation of the data obtained. The next step was to bridge the gap between advanced diffusion models and their clinical applications by using fast diffusion imaging techniques. This was achieved by optimizing the protocol for acquiring multiband diffusion data at 7T and the post-processing pipeline for such data. The quality of the 7T multiband data was evaluated qualitatively and quantitatively in comparison with data obtained at 3T. The acquisition of

multiband two shell diffusion data allowed us to apply neurite orientation dispersion and density imaging (NODDI) to patients with glioma and to evaluate its performance in distinguishing between different types of tissue.

The results of this dissertation suggest that diffusion imaging plays an important role in assessing gliomas. These are very important steps towards improving the assessment of residual disease and distinguishing between tumor and treatment effects for patients with brain tumors.

TABLE OF CONTENTS

LIST OF TABLES

LIST OF FIGURES

PUBLISHED MATERIALS

Chapter 2 is based on the journal article titled “Comparison of ADC metrics and their association with outcome for patients with newly diagnosed glioblastoma being treated with radiation therapy, temozolomide, erlotinib and bevacizumab”, published in Journal of Neuro-Oncology in 2014 with authors: Qiuting Wen, Laleh Jalilian, Janine M. Lupo, Annette M. Molinaro, Susan M. Chang, Jennifer Clarke, Michael Prados, Sarah J. Nelson.

The other material is being prepared for publication but has not yet been accepted.

Chapter 1
Background

This chapter begins by providing an overview of the basic characteristics of primary brain tumors, with a special focus on glioblastoma. A brief review of fundamental MR physics and widely used MR imaging techniques is then presented. Diffusion imaging is introduced in greater detail, including its imaging principles, practical aspects of the basic sequence and major applications in brain tumors.

1.1 Brain Tumor

1.1.1 Structures in the Brain

The major types of cells in the central nervous system (CSN) are: neurons, axons, and glial cells. An understanding of the basic functions of these cells is crucial for understanding the interaction between brain tumor physiology, treatments and changes in the appearance of the lesion on diffusion weighted images. Figure 1-1 shows a schematic representation of the major structures in the cellular network. The neurons are key components for processing and transmitting information by electrical and chemical signaling. They comprise cell bodies, axons and dendrites. The axons are the primary transmission lines that connect different parts of the brain and conduct electrical impulses. Their diameters range from less than 0.2μm to up to 10μm. The majority of axons with diameters greater than 0.2μm are wrapped with an electrical insulating layer called a myelin sheath, which helps to increase the propagation speed of impulses along the axons [1]. When myelin degrades, conduction of signals along the nerve can be impaired or lost. This is the case with certain neurodegenerative disorders such as multiple sclerosis.

Glia cells surround and sheath neuronal cell bodies, axons and synapses throughout the CNS. They make up most of the cells in the brain and can further be separated into (i) Astrocytes,

which maintain homeostasis in the brain by providing neurons with energy and substrates for neurotransmission, (ii) Oligodendrocytes, which form a myelin sheath around axons in the CNS; and (iii) Microglia, which act as the first and main form of active immune defense in the CNS [2].

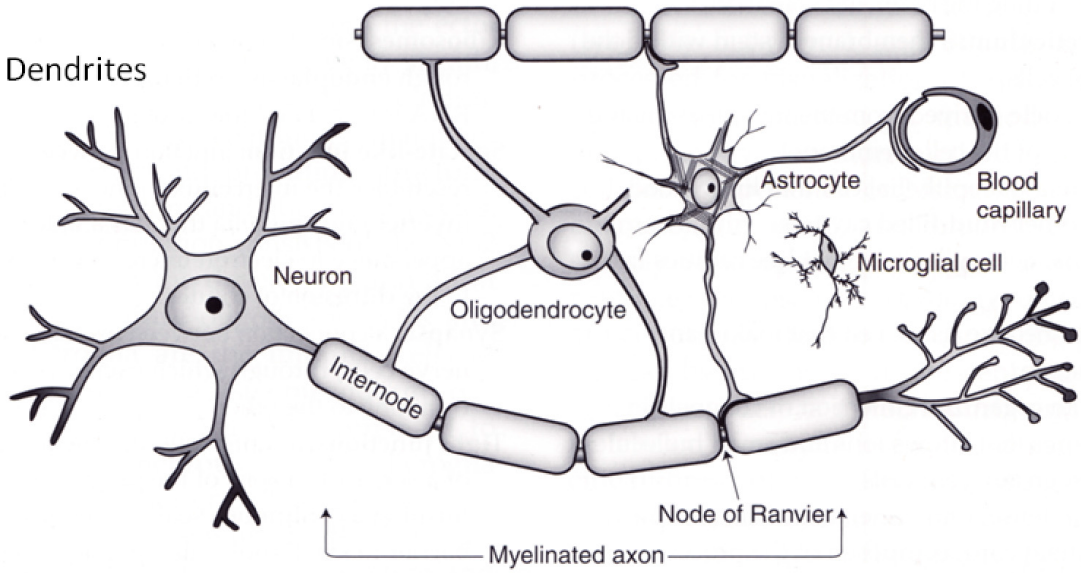

Figure 1-1. Schematic representation of the major cellular elements in the central nervous system (CNS), which include: neurons, axons, myelin sheath and glial cells (Oligodendrocytes, Astrocytes, Microglia). Adapted from Julia M. Edgar IRG 2009.[3]

From a macrostructure view, the brain has three main components: grey matter, white matter and cerebrospinal fluid (CSF). The grey matter or cortex is distributed at the surface of the cerebral hemispheres as well as in the center of the cerebrum. It is composed of neurons, glial cells and capillaries. The white matter contains the majority of myelinated axons. The name 'white' is used because it appears lighter in color due to the fatty myelin sheath. Within white matter tracts, the majority of axons lie parallel to each other (Morell, 1984). CSF is a clear bodily fluid that occupies the ventricular system and surrounds the cortical surface of the brain. Figure 1-2 shows a coronal T_1-weighted MR image with these components labeled.

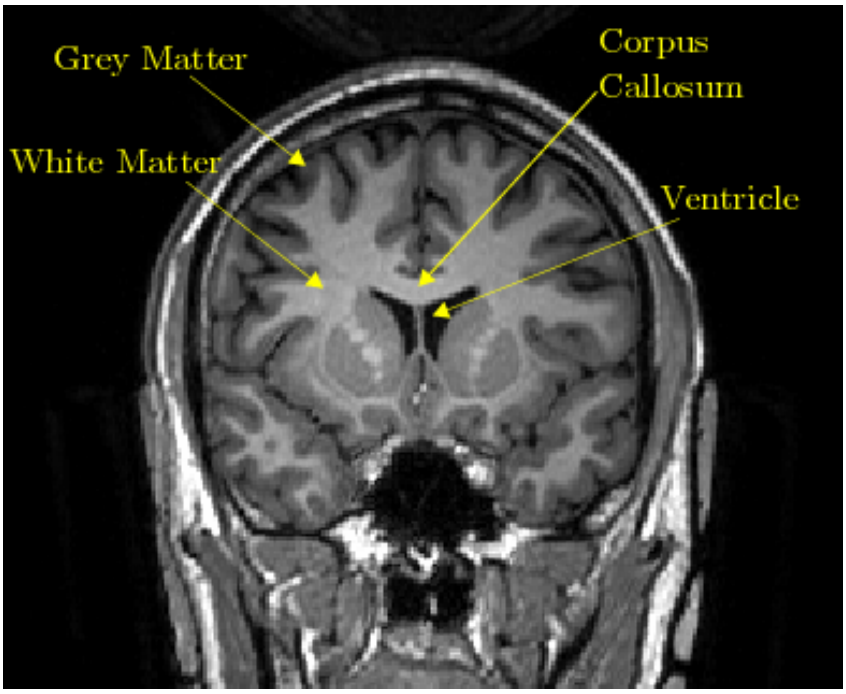

Figure 1-2. A MRI image of brain showing regions of white matter, grey matter, the Ventricles and the Corpus Callosum. The latter is the largest white matter structure in the brain and consists of 200-250 million contralateral axonal projections.

1.1.2 Histologic Features of Gliomas and Grading

It is estimated that seventy percent of the 22,500 malignant primary tumors of the brain and spinal cord that are diagnosed in the United States each year are gliomas [4]. These tumors originate from glial cells and are characterized by the World Health Organization (WHO) criteria on a four-tiered scale. Five histologic features form the basis for this definition: nuclear atypia, cellular density, mitotic activity, endothelial proliferation, and the presence of necrosis [5]. Grade I gliomas are benign and slow-growing, with the best prognosis. They include piliocytic astrocytomas, which most commonly occur in children. Although they are hypercellular, they do not include any of the five features of malignancy. Grade II gliomas are relatively slow growing, but can transform to a higher grade at the time of recurrence. The major sub-types are diffuse astrocytomas, oligodendrogliomas, and oligoastrocytomas. They have moderately increased

cellular density and the presence of nuclear atypia, but lack mitotic activity, necrosis, and endothelial proliferation. Grade III gliomas are considered "high-grade" and have increased mitotic features. Grade IV gliomas are the most malignant subtype, with high cellular density, marked nuclear atypia, elevated mitotic activity, presence of necrosis, and/or endothelial proliferation. The most common sub-type of grade IV glioma are called glioblastoma (GBM). This dissertation is focused primarily on diffusion MR-imaging techniques that aid in the diagnosis and management of GBM.

1.1.3 Treatment of GBM

GBM are aggressively treated with surgery, adjuvant radiation therapy and chemotherapy. Despite advances in care, overall survival (OS) remains limited at approximately 15 months for patients with newly diagnosed lesions [6] and 30 weeks for patients with recurrent GBM [7].

Surgery is the first line of treatment, with the goal of achieving the maximal safe resection of the lesion without causing excessive neurological damage. The extent of resection is typically categorized into gross total resection (GTR), subtotal resection (STR) or biopsy, based upon how much of the Gadolinium enhancing lesion on the T1-weighted images is present in the post-operative scan.

Radiation therapy may be given as a first line treatment, in conjunction with chemotherapy. It works by damaging the DNA of cells and thereby limits their potential for proliferation. The target is typically defined by the anatomical abnormality observed in MR images, plus an additional 2-3cm margin of normal appearing tissue. The standard therapeutic dose for GBM is 60Gy, which is administered in 30-40 fractions in an attempt to avoid neurotoxicity and limit damage to normal tissue. Radiation necrosis is often observed after therapy and makes it extremely difficult to differentiate tumor recurrence from the effect of the treatment itself. Chapter 4 of this thesis will expand on this problem and discuss how advanced MR techniques

(diffusion, perfusion, and spectroscopic imaging) may be able to aid in differentiating between these options. Adding radiotherapy to surgery was shown to increase median survival in patients with newly diagnosed GBM from 3-4 months to 7-12 months [8].

Chemotherapy utilizes agents that have the ability to affect one or more pathways that the tumor utilizes to grow. Examples are the inhibition of protein kinase C activity, tumor angiogenesis, growth factors or tumor invasion. In 2005, it was shown that adding concomitant and adjuvant temozolomide, which is an oral alkylating agent, increased median survival from patients with GBM to 14.6 months compared to 12.1 months with radiotherapy alone [8]. This has become the standard care for GBM. The highly degree of vascularized in GBM and the key role that angiogenesis plays in growth and progression makes disruption of the angiogenic pathway another attractive target for therapeutic intervention.

A variety of intra- and extracellular strategies that disrupt and impede tumor angiogenesis are under investigation [9-11]. These include sequestering circulating VEGF to reduce cell-surface VEGFR activation (bevacizumab, alfibercept), pan-VEGFR tyrosine kinase inhibitors (cediranib), broadspectrum tyrosine kinase inhibitors (sorafenib, sunitnib, XL-184), intracellular protein kinase inhibitors (enzastaurin), and many others. Bevacizumab was successful in receiving accelerated approval from the U.S. Food and Drug Administration (FDA) for use as a single-agent in recurrent glioblastoma patients, based on early evidence of radiographic response [12,13]. This was a key step for integrating antiangiogenic therapy strategies into the clinical care of patients with malignant glioma and raised important clinical questions about how to evaluate response to therapy. In this dissertation, we will discuss a clinical trial that evaluated bevacizumab in patients with newly diagnosed GBM and that demonstrates the potential of using MR diffusion imaging to predict response for these patients.

1.2 Basics of Magnetic Resonance Imaging

The high soft-tissue contrast of MRI is the major diagnostic modality in the evaluation of brain tumors. A brief introduction to the basic principles of MRI is presented here, followed by a description of how it is used routinely in the diagnosis and evaluation of brain tumors.

1.2.1 Spins

The property of Nuclear Magnetic Resonance (NMR) was first described by Rabi in 1938. Purcell and Bloch showed how it could be applied to fluids in 1946 and received the Nobel Prize in Physics for their work in 1952. Since then, NMR has become a powerful tool for chemical and structural analysis of different molecules. In 1973, Lauterbur and Mansfield used the principles of NMR to produce non-invasive images of the body and were awarded the Nobel Prize in Medicine and Physiology in 2003. Over the past 40 years, MRI has become a widely available technology and been applied to address many biomedical, chemical and engineering problems.

The atom is the smallest unit of matter and is composed of a cloud of electrons and a nucleus that is made up of protons and neutrons. An individual unpaired elementary particle (e.g. proton, electron, or neutron) processes an angular momentum or spin of ½ that can be either positive or negative. Nuclei with an odd number of protons and/or neutrons has a non-zero spin and are therefore NMR active. The abundance of the hydrogen atoms (^{1}H) within water protons in the human body has made it the dominant nucleus that is utilized for MRI.

1.2.2 Resonance

In natural environments, a non-zero spin rotates around its own axis creating a microscopic magnetic field, which is called a nuclear magnetic dipole moment and that is randomly oriented. When placed in an external magnetic field B_0, two things happen. The first is that the spins will

process about B_0 with a frequency ω_0 determined by its physical property named gyromagnetic ratio (γ) and the field strength B_0

$$\omega_0 = \gamma B_0 \qquad \text{Eq 1-1}$$

The procession angular frequency ω_0, also called the "Larmor Frequency", which provides the key for creating localization in MRI.

The second thing that happens when the spins are placed in an external magnetic field B_0 is that they will align themselves with the external field B_0 in two possible orientations, parallel (lower energy) or anti-parallel (higher energy). According to the laws of thermodynamics, the number of spins in the lower energy state slightly outnumbers the number of spins in the higher energy state. This small but significant difference is given by Boltzmann statistics by the ratio in Eq 1-2, where N_- and N_+ are the number of spins in the higher and lower energy states respectively, $k = 1.38\times10^{-23}JK^{-1}$ is Boltzmann's constant and T is the temperature in degrees Kelvin.

$$\frac{N_-}{N_+} = exp^{\left(-\gamma B_0/kT\right)} \qquad \text{Eq 1-2}$$

At thermal equilibrium, the small population excess of spins in the lower energy state gives rise to the equilibrium magnetization, M_0 given by Eq 1-3, where $\hbar$ is the Planck's quantum constant and N is the number of excess spins.

$$M_0 \approx N\frac{\gamma^2\hbar^2B_0}{4kT} \qquad \text{Eq 1-3}$$

1.2.3 Excitation and Relaxation

Once the sample of interest is placed in the MR scanner, the spins align (parallel or anti-parallel) in the direction of the main B_0 field (z-direction) and the equilibrium magnetization (M_0)

is produced in the same direction. For a receiver to sensitize the signal to M_0, a radiofrequency (RF) pulse gradient B_1 is applied perpendicular to the z-axis to rotate the M_0 from z-axis to the transverse plane (x-y plane). This process is called excitation. The application of the RF pulse causes the particles to absorb the energy required to move from the lower energy state to the higher energy state. The angle between the B_0 field and rotated M_0 is called the flip angle α, which is proportional to B_1 and the time τ that the rf pulse is applied (Eq 1-4) (Figure 1-3).

$$\alpha = \gamma B_1 \tau \qquad \text{Eq 1-4}$$

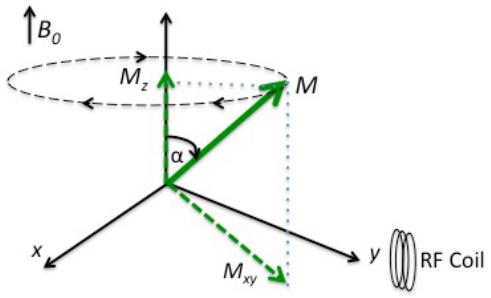

Figure 1-3. After excitation, M is tipped away from the B_0 axis through angle α and precesses about B_0 with $M_{xy}(t)$ and $M_z(t)$.

After the rf pulse is applied, the magnetization vector M precesses about the z-axis at the Larmor frequency ω. There are two methods by which M returns to its initial state (M_0). These are longitudinal and transverse relaxation.

Longitudinal relaxation is the process by which spins release energy into the surrounding lattice environment allowing the corresponding magnetization (M_z) to recover to equilibrium M_0. The growth of M_z is defined by Eq 1-5, where T_1 is the rate constant that describes this process and is defined by the time it takes for M_z to recover to 63.2% of M_0.

$$M_z(t) = M_0(1 - e^{-\frac{t}{T_1}}) \qquad \text{Eq 1-5}$$

Transverse relaxation is the process by which spins lose their coherence through spin-spin interactions and the correpsonding magnetization (M_{xy}) recovers to zero. This is most frequently due to slowly fluctuating or static field variations within tissue, which cause individual spins to experience a slightly different magnetic field. This means that the spins resonate at slightly different frequencies, resulting in a temporary gain or loss of phase with respect to the other spins. The resulting loss of coherence or "dephasing" reduces the net transverse magnetization, M_{xy}, and is governed by Eq 1-6, where T_2 is the rate constant that describes this process and is the time it takes for M_{xy} to decay to 36.8% of original M_{xy} component.

$$M_{xy}(t) = M_0 e^{-\frac{t}{T_2}} \quad \text{Eq 1-6}$$

In practice, magnetic field inhomogeneity and susceptibility effects also cause spin dephasing, which more rapidly decreases M_{xy}. T_2^* is the time constant that describes the loss of coherence due to external field inhomogeneities (T_{2i}) as well as intrinsic, non-reversible T_2 dephasing. T_2 is described by Eq 1-7.

$$T_2^* = \frac{1}{T_2} + \frac{1}{T_{2i}} \quad \text{Eq 1-7}$$

Differences in T_1 and T_2 values between tissues are key to generating contrast in MR images. Table 1-1 shows T_1 and T_2 for major regions of the brain. In general, T_2 values are much less dependent on B_0 compared to T_1. Both of them are strongly influenced by the water content of tissue and vary significantly in abnormal tissue. This is one of the reasons why MRI is a highly sensitive tool for imaging the brain.

Table 1-1. Typical T_1 and T_2 values for grey and white matter at 1.5T and 3T

Brain Tissue	T1		T2	
	1.5T	3 T	1.5T	3T
White Matter	884 ms	1100 ms	72 ms	60 ms
Gray Matter	1124 ms	1800 ms	95 ms	70 ms

MR signal (S) is dependent on the TR, TE, T_1 T_2, and the spin population (ρ) as described in Eq 1-8.

$$S = \rho(1 - e^{-\frac{TR}{T_1}})\, e^{-\frac{TE}{T_2}} \quad \text{Eq 1-8}$$

As can be seen, contrast from T_1 and T_2 can be accentuated or alleviated by using different TR and TE. Table 1-2 demonstrates how altering TR and TE can change the T_1 and T_2 weighting of image contrast.

Table 1-2. Relationship between TE, TR and various image-weighting.

Image-Weighting	TE	TR
T1 weighted	Short	Short
T2 weighted	Long	Long
Proton Density-weighted	Short	Long

1.3 MRI of Brain Tumor

1.3.1 Anatomical Imaging

The phase "anatomical imaging" in MRI refers to T1 and T2-weighted images, which have been standard sequences in routine clinical use in many years. Despite rapidly developing MR imaging techniques, T1 and T2-weighted images are still critical tools for the diagnosis of brain tumors.

Regions where the blood brain barrier (BBB) has broken down are generally thought to be the most aggressive portion of the brain tumor. Gadolinium-based contrast agents leak out of the vasculature in such regions and cause a shortening in T_1. In normal brain, where the BBB is in intact, these agents remain in the vasculature and will not be seen in brain tissue. Gadolinium contrast agents are very useful for identifying regions of BBB disruption and have been used as surrogate markers of tumor presence in GBM. However, Contrast enhancement cannot visualize

the full extent of glioma due to its infiltrating feature. The region that tumor cells blend with the normal brain parenchyma where the blood brain barrier is still intact is not seen in T1 images. And T2 weighted images were often used to define the extent of tumor region.

T_2 values vary between abnormal and normal tissue. The abnormality usually causes the T_2 values to increase and even small variations cause a significant visual difference in T2-weighted images. Typical T2-weighted images include fluid-attenuated inversion recovery (FLAIR) and fast spin-echo (FSE) sequence. The FSE can sometimes be difficult to interpret especially given the cases of tumors that occur very close to the CSF and both regions would show hyperintensity. In contrast, FLAIR gives better contrast between abnormal regions and normal brain tissue as the sequence would null the signal coming from CSF before excitation by playing an inversion recovery pulse. Both FLAIR and FSE are acceptable images for assessing changes in tumor volume, although FLAIR is currently more dominant.

Patients who present with headaches or seizure are referred for an MRI exam of the brain. This typically includes T1-weighted images, with and without contrast, and T2-weighted images. Radiologists review the images to identify suspicious features such as presence of an enhancing mass, volume effect, and T2 hyperintensity. Figure 1-4 shows an example of a patient with de novo, treatment-naïve GBM which is depicted by a region of T2 hyperintensity on a FLAIR (A) and FSE (B), collapsing of the patient's left ventricle due to obvious mass effect (C), and a region of contrast enhancement seen by T1-weighted post-contrast hyperintensity (D).

If the imaging exam shows evidence of such features, the patient will undergo biopsy and/or surgical resection. Histologic analysis of the tissue samples that are acquired during these procedures are examined to identify the most malignant features and define the grade of the tumor. As discussed in section 1.1.3, standard therapy also includes combined radiation therapy and temozolomide.

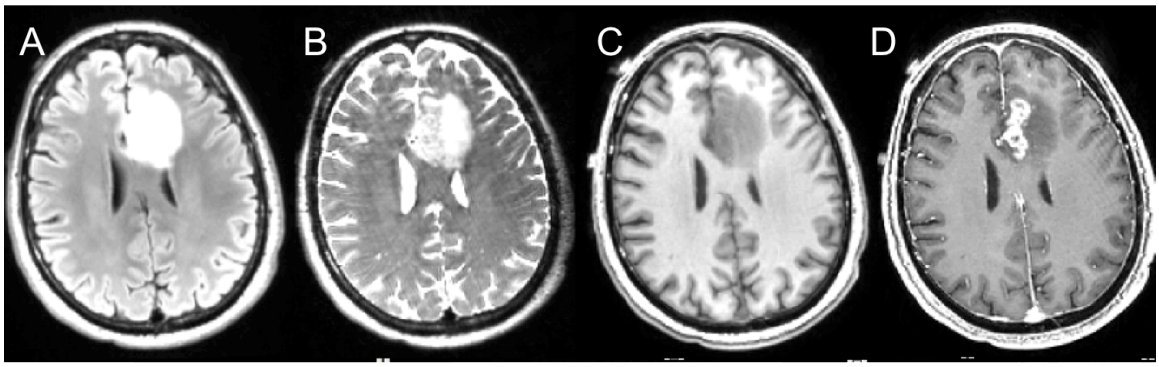

Figure 1-4. T2-weighted FLAIR (A) and FSE (B), T1-weighted pre-contrast (C), and T1-weighted postcontrast (D) MR images at 3 Tesla of a patient with newly diagnosed GBM.

1.3.2 Perfusion Imaging

Advanced imaging methods that can be used to monitor physiologic and metabolic changes in the brain have been proposed as tools that can provide a more accurate diagnosis and assessment of response to therapy for GBM. Perfusion has been used to assess vascular function by tracking the relaxation effects of a bolus of gadolinium that has been injected intravenously as it circulates through the brain. The most widely used perfusion imaging technique in clinical setting is dynamic susceptibility contrast imaging (DSC). This highlights the time-course of changes in image contrast due to alterations in relaxation times and can be used to describe functional characteristics of the underlying vasculature.

DSC-MRI focuses on capturing the first-pass of the bolus of contrast agent. It utilizes the decrease and subsequent recovery in signal observed on T2 or T2* weighted images as the agent passes through the vasculature. The reduction in signal is due to spin-spin dephasing due to the susceptibility gradient, which is induced by the intravascular compartmentalized gadolinium. The signal intensity over time curve can be converted to a change in T2* relaxivity (ΔR_2^*) curve which has a nearly linear relationship with contrast agent concentration [14], thus providing information about the hemodynamics of the tissue.

Multiple parameters can be derived from DSC curves. The parameter most widely reported is the cerebral blood volume (CBV). This relates the area under the curve during the bolus to the concentration of the agent. Other parameters include the height of the peak (PH) in the ΔR_2^* curve and the percent recovery to baseline (RECOV), which reflects the leakiness of the tumor induced vessels. Figure 1-5 shows the generation of a ΔR_2^* curve and the quantification of PH and RECOV.

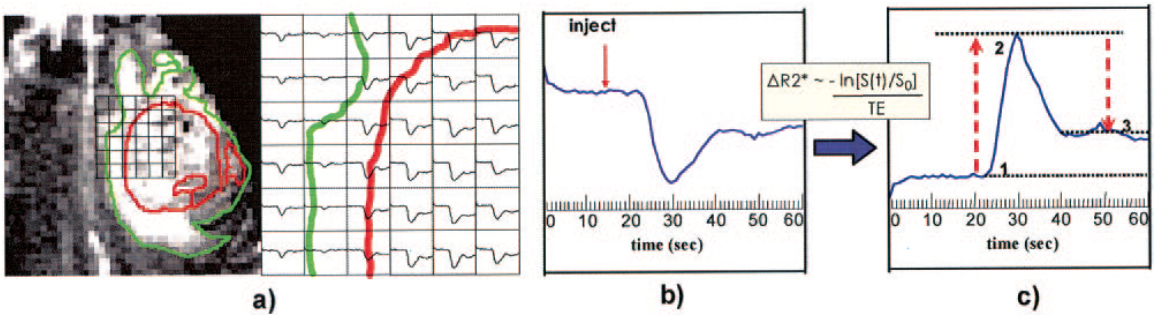

Figure 1-5 a) T2 and contrast enhancing contours overlaid on a GRE EPI and corresponding resampled T2* signal intensity time curves. b) Plot of T2* signal intensity time curve, S(t), for one voxel with red solid arrow denoting the time of contrast agent injection. c) Relative concentration curve (ΔR_2^*) obtained. Peak height (PH) is the distance from 1 to 2, while percent recovery represents how much the post-bolus signal 3 has recovered from the peak 2. (Courtesy of Janine Lupo)

DSC-MRI has been found great potential in evaluating malignancy of gliomas in many studies. In particular, it's been shown to improve the characterization of the degree of angiogenesis [15] and was found to correlate with the vascular histopathology [16]. It has also been used to assess response to antiangiogenic therapy [17,18] and as well as a potential biomarker for prognosis following standard treatment [19,20]. The use of DSC-MRI for differentiating true progression from pseudoprogression has also been an area of interest for investigation [21-23].

1.3.3 Spectroscopic Imaging

Another technique that is becoming more widely used is that of spatially localized in vivo H-1 Magnetic Resonance Spectroscopic Imaging (MRSI). This is able to simultaneously measure the levels of different cellular metabolites from multiple voxels and is based upon the observation that protons in different regions of a molecule resonate at the different frequencies due to variations in chemical shift and J-coupling.

Chemical shifts reflect differences in frequency that are observed when the electron clouds surrounding protons create small magnetic fields that oppose the main B_0 field. This effect is known as shielding and it affects the resonant frequency as described by Eq 1-9, where σ is the chemical shielding factor for chemical i.

$$\omega_i = \gamma B_0(1 - \sigma_i) \qquad \text{Eq 1-9}$$

The chemical shift expressed is typically expressed in a frequency scale independent of the magnetic field strength and is called parts per million or ppm. The ppm value for a proton resonating at a frequency ω_i is defined by Eq 1-10, where reference frequency, ω_{rf}, of tetramethylsilane (TMS) is defined to be 0 ppm. The ppm value is used to display MR spectra, with positive ppm values to the left.

$$ppm_i = \frac{\omega_i - \omega_{rf}}{\omega_{rf}} \times 10^6 \qquad \text{Eq 1-10}$$

J-coupling also affects the resonance of a proton in a molecule and is independent of magnetic field. In this case, interaction between the proton and neighboring electronegative groups translates to each peak splitting into a complex peak (e.g. doublet, triplet), this is referred to as spin-spin splitting. A proton having n neighboring protons will generally break down to n+1 peaks due to these interactions.

In vivo MRSI data that are acquired from healthy brain tissue with a long TE (~144 ms) are characterized by three major metabolite peaks: choline (Cho), creatine (Cre), and N-acetyl aspartate (NAA). Abnormal processes in the brain, including inflammation, tumor, treatment effects, etc., affect the heights of the peaks corresponding to these metabolites and may also reveal resonances such as lactate (Lac) and lipid (Lip). Figure 1-6 illustrates spectra from normal and abnormal regions of the brain.

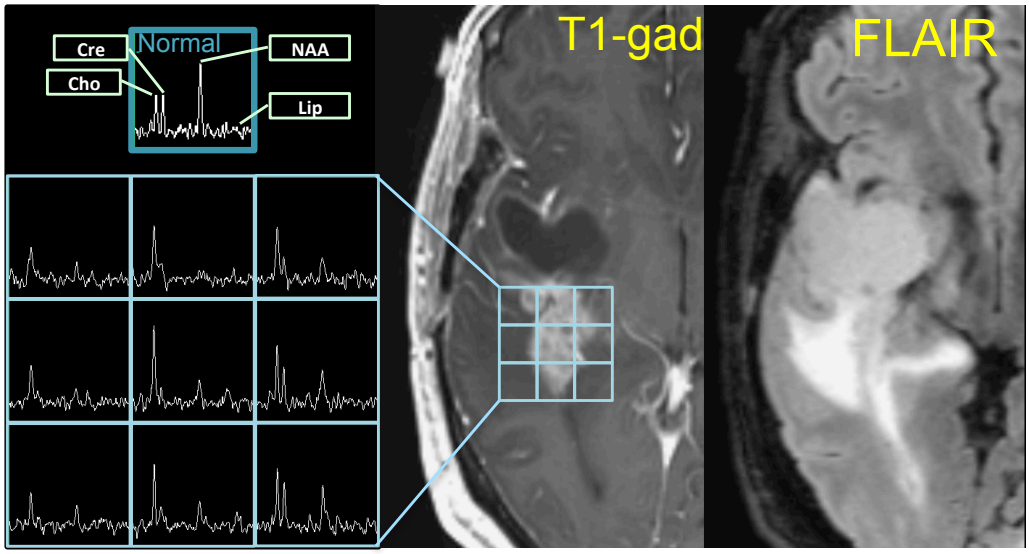

Figure 1-6 MRSI from a tumor region with the spectra from normal tissue on the side. In a GBM, Choline is increased and NAA is decreased comparing to normal tissue, and elevated Lipid level indicates necrotic tissue.

The choline peak resonates as a singlet at 3.22 ppm. It comprises free choline, acetylcholine, phosphocholine (PC), and glycerophosphocholine (GPC). Choline is required for the synthesis of the neurotransmitter acetylcholine and phosphatidylcholine is a major constituent of the cell membrane. An increase in the levels of choline provides a marker for excessive cell growth, increased cell density or cell membrane turnover, which are associated with increased tumor growth and/or treatment effects.

N-acetyl aspartate (NAA) appears as a singlet at 2.02 ppm. NAA is an amino acid that is synthesized in neurons and is a marker of neuronal viability. Decreases in NAA are observed in pathology with a loss of neurons or reduction in their function, as is seen in brain tumors.

Creatine appears as two singlets at 3.04 and 3.9 ppm. The creatine peak is composed of creatine (Cre) and phosphocreatine (PCr). These metabolites are involved with ATP metabolism and are therefore thought to represent the energetic status of the cell. Creatine levels are relatively unaffected in many diseases but however patients with GBM often do show a reduction of creatine in comparison to normal brain [24].

Lipids may appear in the spectra due to folding in from the skull or in regions of necrotic tumor, with a chemical shift of 1.3 and 0.9 ppm. Lipids in the cell membrane do not significantly contribute to the observed signals due to their very short T2 relaxation. The resonances that can be observed are thought to be correlated with mobile lipids, such as adipose or cytoplasmic droplets, and to be associated with phospholipids that are released during cell breakdown. The presence of lipid peaks is typically associated regions of necrosis that are observed in high-grade gliomas [25].

Lactate appears as a doublet at 1.33 ppm and is a byproduct of anaerobic glucose metabolism. Although it is not usually seen in normal spectra, it is more likely to be present in areas of tumor due to the presence of poor oxygenation and hypoxia. It can also be observed in ischemic regions of tumor regions [26,27], which is typically observed immediately post surgery. It is a potential physiologic marker for tumor malignancy [28].

There is a growing body of evidence in the literature that MRSI can contribute to diagnosis and treatment monitoring for patients with glioma [29-34].

1.4 Diffusion Imaging

Diffusion MRI is a technique that is capable of providing in vivo images with a contrast uniquely sensitive to molecular displacement at cellular and sub-cellular length scales. The average diffusion coefficient for water in the CNS is about 1 mm^2/ms and the typical MR diffusion experiment employs a diffusion time of 20–80 ms. This means that the average water molecule probes a length scale on the order of 5–20um and makes diffusion MR sensitive to a wide range of tissue microstructures, including axons, dendrites, glial cells, et cl. Diffusion imaging has become a valuable tool in assisting diagnosis of many brain diseases, including acute stroke [35], epilepsy [36], multiple sclerosis [37] and brain tumors [38].

Although it is possible to acquire diffusion data on most MR scanners and it is routinely included in many clinical protocols for evaluating patents with brain tumors, the implications of the parameters being used are often not appreciated by the oncology community. This is especially true when it is applied to patients with gliomas, where tissue is highly heterogeneous, changes in diffusion parameters are usually not specific to tumor. Advanced diffusion models that aim to disentangle differences in tissue composition have great potential in providing complementary information to routine MR imaging. At the current time, the applications of such advanced models in clinical studies has been very limited due to the long acquisition times that are typically required. These factors have provided motivations for this thesis in that we will explore the value of current routine diffusion imaging in several clinical trials to better understand their implications. We will also strive to bring advanced diffusion models into routine clinical application using state of the art fast imaging techniques.

In the following section, we will introduce the basic principles of diffusion weighted imaging and summarize its current applications in the assessment of patients with GBM.

1.4.1 Diffusion Measurements Using MRI

The diffusion that we are interested in is called intra-voxel incoherent motion, random motion, or Brownian motion (Figure 1-7a). If we drop ink in such a system, its shape become bigger as time elapses but its center remains at the same position. Along any arbitrary axis, the probability of going in all directions is the same. Assuming there is no barrier, the ink will spread out according to a "Gaussian" distribution.

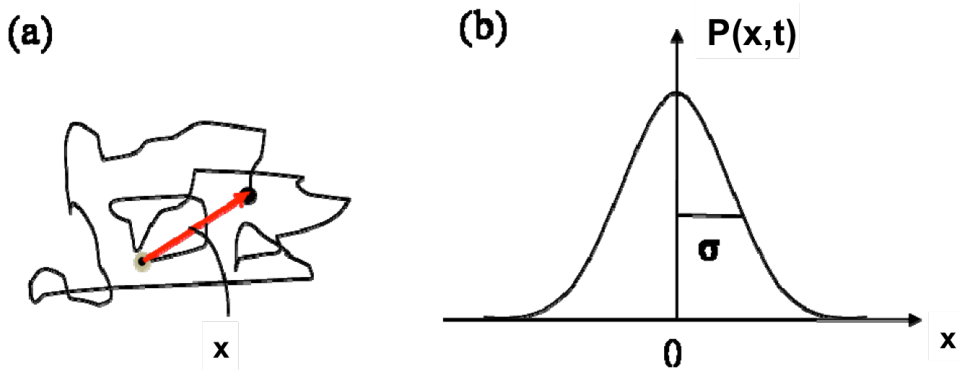

Figure 1-7 Schematic representation of random walk of a water molecule that has a displacement of x (red arrow) (a). The distribution of its displacement s after time t is shown in (b).

As introduced in 1.2 and 1.3, signal intensity in MRI is dominated by the number of water molecules present (proton density), and by relaxation times such as T_1 and T_2. The task of measuring diffusion is to sensitize the signal intensity to the amount of the motion of the water molecules. To achieve this, a gradient field is applied so that molecules at different locations will experience different field strengths and hence be dephased by varying amounts.

When a pair of dephasing and rephasing gradients are applied, the signal is sensitized to molecular motions and the signal becomes "diffusion-weighted". i.e., the gradient "diffusion - weights" the signal. This is because perfect refocusing happens only when water molecules do not change their locations between the application of the dephase-rephase gradients. Figure 1-8 illustrates the basic sequence used in diffusion and shows how the phase evolves in the absence of

diffusion. Figure 1-9 illustrates how the application of diffusing gradients can tag the diffusing water molecules and 'weights' the signal.

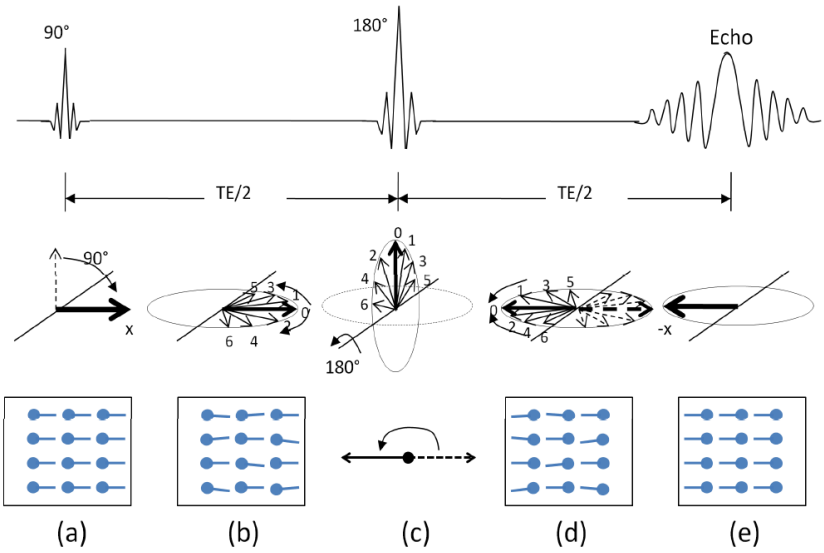

Figure 1-8 Illustration of phase evolution of spins at different stages of the image acquisition: (a) excitation (t = 0); (b) dephasing; (c) refocusing (t = TE/2); (d) rephasing and (e) echo (t = TE). TE is the echo time.

The dephasing gradient "tags" locations of water molecules based upon their phase. If water moves, it results in disruption of the phase gradient across the sample and after the rephasing gradient, molecules that have moved can be detected because they have different phases from stationary molecules at the same location. MRI cannot measure the phase of individual water molecules, but it can detect imperfect rephasing based upon the loss of signal intensity.

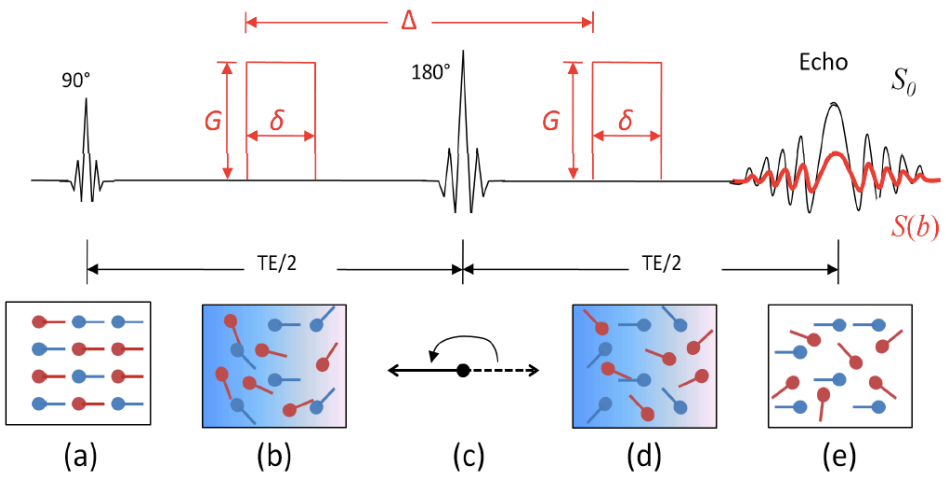

Figure 1-9 Illustrations of spin phase evolution. Shown in red is the added diffusion gradients compared to Figure 1-8

1.4.1.1 Mathematics of Diffusion Measurement

The amount of phase difference introduced by a gradient pulse with strength G and a duration of δ with respect to an arbitrarily defined reference point (x=0) is:

$$\phi(x) = e^{i\gamma G\delta x} \qquad \text{Eq 1-11}$$

where γ is the gyromagnetic ratio ($2.765\times10^8\ T/s$) and x is the distance from the reference point along the x-axis. If we assume that there is free or unhindered diffusion, the distribution of water molecules can be described by a Gaussian distribution (Figure 1-7b). In general, the Gaussian function is described as:

$$\frac{1}{\sigma\sqrt{2\pi}} e^{x^2/2\sigma^2} \qquad \text{Eq 1-12}$$

where $1/\sigma\sqrt{2\pi}$ is the scaling actor to normalize the area under the curve to 1. This gives us the population of water molecules at location x. The parameter σ controls the width of the curve, or how far water molecules travel on average. We can use Einstein's equation, $\sqrt{2Dt}$, to estimate the average distance water travels. So by substituting σ with $\sqrt{2Dt}$, we can obtain:

$$P(x,t) = \frac{1}{\sqrt{4\pi Dt}} e^{-x^2/4Dt} \quad \text{Eq 1-13}$$

where $P(x,t)$ tells population of water at location x at time point t. The longer the $t(=\Delta)$, the wider the distribution becomes. For the fixed length of Δ, higher diffusion constants (D) lead to a wider distribution.

The total MR signal can be calculated by summing up the product of population and signal phase at location x:

$$Signal = \int_x P(x,t)\phi(x)dx = \frac{1}{\sqrt{4\pi D\Delta}} \int_x e^{-x^2/4D\Delta} e^{i\gamma G\delta x} dx \quad \text{Eq 1-14}$$

Eq 1-14 can be calculated as follows:

$$\frac{1}{\sqrt{4\pi D\Delta}} \int_x e^{-x^2/4D\Delta} e^{i\gamma G\delta x} dx \quad \text{Eq 1-15}$$
$$= \frac{1}{\sqrt{4\pi D\Delta}} \left[\int_x e^{-x^2/4D\Delta} \cos(\gamma G\delta x)\, dx - i \int_x e^{-x^2/4D\Delta} \sin(\gamma G\delta x) dx \right]$$

The second term is 0 because it is an asymmetric function. The integration of the real term is:

$$Signal = e^{-\gamma^2 G^2 \delta^2 D\Delta} \quad \text{Eq 1-16}$$

This signal intensity is normalized, so that its maximum value is 1 when $G = 0$ (no diffusion weighting). If we assign S_0 and S for the signal intensity without and with diffusion weighting, Eq 1-16 becomes:

$$S = S_0 e^{-\gamma^2 G^2 \delta^2 D\Delta} \quad \text{Eq 1-17}$$

In a practical situation, the gradient length δ is usually long (5-30ms), and we cannot neglect the molecule motion during the gradient pulse. So the phase gradation introduced is now a function of both location x and time t:

$$\phi(x,t) = e^{i\gamma G(t)tx} \quad \text{Eq 1-18}$$

To calculate signal intensity, we need to integrate not only location x but also time t. The derivation is omitted here and the general solution in the practical situation would be:

$$S = S_0 e^{-\gamma^2 G^2 \delta^2 D(\Delta - \frac{1}{3}\delta)} \quad \text{Eq 1-19}$$

The parameters $G, \delta, and\ \Delta$ can be controlled by the scanner. These parameters are often abbreviated to one parameter, $b = \gamma^2 G^2 \delta^2 (\Delta - \frac{1}{3}\delta)$ and the preceding equations simplified to:

$$S = S_0 e^{-bD} \quad \text{Eq 1-20}$$

It can be seen from Eq 1-20 that from two measurements - with (S) and without (S_0) diffusion weighting, we can estimate a diffusion constant along the direction that the gradient (G) is applied.

1.4.2 Principle of Diffusion Tensor Imaging (DTI)

When diffusion occurs preferentially in a given direction it is described as being "anisotropic". This is of great interest because it carries information about the underlying anatomical architecture of living tissues. Whenever there is ordered structures such as axonal tracts in the brain or protein filaments in muscle, the water tends to diffuse along them (Figure 1-10). Due to collisions with the fibers, water molecules would travel less distance perpendicular to the fiber direction than along the fiber. It can be modeled as an ellipsoid with preferred direction pointing toward the fiber direction. If we can determine the shape of ellipsoid, we can obtain structural information about the object. This is exactly what we try to accomplish using diffusion tensor imaging (DTI).

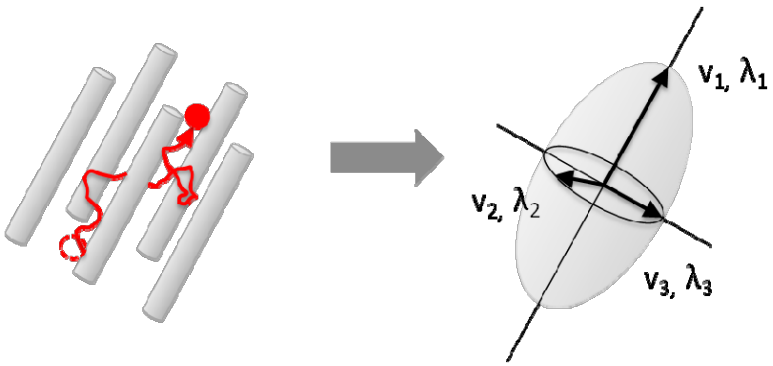

Figure 1-10 Water diffusion in an environment contains densely packed long fibers. Due to collisions with the fibers, water molecules would travel less distance perpendicular to the fiber direction than along the fiber. It can be modeled as an ellipsoid with preferred direction pointing toward the fiber direction.

Six parameters are needed to uniquely define an ellipsoid. We need three lengths for the longest, shortest, and middle axes that are perpendicular to each other. These three lengths are usually called $\lambda_1, \lambda_2, \lambda_3$, or "eigenvalues". To define the orientation of the principal axes we need three unit vectors (three degrees of freedom). These vectors are called v_1, v_2, v_3, or "eigenvectors", as shown in Figure 1-10. DTI then characterizes the diffusion ellipsoid from multiple diffusion constant measurements along different directions. Intuitively we can see that if the directions are well chosen, we need at least six measurements to determine the six parameters $(\lambda_1, \lambda_2, \lambda_3, v_1, v_2, v_3)$.

Strictly speaking, the equations to measure diffusion constants (Eq 1-20) hold only when molecules are diffusing freely and when the process can be described by a Gaussian distribution. If there are obstacles and boundaries present (restricted diffusion), the basic assumptions does not hold. While the diffusion constant of the parenchyma could truly be slower than that of CSF because of higher viscosity, the majority of the reduction in translational motion observed is most likely due to the presence of obstacles. It is for that reason that the diffusion constant calculated from Eq 1-20 is typically called the "apparent" diffusion constant (ADC).

1.4.2.1 Mathematics of Diffusion Tensor Imaging

In order to keep track of the six parameters $\lambda_1, \lambda_2, \lambda_3, v_1, v_2, v_3$, we use a 3×3 tensor, called a diffusion tensor, $\overline{\overline{D}}$, which is related to the six parameters by diagonalization.

$$\overline{\overline{\boldsymbol{D}}} = \begin{bmatrix} D_{xx} & D_{xy} & D_{xz} \\ D_{yx} & D_{yy} & D_{yz} \\ D_{zx} & D_{zy} & D_{zz} \end{bmatrix} \xrightarrow{diagonalization} \lambda_1, \lambda_2, \lambda_3, v_1, v_2, v_3 \quad \text{Eq 1-21}$$

Rewriting Eq 10 in a more complete expression for anisotropic media, we have:

$$\ln\left[\frac{S}{S_0}\right] = e^{-\sqrt{b}\overline{\overline{\boldsymbol{D}}}\sqrt{b}^T} \quad \text{Eq 1-22}$$

where $\overline{\sqrt{b}} = \gamma \bar{G} \delta \sqrt{(\Delta - \delta/3)}$, Here $\bar{G}$ and $\sqrt{b}$ are vectors because they contain information about the orientation.

Next, expanding $\sqrt{b}\overline{\overline{\boldsymbol{D}}}\sqrt{b}^T$ we have:

$$\sqrt{b}\overline{\overline{D}}\sqrt{b}^T = \begin{bmatrix} \sqrt{b_x} & \sqrt{b_y} & \sqrt{b_z} \end{bmatrix} \begin{bmatrix} D_{xx} & D_{xy} & D_{xz} \\ D_{yx} & D_{yy} & D_{yz} \\ D_{zx} & D_{zy} & D_{zz} \end{bmatrix} \begin{bmatrix} \sqrt{b_x} \\ \sqrt{b_y} \\ \sqrt{b_z} \end{bmatrix} \quad \text{Eq 1-23}$$

where $\overline{\boldsymbol{D}}$ and $\overline{\boldsymbol{b}}$ are defined as:

$$\begin{aligned} \overline{\boldsymbol{D}} &= [D_{xx} \quad D_{yy} \quad D_{zz} \quad 2D_{xy} \quad 2D_{xz} \quad 2D_{yz}] \\ \overline{\boldsymbol{b}} &= [b_x \quad b_y \quad b_z \quad \sqrt{b_x b_y} \quad \sqrt{b_x b_z} \quad \sqrt{b_y b_z}] \end{aligned} \quad \text{Eq 1-24}$$

Eq 1-22 can be written as:

$$ln(S) = \ln(S_0) - \overline{\boldsymbol{D}}\overline{\boldsymbol{b}} \quad \text{Eq 1-25}$$

Eq 1-25 can be solved by linear least-square fitting. E.g. If we take 6 measurements by applying gradients at six directions, then we will have:

$$\begin{bmatrix} S_1 \\ S_2 \\ S_3 \\ S_4 \\ S_5 \\ S_6 \end{bmatrix} = \ln(S_0) - \overline{\boldsymbol{D}} \begin{bmatrix} b_1 \\ b_2 \\ b_3 \\ b_4 \\ b_5 \\ b_6 \end{bmatrix} \quad \text{Eq 1-26}$$

where $b = \gamma^2 G_{x,y,z}^2 \delta^2 D(\Delta - \delta/3)$.

Parameters commonly extracted to present the tensor and are calculated as follows:

$$ADC = \frac{\lambda_1 + \lambda_2 + \lambda_3}{3} \quad \text{Eq 1-27}$$

$$FA = \sqrt{\frac{1}{2}} \frac{\sqrt{(\lambda_1 - \lambda_2)^2 + (\lambda_2 - \lambda_3)^2 + (\lambda_3 - \lambda_1)^2}}{\sqrt{\lambda_1^2 + \lambda_2^2 + \lambda_3^2}}$$

$$ev1 = \lambda_1, ev2 = \lambda_2, ev3 = \lambda_3$$

The two most commonly used parameters are the apparent diffusion constant (ADC) and fractional anisotropy (FA). The range of FA is 0-1 with 0 for a sphere ($\lambda_1 = \lambda_2 = \lambda_3$) and becomes larger as the ellipsoid deviates from a sphere and is more anisotropic. Eigen values (Ev) are also widely applied as they are insensitive to the orientation of the fibers. Figure 1-11 demonstrates the image contrast on these maps.

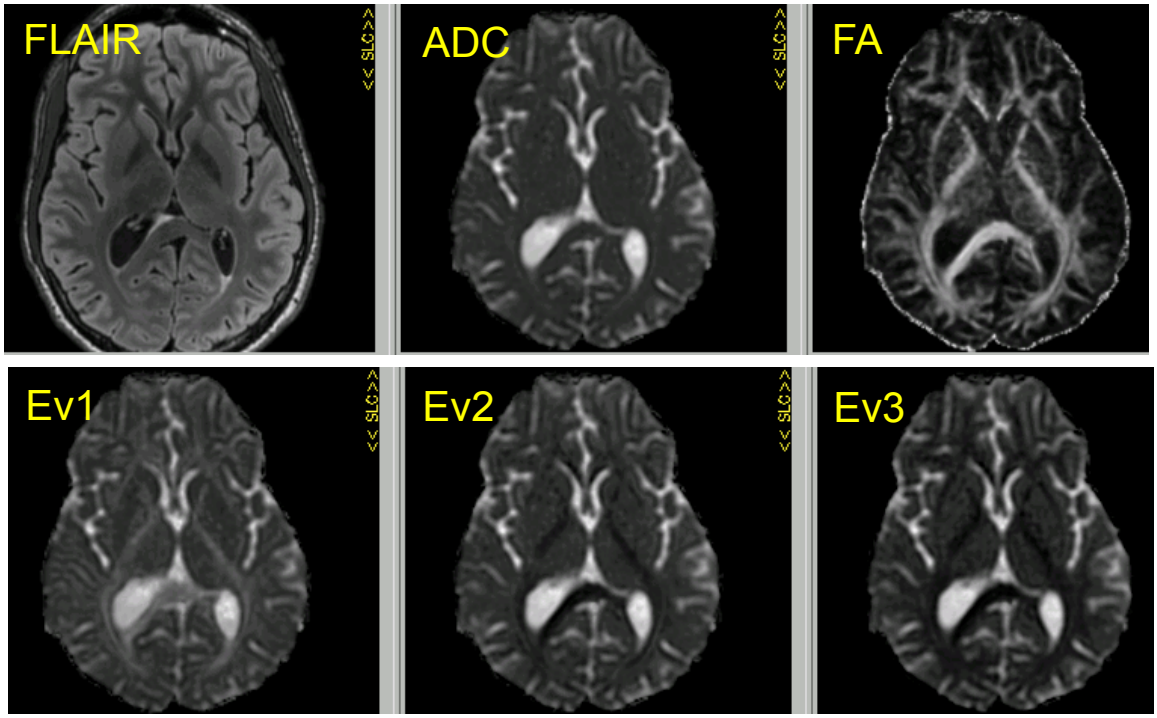

Figure 1-11 Various image contrasts obtained from DTI. ADC describes the mean axis of the tensor and FA describes the anisotropy of the tensor. Ev1, Ev2, Ev3 are insensitive to the orientation of the tensor.

1.4.3 Practical Aspects of Diffusion Tensor Imaging

In this section, we will discuss the rationale behind the acquisition parameters being used in the diffusion sequence. We will also talk about the image artifacts associated with it and how to correct for them. Then we conclude with the diffusion protocol we are currently using and its post-processing pipelines.

1.4.3.1 Use of Echo-Planar Imaging (EPI) and its Limitations

Motion is a challenge in diffusion imaging. Coherent motions lead to a phase shift of the signal and if k-space is recorded line-by-line as in a gradient echo sequence. For instance, a 128×128 matrix, which is the most commonly used matrix size in diffusion imaging, requires 128 independent scans, with each scan corresponding to one line. A non-reproducible phase shift is introduced at each scan, this leads to mis-registration of proton signals after the Fourier

transform (FT), which appears as “ghosting”. The phase errors caused by subject motion also exist in conventional MRI but the magnitude is larger in DWI because of the application of the large diffusion-weighting gradients.

The most common way for solving this problem is to use techniques such as single-shot echo-planar imaging (SS-EPI). In SS-EPI, even if the diffusion weighting and bulk motions cause phase shifts, the entire k-space has the same amount of phase error, which in theory doesn’t have any effect in the image space after the Fourier Transform (FT). Unless there is severe motion, the SS-EPI can address most of the motion-related ghosting issues. On the other hand, SS-EPI has its own problems that must be overcome.

(1) Imaging resolution is limited. The length of the echo train can usually only goes up to 128 because there is not much signal left. A longer echo train doesn’t lead to real resolution enhancement, but longer effective TE and lower signal to noise (SNR).

(2) Image distortion. The long readout time in the phase-encoding direction means that the bandwidth is very small in this direction. Such small bandwidth would exaggerate the effect of B0 field distortion, where protons located in the distorted field location with a small frequency shift would be matched a few voxels a way in the small bandwidth direction in the resulting image after the FT. Figure 1-16 shows a case acquired at 7T, where the distortion is more severe compared to lower field strength.

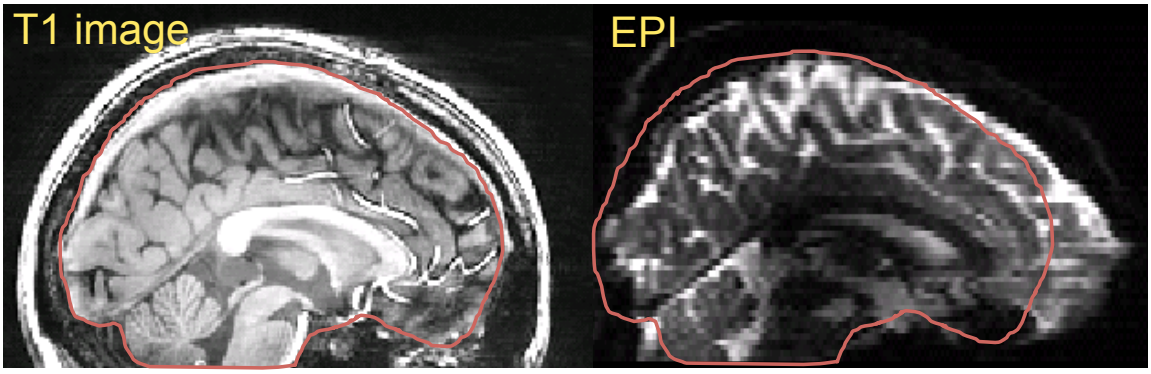

Figure 1-12 EPI distortion (sagittal view) in comparison to un-distorted T1 weighted image acquired on 7T. Susceptibility artifact is the main cause for the stretched frontal lobe and compressed parietal lobe. Image was acquired axially with phase-encoding direction in the anterior-posterior direction.

1.4.3.2 Ways to Reduce Echo Time

In order to maximize the efficiency of diffusion weighting, the entire echo time is usually filled with diffusion-weighting gradients. This means the gradient length δ is set close to the gradient separation Δ. If we set $\Delta = \delta + 5ms$ to accommodate a 180° RF pulse, and assume the gradient can be driven up to 40mT/m, then to achieve $b = 1000mm^2/s$, we need δ of ~21ms. The length of echo time (TE) must then be at least ~50ms to accommodate the diffusion-weighting gradient. In practice, the length of the echo train is typically 30ms. By combining the time required for diffusion weighting and the echo train, the echo time needs to be ~80ms.

To shorten this long echo time, it is common to use an asymmetrical echo train. For example, by using 25% truncation (75% k-space sampling) as shown in Figure 1-13, the echo time can be shortened by half of the echo train length (15ms). Asymmetric k-space coverage can efficiently shorten the echo time, and it is commonly used in routine DTI acquisitions. The most efficient and widely used partial k-space reconstruction is projection onto convex sets (POCS) and homodyne methods, which are well discussed in Bernstein MA et al, 2004[39].

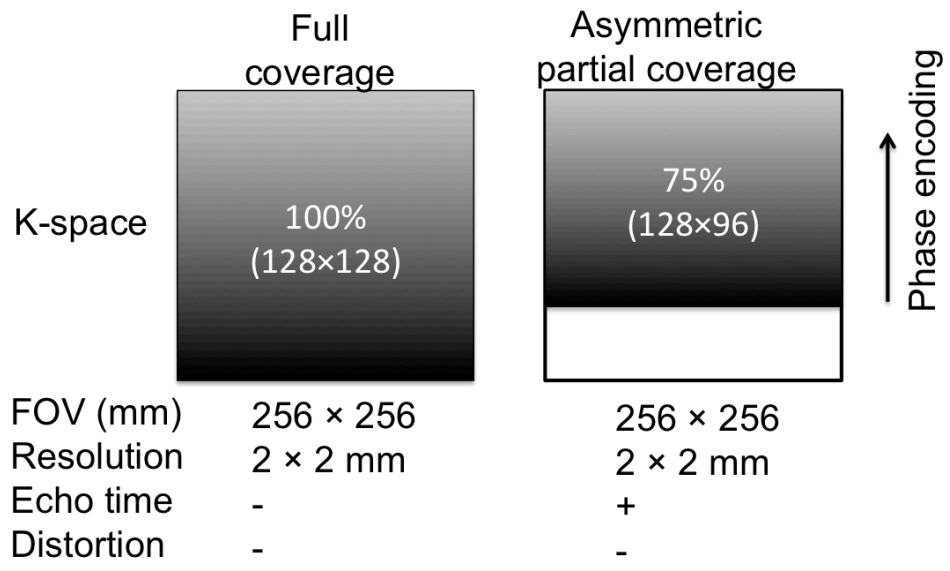

Figure 1-13 Partial k-space sampling scheme and FOVs. The k-space, FOV and resolution are indicated by frequency × phase encoding steps. For echo time and distortion, -, + indicate the extent of improvement, while – indicates the same as full coverage.

Because brains are relatively oval in shape for axial slices, it is a good idea, in theory, to use a rectangular FOV. However, there are several complications. The first option is to set the frequency encoding along the right-left (RL) orientation and phase encoding along anterior-posterior (AP) (phase encoding for the long axis). The second option is to set the frequency encoding along the AP and phase encoding is RL (phase encoding for short axis). This is a feasible option for getting shorter echo times and less distortion. However, the way the image distorts with respect to anatomy is an issue. In SS-EPI, the susceptibility distortion occurs mostly along the phase encoding orientation. Distortion is more benign when it occurs along the AP axis because it does not affect the intrinsic RL symmetry of the brain geometry. This is important for radiological diagnosis, in which the symmetry is often important information. A secondary complication is the Peripheral Nerve Stimulation (PNS). It's been shown that PNS is more likely to happen when phase-encoding is along RL and causes discomfort in patients. Considering all

these factors, square FOV with the phase encoding steps along the AP direction is still used for the majority of studies.

Another common approach to achieve shorter TE and less distortion is the use of parallel imaging. There are several implementations of parallel imaging techniques, that are known by different acronyms, such as SENSE, GRAPPA, SMASH, and ASSET, by different scanner manufacturers. These implementations have differences in technical details, yet they all achieve the same effect – namely to shorten the length of the echo train. This can effectively reduce the amount of distortion and shorten the effective echo time. Multi-channel surface coils are a prerequisite for such acquisitions and are available for most state of the art scanners. The trade off in using parallel imaging is that SNR and signal homogeneity degrades as higher acceleration factors are used. Acceleration factor of 2-3 are typically used for current applications.

With the development of multiband excitation techniques [40-42] and the implementation of 32-channel (or higher number of) surface coils, higher acceleration factors can be achieved by also applying acceleration in the slice direction. Although it is not yet in clinical use, multiband EPI has become the major technique utilized in the Human Connectome Project protocol [42-44]. The multiband DTI technique will be further discussed in Chapter 5.

Shorter TE can further be achieved by using stronger gradient with higher-gradient slew rates. The new scanner that was built at the MGH Martinos Center for human connectome project is 4 to 8 times as powerful as conventional systems. The scanner has a maximum gradient strength of 300 mT/m and a slew rate of 200 T/m/s, which significantly shortens TE and have b-values tested up to 20,000 [42].

1.4.3.3 Eddy Current Distortion and its Correction

Image distortion due to B_0 inhomogeneity has been discussed but the diffusion weighting gradient is another major source of distortion. To achieve sufficient diffusion weighting (enough b-value) within the shortest amount of time, maximum gradient strength available is applied. Rapid switches in gradients can cause eddy currents that linger after the diffusion-weighting gradients are turned off. If this lingering gradient overlaps with signal detection, unwanted image distortion occurs.

Eddy current and B_0 inhomogeneity have very different consequences on image distortions. The B_0 inhomogeneity affects the b=0 and DW images in the same way. The eddy current affects each DW image in different ways. This means that pixels in different images are not co-registered, and the tensor calculation is no longer accurate. This causes erroneously high diffusion anisotropy for pixels at tissue boundaries such as brain parenchyma and CSF. In most cases, the eddy-current induced distortions are mostly linear and global, which can be corrected in post-processing. Currently, the most time-efficient way of correcting eddy current distortion is to apply a 12-degree of freedom (DOF) linear registration between diffusion and the b=0 (or b0) image.

Another way to reduce the effect of eddy currents is through the choice of pulse sequence. One of the most widely used approaches is the so-called dual echo sequence [45], which is shown in Figure 1-14. The lingering gradient can be canceled out by the consecutive applications of positive and negative gradients. The trade-off of this method is the prolonged TE and slightly reduced SNR. The dual echo sequence is widely used in most GE clinical scanners and can be easily turned on or off in the prescription interface.

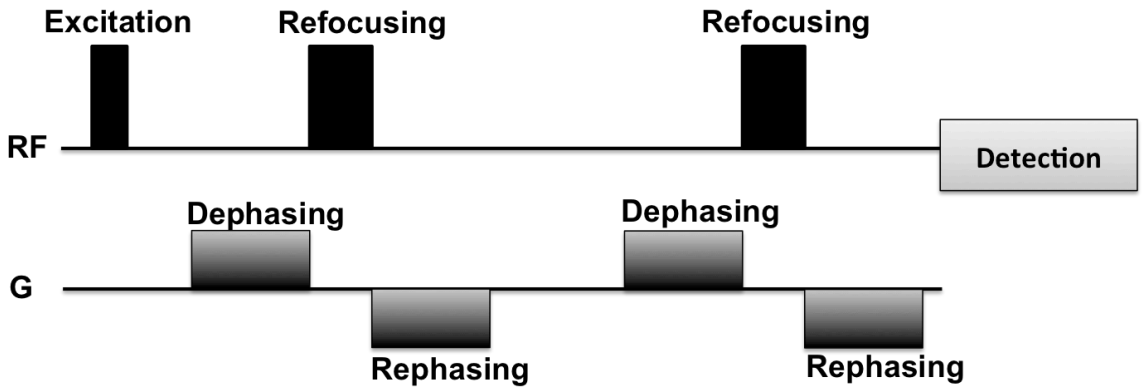

Figure 1-14 Illustration of diffusion-weighting sequence with dual spin-echo.

1.4.3.4 Our Current DTI Protocol

The standard DTI protocol on our 3T scanner employs a dual spin-echo sequence with EPI readout to minimize the eddy current effect with phase encoding direction in the AP direction. The k-space coverage is 75% and a parallel imaging method is employed (SENSE, or ASSET at GE scanner) with an acceleration factor of 2 to reduce the echo train length and to shorten TE. Matrix size is 128×128 and voxel size is 2×2×2mm with whole brain coverage. Such set up results in a TE ≈ 100 ms and TR = 8-10s.

Total acquisition time varies according to the number of directions being acquired. In theory 1 b0 (or T2 weighted) and 6 DW images are minimally required to calculate diffusion tensor parameters (including ADC, FA, EV1, EV2, EV3). In practice, more b0 images are needed as b0 is the denominator in calculating the diffusion constant D in Eq 1-20 and by acquiring more b0 and then averaging, higher SNR could be achieved to improve the final calculation. Also, the more images that are acquired, the more robust the calculation of the tensor. It has also been suggested by the FSL community that number of b0 being $1/4$ - $1/6$ the number of DW images for an optimal tensor calculation. Therefore in practice, our DTI protocol is set to acquire 4 b0 and 24 DW images to achieve a tradeoff between SNR and total acquisition time, with a scan time of ~4min.

Eddy current distortions are reduced in post-processing through an affine registration (12 DOF), and the tensor calculation is done with a weighted lease squares fitting. All the post-processing is done within FSL (FMRIB, Oxford, UK)

1.4.4 Diffusion Imaging in Gliomas

MR diffusion weighted imaging has become a widely accepted method to probe for the presence of fluid pools and molecular tissue water mobility. It has become one of the routine MR acquisitions in brain tumor secondary to T1 and T2 weighted images, and it has demonstrated significant value both in clinical diagnosis and in research studies of patients with glioma.

1.4.4.1 Diffusion Imaging For Resection of Gliomas

Minimizing damage to the eloquent cortex and white matter tracts, while maximizing surgical resection of brain tumors remains a challenge, especially when the white matter tracts are displaced or infiltrated by tumor. Diffusion tractography is a diffusion technology that resolves crossing fibers, providing a precise and thorough visualization of fibers tracts. A tract can be depicted as unchanged (when its course is not modified by the tumor or edema), dislocated, or infiltrated and/or interrupted (when the tract is in strict relationship with the mass or interrupted by it). Tractography can provide information about the relationship of these tracts to the tumor mass, and is particularly useful in helping the surgeon in surgical planning and providing intraoperative guidance as well. Successful uses have been reported by many studies [46,47]. Figure 1-15 showed a comparison between DTI and tractography derived with the technique called High angular resolution diffusion imaging (HARDI) [48].

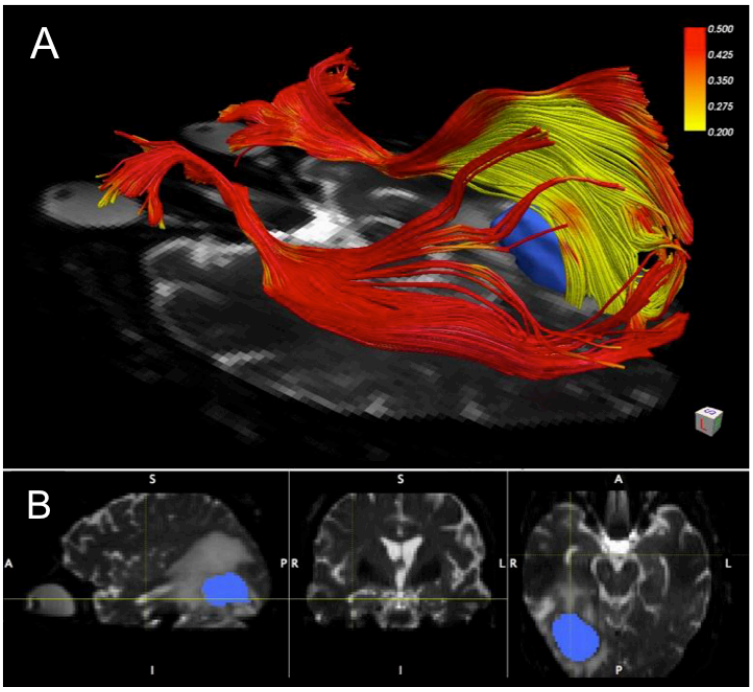

Figure 1-15 (A) Tractography used for presurgical mapping to characterize the brain microstructure in a patient with glioma in order to visualize fibers surrounding tumor mass. (B) ADC maps of the lesion from three views.

1.4.4.2 Diffusion Tensor Imaging for Differentiating Post-Resection Ischemia

While diffusion imaging is well established and widely used for the detection of early ischemic stroke [49,50], it is also a critical tool in differentiating post-surgical ischemic regions from recurrent tumor [51]. An abnormality related to diffusion-weighted sequences on postoperative MR imaging can occur after resection of gliomas. Such abnormality typically resolves and is replaced by contrast enhancement on follow-up imaging, ultimately demonstrating encephalomalacia on long-term follow up. Findings on neuroimaging during the period of enhancement could be confused with recurrent tumor and interpreted as early treatment failure. Therefore the inclusion of diffusion-weighted sequences in postoperative MR imaging is essential and is routinely used to distinguish such lesion from tumor recurrence. New enhancement observed after glioma surgery

should be interpreted in the context of the diffusion-weighted image obtained immediately postoperatively to exclude the possibility of surgery induced ischemia.

1.4.4.3 Diffusion Tensor Imaging for Monitoring Treatment Response

The values from DTI that are most widely reported in the assessment of post-treatment gliomas are ADCs. Lower ADC values reflect lower (more restricted) diffusion. Several physiologic properties of the tumor may influence ADC values. Water molecules are generally more restricted in their movement within cells and less restricted in the extracellular space. Because necrosis involves degradation of cellular integrity, it is thought that necrosis increases ADC. In a similar way, edema increases interstitial fluid, thereby increasing ADC. Conversely, increased cellular density lowers ADC by restricting diffusion. Because of these relationships, DTI has been studied as a means of evaluating the effects of therapy on malignant gliomas. ADC values within enhancement or FLAIR lesions are analyzed with a number of different quantification methods. Figure 1-16 illustrates the major methods applied for evaluating changes in ADC with treatment. These include ADC percentiles, parameters extracted from 2-mixture normal distribution fitting, or functional diffusion maps (fDM) that looks at voxel-wise changes between two time points. These methods will be explained and compared in Chapter 2.

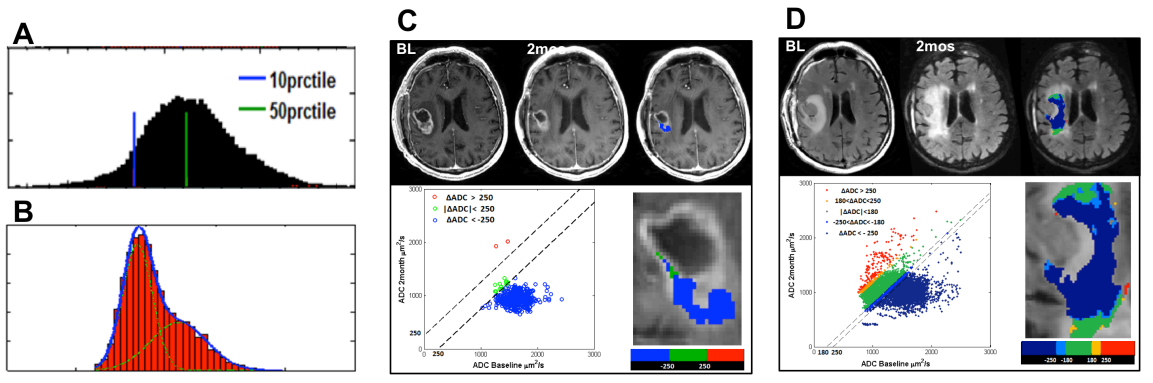

Figure 1-16 Illustration of methods for analyzing ADC: (A) percentile values extracted from the histogram of ADC values in the lesion. (B) 2-mixture normal distribution fitting on ADC histograms in CEL. (C) fDMs within

the CEL overlaid on a T1 post-contrast image at 2 months with scatter plot of the distribution of ADC changes for the entire CEL. (D) fDMs within the T2L overlaid on a FLAIR image at 2months with scatter plot of the distribution of ADC changes for the entire T2L.

Successful radiation plus cytotoxic chemotherapy treatment has been shown to increase ADC percentile values within the contrast enhancement [52,53], consistent with the radiation causing increased disruption of tissue architecture and a decrease in cellularity that is associated with treatment-induced necrosis. The functional diffusion map (fDM) was developed to take advantage of the relationship between ADC and cell density by examining voxel-wise changes in ADC measured in the same patient over time and are supposed to provide improved sensitivity of detecting subtle changes in tumor cell density (Figure 1-16C,D). This technique has primarily been applied as a tool to predict response to cyctotoxic chemotherapy and radiotherapy within the contrast-enhancing lesion and has demonstrated great success [54-56]. Specifically, they have demonstrated that patients with a larger region showing decreased ADC had shorter survival compared with patients with a smaller region. Recent studies have also demonstrated its utility outside regions of contrast enhancement [57] and as a tool for studying the effects of anti-VEGF therapy [58,59]. Our recent study of anti-VEGF therapy evaluated the association of different ADC metrics with survival and highlighted the value of parameters from the T2L at the post-RT examination in predicting outcome [60].

While ADC analysis is valuable in evaluating response to various therapies during early follow-ups, it has also been found a biomarker for survival for anti-VEGF therapy. At the pre-treatment stage, a histogram analysis of ADC within the enhancing tumor was found to be predictive of survival (Figure 1-16B). In this study, the authors hypothesized that ADC values can potentially be used as a noninvasive surrogate for VEGF expression and thus susceptibility to bevaciuzmab, and tumors with low ADC values prior to initiation of bevaciuzmab were more likely to progress compared to those with high ADC values [61-63]. At later time points into

treatment, bevacizumab has been noted to produce persistent diffusion restriction. Several groups found that such region with decreased ADC values were consistent with chronic hypoxia and were reflective of successful anti-VEGF effect, therefore associating with a longer survival [64,65].

The integration of diffusion imaging methods to the clinical MRI exam for patients with GBM has the potential to improve the diagnosis of disease, tailor adjuvant treatment strategies to an individual patient, and to provide an alternative early biomarker of response. Perfusion and MR spectroscopic imaging have also demonstrated great values in these aspects, as well as in distinguishing recurrence from treatment effect. The potential benefit of these complementary imaging parameters rests on developing reliable methods and analysis metrics that can be translated to the clinical environment. The research presented in this dissertation was aimed at addressing the engineering challenges and clinical translation of incorporating these advanced imaging metrics to the treatment management of patients with GBM, with a special focus on diffusion imaging.

1.5 References

1. Asao Hirano JF, Llena: Morphology of central nervous system axons, The Axon: Structure, Function and Pathophysiology, 1995

2. Allen NJ, Barres BA: Neuroscience: Glia - more than just brain glue. Nature 457:675-7, 2009

3. Julia M. Edgar IRG: White Matter Structure: a Microscopist's View, in Johansen-Berg H, Behrens TEJ (eds): Diffusion MRI : from quantitative measurement to in-vivo neuroanatomy (ed 1st). Amsterdam ; Boston, Elsevier/Academic Press, 2009, pp xi, 490 p.

4. Porter KR, McCarthy BJ, Freels S, et al: Prevalence estimates for primary brain tumors in the United States by age, gender, behavior, and histology. Neuro Oncol 12:520-7, 2010

5. Louis DN, Ohgaki H, Wiestler OD, et al: The 2007 WHO classification of tumours of the central nervous system. Acta Neuropathol 114:97-109, 2007

6. Stupp R, Hegi ME, Mason WP, et al: Effects of radiotherapy with concomitant and adjuvant temozolomide versus radiotherapy alone on survival in glioblastoma in a randomised phase III study: 5-year analysis of the EORTC-NCIC trial. Lancet Oncol 10:459-66, 2009

7. Friedman HS, Petros WP, Friedman AH, et al: Irinotecan therapy in adults with recurrent or progressive malignant glioma. J Clin Oncol 17:1516-25, 1999

8. Stupp R, Mason WP, van den Bent MJ, et al: Radiotherapy plus concomitant and adjuvant temozolomide for glioblastoma. N Engl J Med 352:987-96, 2005

9. Chi AS, Sorensen AG, Jain RK, et al: Angiogenesis as a therapeutic target in malignant gliomas. Oncologist 14:621-36, 2009

10. Chi AS, Norden AD, Wen PY: Antiangiogenic strategies for treatment of malignant gliomas. Neurotherapeutics 6:513-26, 2009

11. Quick A, Patel D, Hadziahmetovic M, et al: Current therapeutic paradigms in glioblastoma. Rev Recent Clin Trials 5:14-27, 2010

12. Friedman HS, Prados MD, Wen PY, et al: Bevacizumab alone and in combination with irinotecan in recurrent glioblastoma. J Clin Oncol 27:4733-40, 2009

13. Kreisl TN, Kim L, Moore K, et al: Phase II trial of single-agent bevacizumab followed by bevacizumab plus irinotecan at tumor progression in recurrent glioblastoma. J Clin Oncol 27:740-5, 2009

14. Weisskoff RM, Zuo CS, Boxerman JL, et al: Microscopic susceptibility variation and transverse relaxation: theory and experiment. Magn Reson Med 31:601-10, 1994

15. Lupo JM, Cha S, Chang SM, et al: Dynamic susceptibility-weighted perfusion imaging of high-grade gliomas: characterization of spatial heterogeneity. AJNR Am J Neuroradiol 26:1446-54, 2005

16. Essock-Burns E, Phillips JJ, Molinaro AM, et al: Comparison of DSC-MRI post-processing techniques in predicting microvascular histopathology in patients newly diagnosed with GBM. J Magn Reson Imaging 38:388-400, 2013

17. Essock-Burns E, Lupo JM, Cha S, et al: Assessment of perfusion MRI-derived parameters in evaluating and predicting response to antiangiogenic therapy in patients with newly diagnosed glioblastoma. Neuro Oncol 13:119-31, 2011

18. Sawlani RN, Raizer J, Horowitz SW, et al: Glioblastoma: a method for predicting response to antiangiogenic chemotherapy by using MR perfusion imaging--pilot study. Radiology 255:622-8, 2010

19. Cao Y, Tsien CI, Nagesh V, et al: Survival prediction in high-grade gliomas by MRI perfusion before and during early stage of RT [corrected]. Int J Radiat Oncol Biol Phys 64:876-85, 2006

20. Mangla R, Singh G, Ziegelitz D, et al: Changes in relative cerebral blood volume 1 month after radiation-temozolomide therapy can help predict overall survival in patients with glioblastoma. Radiology 256:575-84, 2010

21. Barajas RF, Jr., Chang JS, Segal MR, et al: Differentiation of recurrent glioblastoma multiforme from radiation necrosis after external beam radiation therapy with dynamic susceptibility-weighted contrast-enhanced perfusion MR imaging. Radiology 253:486-96, 2009

22. Gahramanov S, Raslan AM, Muldoon LL, et al: Potential for differentiation of pseudoprogression from true tumor progression with dynamic susceptibility-weighted contrast-enhanced magnetic resonance imaging using ferumoxytol vs. gadoteridol: a pilot study. Int J Radiat Oncol Biol Phys 79:514-23, 2011

23. Hu LS, Baxter LC, Smith KA, et al: Relative cerebral blood volume values to differentiate high-grade glioma recurrence from posttreatment radiation effect: direct correlation between image-guided tissue histopathology and localized dynamic susceptibility-weighted

contrast-enhanced perfusion MR imaging measurements. AJNR Am J Neuroradiol 30:552-8, 2009

24. Howe FA, Barton SJ, Cudlip SA, et al: Metabolic profiles of human brain tumors using quantitative in vivo 1H magnetic resonance spectroscopy. Magn Reson Med 49:223-32, 2003

25. Li X, Vigneron DB, Cha S, et al: Relationship of MR-derived lactate, mobile lipids, and relative blood volume for gliomas in vivo. AJNR Am J Neuroradiol 26:760-9, 2005

26. Harada M, Uno M, Hong F, et al: Diffusion-weighted in vivo localized proton MR spectroscopy of human cerebral ischemia and tumor. NMR Biomed 15:69-74, 2002

27. Higuchi T, Fernandez EJ, Maudsley AA, et al: Mapping of lactate and N-acetyl-L-aspartate predicts infarction during acute focal ischemia: in vivo 1H magnetic resonance spectroscopy in rats. Neurosurgery 38:121-9; discussion 129-30, 1996

28. Mariappan R, Venkatraghavan L, Vertanian A, et al: Serum lactate as a potential biomarker of malignancy in primary adult brain tumours. J Clin Neurosci 22:144-8, 2015

29. Nelson SJ: Magnetic resonance spectroscopic imaging. Evaluating responses to therapy for gliomas. IEEE Eng Med Biol Mag 23:30-9, 2004

30. Nelson SJ: Analysis of volume MRI and MR spectroscopic imaging data for the evaluation of patients with brain tumors. Magn Reson Med 46:228-39, 2001

31. Nelson SJ, McKnight TR, Henry RG: Characterization of untreated gliomas by magnetic resonance spectroscopic imaging. Neuroimaging Clin N Am 12:599-613, 2002

32. McKnight TR: Proton magnetic resonance spectroscopic evaluation of brain tumor metabolism. Semin Oncol 31:605-17, 2004

33. McKnight TR, Lamborn KR, Love TD, et al: Correlation of magnetic resonance spectroscopic and growth characteristics within Grades II and III gliomas. J Neurosurg 106:660-6, 2007

34. Li Y, Lupo JM, Parvataneni R, et al: Survival analysis in patients with newly diagnosed glioblastoma using pre- and postradiotherapy MR spectroscopic imaging. Neuro Oncol 15:607-17, 2013

35. van Everdingen KJ, van der Grond J, Kappelle LJ, et al: Diffusion-weighted magnetic resonance imaging in acute stroke. Stroke 29:1783-90, 1998

36. Gross DW: Diffusion tensor imaging in temporal lobe epilepsy. Epilepsia 52 Suppl 4:32-4, 2011

37. Rovaris M, Gass A, Bammer R, et al: Diffusion MRI in multiple sclerosis. Neurology 65:1526-32, 2005

38. Maier SE, Sun Y, Mulkern RV: Diffusion imaging of brain tumors. NMR Biomed 23:849-64, 2010

39. Bernstein MA, King KF, Zhou XJ: Chapter 11 Signal acquisition and k-space sampling, Handbook of MRI pulse sequences. Amsterdam ; Boston, Academic Press,, 2004, pp 1 online resource (xxii, 1017 p.)

40. Setsompop K, Cohen-Adad J, Gagoski BA, et al: Improving diffusion MRI using simultaneous multi-slice echo planar imaging. Neuroimage 63:569-80, 2012

41. Setsompop K, Gagoski BA, Polimeni JR, et al: Blipped-controlled aliasing in parallel imaging for simultaneous multislice echo planar imaging with reduced g-factor penalty. Magn Reson Med 67:1210-24, 2012

42. Setsompop K, Kimmlingen R, Eberlein E, et al: Pushing the limits of in vivo diffusion MRI for the Human Connectome Project. Neuroimage 80:220-33, 2013

43. Van Essen DC, Ugurbil K: The future of the human connectome. Neuroimage 62:1299-310, 2012

44. Van Essen DC, Ugurbil K, Auerbach E, et al: The Human Connectome Project: a data acquisition perspective. Neuroimage 62:2222-31, 2012

45. Reese TG, Heid O, Weisskoff RM, et al: Reduction of eddy-current-induced distortion in diffusion MRI using a twice-refocused spin echo. Magn Reson Med 49:177-82, 2003

46. Bello L, Castellano A, Fava E, et al: Intraoperative use of diffusion tensor imaging fiber tractography and subcortical mapping for resection of gliomas: technical considerations. Neurosurg Focus 28:E6, 2010

47. Vassal F, Schneider F, Nuti C: Intraoperative use of diffusion tensor imaging-based tractography for resection of gliomas located near the pyramidal tract: comparison with subcortical stimulation mapping and contribution to surgical outcomes. Br J Neurosurg 27:668-75, 2013

48. Hess CP, Mukherjee P, Han ET, et al: Q-ball reconstruction of multimodal fiber orientations using the spherical harmonic basis. Magn Reson Med 56:104-17, 2006

49. Ahlhelm F, Reith W: [Modern diagnosis in acute cerebral infarct. Diffusion weighted imaging and ADC (apparent diffusion coefficient) calculations]. Nervenarzt 73:736-44, 2002

50. Ahlhelm F, Schneider G, Backens M, et al: Time course of the apparent diffusion coefficient after cerebral infarction. Eur Radiol 12:2322-9, 2002

51. Smith JS, Cha S, Mayo MC, et al: Serial diffusion-weighted magnetic resonance imaging in cases of glioma: distinguishing tumor recurrence from postresection injury. J Neurosurg 103:428-38, 2005

52. Li Y, Lupo JM, Polley MY, et al: Serial analysis of imaging parameters in patients with newly diagnosed glioblastoma multiforme. Neuro Oncol 13:546-57, 2011

53. Chenevert TL, Stegman LD, Taylor JM, et al: Diffusion magnetic resonance imaging: an early surrogate marker of therapeutic efficacy in brain tumors. J Natl Cancer Inst 92:2029-36, 2000

54. Hamstra DA, Chenevert TL, Moffat BA, et al: Evaluation of the functional diffusion map as an early biomarker of time-to-progression and overall survival in high-grade glioma. Proc Natl Acad Sci U S A 102:16759-64, 2005

55. Hamstra DA, Galban CJ, Meyer CR, et al: Functional diffusion map as an early imaging biomarker for high-grade glioma: correlation with conventional radiologic response and overall survival. J Clin Oncol 26:3387-94, 2008

56. Moffat BA, Chenevert TL, Lawrence TS, et al: Functional diffusion map: a noninvasive MRI biomarker for early stratification of clinical brain tumor response. Proc Natl Acad Sci U S A 102:5524-9, 2005

57. Ellingson BM, Malkin MG, Rand SD, et al: Validation of functional diffusion maps (fDMs) as a biomarker for human glioma cellularity. J Magn Reson Imaging 31:538-48, 2010

58. Ellingson BM, Cloughesy TF, Lai A, et al: Graded functional diffusion map-defined characteristics of apparent diffusion coefficients predict overall survival in recurrent glioblastoma treated with bevacizumab. Neuro Oncol 13:1151-61, 2011

59. Ellingson BM, Malkin MG, Rand SD, et al: Volumetric analysis of functional diffusion maps is a predictive imaging biomarker for cytotoxic and anti-angiogenic treatments in malignant gliomas. J Neurooncol 102:95-103, 2011

60. Wen Q, Jalilian L, Lupo JM, et al: Comparison of ADC metrics and their association with outcome for patients with newly diagnosed glioblastoma being treated with radiation therapy, temozolomide, erlotinib and bevacizumab. J Neurooncol, 2014

61. Ellingson BM, Sahebjam S, Kim HJ, et al: Pretreatment ADC histogram analysis is a predictive imaging biomarker for bevacizumab treatment but not chemotherapy in recurrent glioblastoma. AJNR Am J Neuroradiol 35:673-9, 2014

62. Pope WB, Kim HJ, Huo J, et al: Recurrent glioblastoma multiforme: ADC histogram analysis predicts response to bevacizumab treatment. Radiology 252:182-9, 2009

63. Pope WB, Lai A, Mehta R, et al: Apparent diffusion coefficient histogram analysis stratifies progression-free survival in newly diagnosed bevacizumab-treated glioblastoma. AJNR Am J Neuroradiol 32:882-9, 2011

64. Rieger J, Bahr O, Muller K, et al: Bevacizumab-induced diffusion-restricted lesions in malignant glioma patients. J Neurooncol 99:49-56, 2010

65. Rieger J, Bahr O, Ronellenfitsch MW, et al: Bevacizumab-induced diffusion restriction in patients with glioma: tumor progression or surrogate marker of hypoxia? J Clin Oncol 28:e477; author reply e478, 2010

Chapter 2

Comparison of ADC metrics and their association with outcome in patients treated with a combined therapy that includes bevacizumab

In this chapter, different metrics of describing changes in apparent diffusion coefficient (ADC) are introduced. These metrics are then used to examine their association with clinical outcome for patients with newly diagnosed GBM who were participating in a Phase II clinical trial of treatment with radiation (RT), temozolomide, erlatonib and bevacizumab. Treatment related changes in ADC are observed and a potential biomarker is identified.

2.1 Introduction

Bevacizumab is a humanized monoclonal VEGF-blocking antibody that has been shown to normalize vascular permeability and regulate angiogenesis in patients with glioblastoma (GBM). Although it has been shown to reduce the volume of the contrast enhancing lesion (CEL) on post-Gadolinium T1-weighted MR images and to provide improved time to progression in patients with recurrent disease [1-3], recent Phase II and Phase III clinical trials indicated that it is ineffective at extending overall survival for patients with newly diagnosed GBM [4-7]. With a growing number of studies providing evidence for increased tumor invasiveness following treatment failure in patients receiving bevacizumab [8], it is important to identify at an early stage which patients are benefiting from anti-angiogenic therapies, as opposed to treating all patients in the same manner. Monitoring the effectiveness of bevacizumab is challenging using conventional measures of response to therapy because reductions in the CEL may be due to an anti-permeability effect rather than a reduction in bulk tumor [9], which is commonly referred to as "pseudoresponse" [10,11]. Differentiation of non-enhancing tumor within the T2L from edema or

gliosis is important for effectively monitoring response to bevacizumab and similar anti-angiogenic agents.

The apparent diffusion coefficient (ADC) is a metric that characterizes the random motion of water molecule protons in the extracellular space and may provide valuable insights to tumor physiology. Decreases in ADC have been proposed as a non-invasive measure of tumor cellularity and increases in ADC to reflect a breakdown of tissue architecture [12-16]. A number of different strategies have been proposed to define metrics in predicting clinical outcome and monitoring response to therapy following treatment with bevacizumab. These include parameters derived from the histogram of ADC values within the anatomic lesion at a single time point [17-19], and from functional diffusion maps (fDMs) that evaluate serial changes in ADC on a pixel by pixel basis [20-26]. For patients with recurrent GBM being treated with bevacizumab, low values in the pretreatment ADC histogram from the CEL that were fit to a two normal distribution mixture curve were found to be associated with poor outcome [17,18], but in the up-front setting low ADC was found to be associated with significantly longer PFS [19]. When fDM analysis was used in patients with recurrent GBM [25,26], prior studies showed that the volumes of tissue within the CEL and T2L that had reduced ADC values between baseline and early post-treatment scans were associated with PFS and OS.

Although these initial results indicate that ADC metrics may be helpful in predicting treatment effectiveness for patients with recurrent GBM, their utility has not yet been fully explored for combination treatments that are being applied in an upfront setting. Obtaining a detailed understanding of how to interpret early changes in these parameters and integrate them into criteria used for assessing treatment response could have a significant impact on patient care. The purpose of this study was to evaluate the association of ADC metrics with clinical outcomes for patients with newly diagnosed GBM who were participating in a Phase II clinical trial that included bevacizumab.

2.2 Materials and Methods

2.2.1 Patient Population

A total of 151 MR scans that include diffusion weighted imaging (DWI) were obtained from 36 patients with newly diagnosed GBM who were participating in a Phase II clinical trial during the period between January 9, 2009 and April 3, 2012 (29 scans at baseline, 25 patients had complete serial scans from baseline until progression). All patients had pathologically confirmed GBM, a Karnofsky Performance Score (KPS) of at least 60 and had undergone prior biopsy (5 patients) or surgical resection (10 gross-total and 21 sub-total) but no other prior therapy. Patient age ranged from 21 to 76 years, with a median of 52 years. Treatment included external beam radiation therapy to an average dose of 60 Gy and was delivered to the tumor site in 2-Gy fractions over a 6-week period. The protocol called for temozolomide to be given at a daily dose of 75mg/m^2, during radiation therapy and at 200mg/ m^2 for 5 days every 28 days afterwards, for erlotinib to be given daily both during and after radiation, and for bevacizumab to be given at a dose of 10mg/kg IV every 2 weeks, starting at approximately 2 weeks into radiation therapy [5]. All patients participating in this study gave informed consent according to the guidelines of our institutional review board. Progression was determined based on the recently defined RANO criteria [10].

2.2.2 MR Imaging and Post-processing

All scans were obtained using a 3T GE MR scanner. Time points selected for study were at baseline (post-surgical resection and prior to therapy), 1 month (mid-RT), 2 months (post-RT) and every 2 months thereafter until presumed tumor progression (up to a maximum of 14 months). Standard anatomical MR imaging included axial T2-weighted fluid attenuated inversion recovery (FLAIR) images and pre- and post-contrast T1-weighted spoiled gradient echo (SPGR). DWI were acquired with b=1000 (dir=6, NEX=4) and ADC maps were calculated using in-house

developed software. CEL regions were manually defined on the coregistered post-contrast T1 SPGR images at each available time point. Any hyperintense signal that was also present on the pre-contrast T1 images was assumed to be indicative of acute blood products and was excluded. The T2L regions were segmented based on the hyper-intensity region of FLAIR images using a semi-automatic region-growing segmentation tool [27]. The resection cavity was excluded from all ROIs.

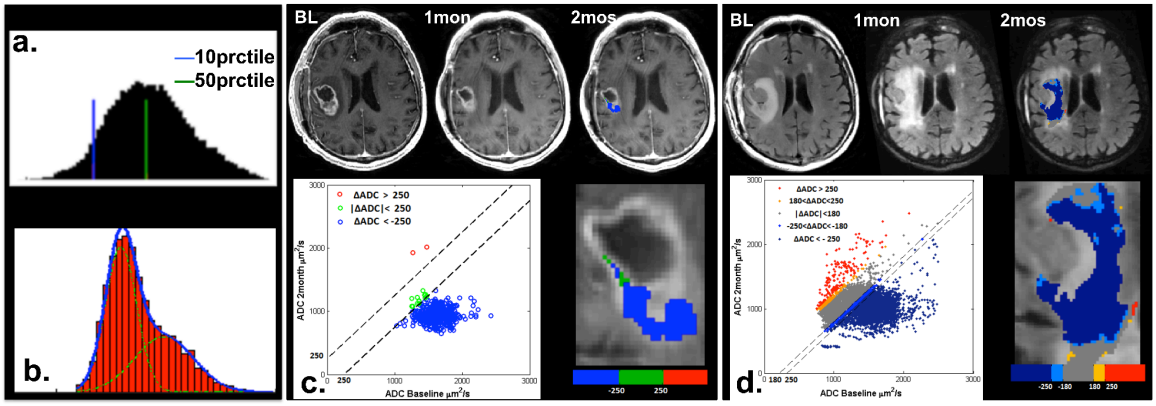

Figure 2-1 Illustration of methods for analyzing ADC: (a) percentile values extracted from the histogram of ADC values in the T2L. (b) 2-mixture normal distribution fitting on ADC histograms in CEL. (c) Traditional fDMs within the CEL overlaid on a T1 post-contrast image at 2 months with scatter plot of the distribution of ADC changes for the entire CEL. (d) Graded fDMs within the T2L overlaid on a FLAIR image at 2months with scatter plot of the distribution of ADC changes for the entire T2L.

2.2.2.1 Histogram Analysis within the T2L And CEL

In regions of interest corresponding to T2Ls at time points up to 8 months after the start of treatment, ADC histograms followed an approximately normal distribution and were characterized using percentile values (Figure 2-1a). In this case the 10^{th} and 50^{th} percentiles were chosen for subsequent analysis to represent regions with more aggressive tumor. At baseline, histograms of the ADC within the CEL were also fit with a 2-mixture normal distribution (Figure

2-1b). Mean values for the lower peak (ADC_L) and the lower curve proportion (LCP) were calculated in the manner proposed by Pope et al. [17].

2.2.2.2 Functional Diffusion Map

For fDM analysis, ADC maps at baseline and 2 months were co-registered using an affine registration with 12 degrees of freedom to ensure adequate alignment (http://www.fmrib.ox.ac.uk/fsl/). Voxel-wise subtraction was performed between 2 months and baseline ADC maps. Both traditional fDMs (Figure 2-1c) [20] and graded fDMs (Figure 2-1d) [25] were generated. Due to the fact that our data were acquired at a field strength of 3T than 1.5T as was used for these earlier studies, a set of new thresholds were generated in the same way as described in the literature [21,24,25]. For each patient, the volume of tissue showing decreased ADC ($Vol_{\Delta ADC}$), as well as the normalized volume showing decreased ADC within the CEL and T2L ($\%Vol_{\Delta ADC}$, which was normalized against the overlapping lesion volume), were calculated.

2.2.3 Statistical Analysis

Both univariate and multivariate Cox Proportional Hazards (CoxPH) model with covariates of baseline KPS, age, and extent of resection (0-biopsy, 1-subtotal, 2-grosstotal) were employed to evaluate the relationship of the fitted parameters to progression-free survival (PFS) and overall survival (OS), landmarked from the scan date of the diffusion parameters. In the case of no progression or death, the event time was censored at the date of last contact. Classification and regression tree (CART) analysis was utilized to determine the cut-off for dichotomizing the fitted parameters [28]. Kaplan-Meier survival curves for each subgroup determined by the CART split points were compared using a log-rank test. Owing to the exploratory nature of the study, no formal adjustment of type I error was undertaken. In all cases, $p<0.05$ was considered statistically significant (Matlab 2012a).

2.3 Results

2.3.1 Clinical

Median OS was 86.1 weeks with 9 patients censored and median PFS was 56.1 weeks with 4 patients censored for the 36 patients considered in this analysis, which is consistent with our recent report on a larger population study [5]. At the time of progression, 23 patients had enhancing progressive disease, 11 patients had non-enhancing progressive disease with only enlarged FLAIR lesion volume, and 2 patients died before imaging follow-up. Of the baseline clinical factors (KPS, age, gender and extent of resection), only the extent of resection was significantly associated with OS (Univariate, $p < 0.002$, HR=0.285, 95%CI=0.134-0.608) and PFS (Univariate, $p < 0.006$, HR=0.366, 95%CI=0.179-0.748).

2.3.2 Volumes of Anatomic Lesions

Table 2-1 lists the median and range of T2L and CEL volumes at different time points. There was a noticeable reduction at 1month and 2months in the volumes of both CEL and T2L. When considered as single variable, the volumes of the CEL at 1 month and 2 months were associated with OS ($p < 0.003$, HR=1.22 at 1 month; $p < 0.03$, HR=1.37 at 2 months) and PFS ($p < 0.03$, HR=1.11 at 1 month; $p < 0.02$, HR=1.38 at 2 months). When adjusted for clinical factors these associations were no longer significant. The volumes of the T2L were not associated with OS or PFS.

Table 2-1 Volume for Anatomic Lesions [median (min-max) in cc].

	Baseline	1mon	2mon	4mon	6mon	8mon
T2L	30.07 (1.71-142.60)	23.52 (1.51-140.42)	9.55 (0.05-41.64)	10.64 (0.28-43.55)	13.72 (0.37-46.35)	14.93 (0.12-44.17)
CEL	3.12 (0.19-21.94)	1.22 (0-17.65)	1.08 (0-7.2)	0.08 (0-3.13)	0.12 (0-1.93)	0.03 (0-4.02)

2.3.3 Histogram Analysis

Within the T2L, the CoxPH model coefficients showed a significant association for values of $ADC_{10\%}$ and $ADC_{50\%}$ with OS and PFS (Table 2-2). A lower ADC percentile value within the T2L indicated a poorer prognosis. The $ADC_{10\%}$ at 2months (post-RT) was associated with PFS (univariate CoxPH, $p<0.03$, HR=0.52, 95%CI=0.29-0.93) and OS (univariate CoxPH, $p < 0.01$, HR=0.37, 95%CI=0.18-0.79). Adjusting for baseline KPS, age, extent of resection, Cox regression analysis confirmed that lower $ADC_{10\%}$ within T2L at 2 months is still a risk factor for OS (multivariate CoxPH, $p < 0.001$, HR=0.11, 95%CI=0.03-0.41) and PFS (multivariate CoxPH, $p < 0.007$, HR=0.31, 95%CI=0.13-0.72). Serial ADC percentile changes of two age-matched patients who both had large T2L at baseline are shown in Figure 2-2. One patient progressed early and the other was stable and completed therapy after being on treatment for 12 months. T2L and ADC were significantly reduced in both cases immediately following onset of therapy (Figure 2-2a). At post-RT, T2L volumes were comparable for both patients, but ADC percentage values were much lower in the patient who progressed early than the patient who was stable (Figure 2-2b). Figure 2-2c shows profiles of ADC histograms within T2L and CEL over time.

Table 2-2 Summary of multivariate CoxPH results with adjustment for KPS, age and extent of resection.

Type	Parameters considered	Time Point	OS		PFS	
			p-val	HR	p-val	HR
Lesion size	Vol_{CEL} (cc)	BL	0.315	0.95 [0.87 1.05]	0.900	0.99 [0.92 1.08]
		2mos	0.301	1.23 [0.83 1.81]	0.201	1.26 [0.89 1.79]
	Vol_{T2L} (cc)	BL	0.431	0.99 [0.98 1.01]	0.837	1.00 [0.99 1.15]
		2mos	0.326	1.03 [0.97 1.10]	0.421	1.02 [0.97 1.07]
Histogram – 2-mixture normal fitting	ADC_L	BL	0.91	1.01 [0.80 1.29]	0.75	0.95 [0.79 1.18]
Histogram – Percentiles in the T2L	$ADC_{10\%}$ ($\mu m^2/s$ /100)	BL	0.116	0.77 [0.55 1.07]	***0.032****	0.69 [0.50 0.97]
		1mos	0.188	0.54 [0.21 1.36]	***0.014****	0.39 [0.18 0.83]
		2mos	***0.001****	0.11 [0.03 0.41]	***0.007****	0.31 [0.13 0.72]
		4mos	***0.005****	0.43 [0.23 0.78]	***0.024****	0.54 [0.32 0.92]
	$ADC_{50\%}$	4mos	***0.011****	0.61 [0.42 0.89]	***0.045****	0.73 [0.54 0.99]
Traditional fDM in T2L	$Vol_{\Delta ADC<-250}$ (cc)	BL-1mos	0.927	0.99 [0.82 1.20]	0.963	1.00 [0.84 1.20]
		BL-2mos	0.552	1.13 [0.75 1.70]	0.603	1.09 [0.78 1.54]
Graded fDM In T2L	$Vol_{250<\Delta ADC<-180}$	BL-1mos	0.489	0.486 [0.06 3.76]	0.577	0.63 [0.13 3.16]
		BL-2mos	0.347	2.36 [0.39 14.19]	0.481	1.65 [0.41 6.71]

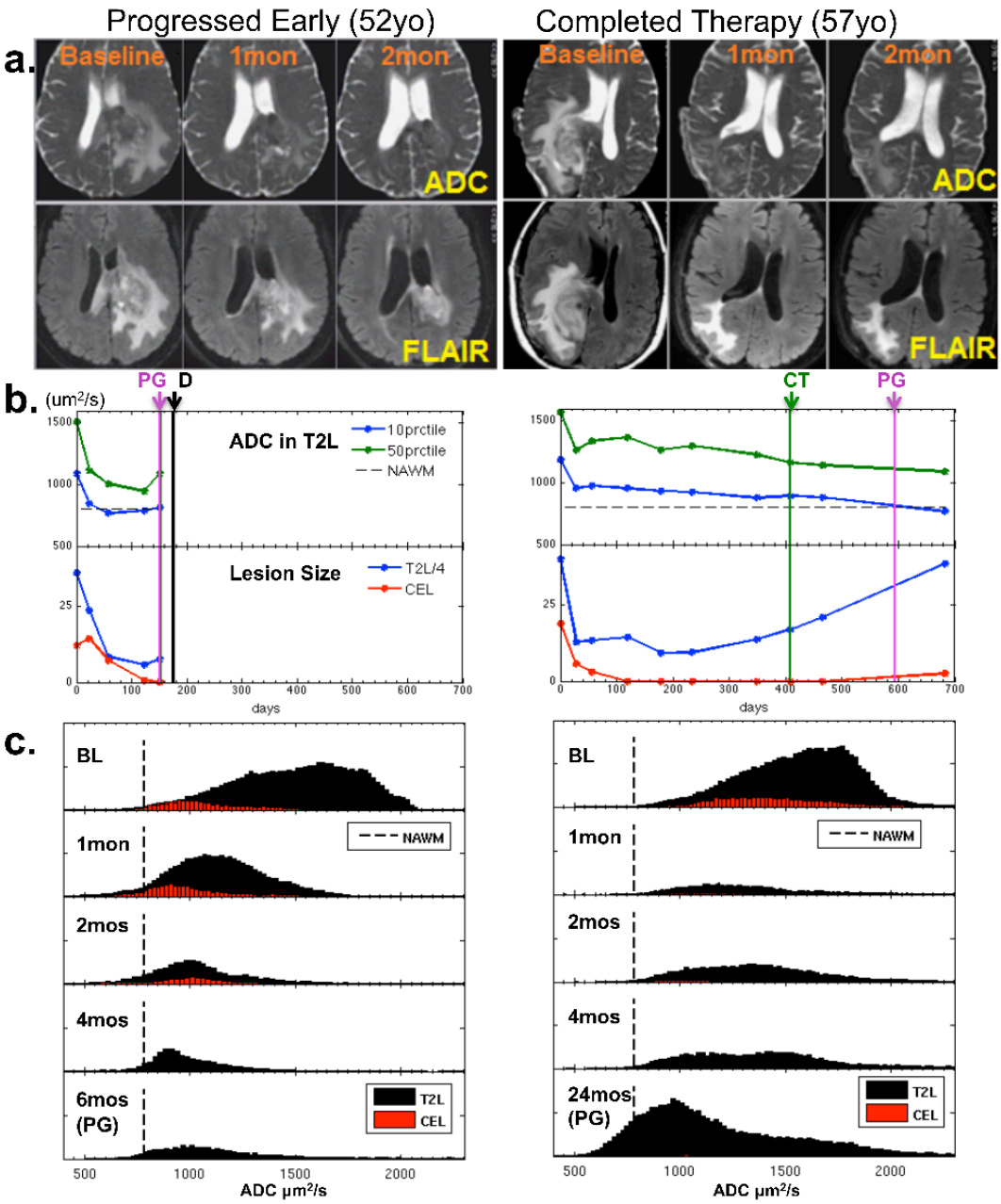

Figure 2-2 Comparison of serial displays for two patients (left – progressed early, right – completed therapy without signs of progression) who both had large T2L at baseline. T2L and ADC were significantly reduced in both patients immediately following onset of therapy. At post-RT, residual T2Ls were comparable for both patients, but ADC percentage values were much lower in the patient who progressed early than the patient who was stable. (a) ADC and FLAIR images at baseline, 1 month and 2 months. (b) Serial display of ADC percentiles and lesion sizes. (PG – progression. CT – completed therapy. D – deceased.). (c) Serial display of ADC histograms in T2L and CEL lesions.

A cutoff value of 853μm^2/s at the 2 month time point was determined by CART analysis to differentiate patients into two groups based on OS (log-rank, p=0.00048) (Figure 2-3a), and a cutoff value of 853μm^2/s based on PFS (log-rank, p=0.02) (Figure 2-3b). The mean and standard deviation for $ADC_{10\%}$ over time for each split group is shown in Figure 2-3c. At baseline, no parameters from the 2-mixture normal fitting were found to be associated with either OS or PFS (p>.1).

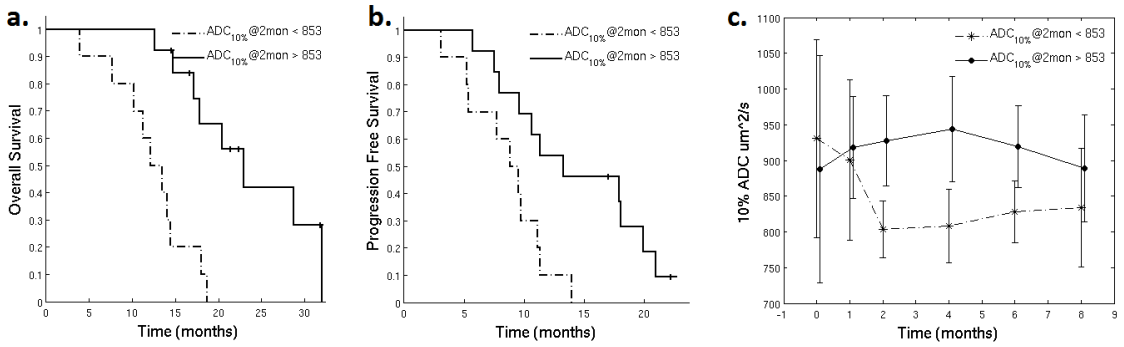

Figure 2-3 Stratification of patients based on CART analysis of $ADC_{10\%}$ in T2L at 2 months. (a) Kaplan-Meier curves for each group when split on CART threshold at 2 months for OS with $ADC_{10\%}$ < 853μm^2/s in dash line (12 patients), $ADC_{10\%}$ > 853μm^2/s in solid line (13 patients). (b) Kaplan-Meier curves for each group when split on CART threshold at 2 months for PFS with $ADC_{10\%}$ < 853μm^2/s in dash line (12 patients), $ADC_{10\%}$ > 853μm^2/s in solid line (13 patients). (c) The mean and standard deviation for $ADC_{10\%}$ over time for each CART split group.

2.3.4 fDM

The traditional fDM technique typically applies a single ΔADC threshold to classify voxels into increasing or decreasing ADC. The 95% confidence interval for defining normal-appearing white and grey matter was 250μm^2/s for our protocol. For graded fDMs, the 95% confidence interval for defining normal-appearing white matter was 180μm^2/s for our data set.

Within the CEL, the recommended minimum overlapping CEL volume that should be considered is 4cc for traditional fDM [20]. In this study, due to the strong anti-angiogenic effect, none of our patients had an overlapping CEL larger than 4cc. Without consideration of this criteria, the traditional fDM and graded fDM analyses within the CEL provided parameters that were associated with OS and PFS ($Vol_{\Delta ADC<-250}$ with OS, $p < 0.003$; HR = 9.52; $Vol_{-250<\Delta ADC<-180}$ with OS, $p < 0.03$, HR = 15509; with PFS $p < 0.03$, HR = 23775). However, these were not significant when adjusting for clinical factors. Within the T2L, none of these parameters were found to be associated with OS or PFS (Table 2).

2.4 Discussion

Although bevacizumab has been shown to reduce the volume of the contrast enhancing and T2 lesions after the initiation of therapy, the highly variable response and limited improvement in overall survival times highlight the need for identifying alternative parameters that can more accurately predict treatment outcomes. Diffusion imaging techniques are dependent on the microscopic structure of tissue, and are sensitive to cell density and necrosis as well as vasogenic edema. It is for this reason that analysis of the ADC maps has been proposed as a method for providing information about the properties of both enhancing and non-enhancing tumor.

Consistent with previous report for patients treated with bevacizumab [1-4], there were reductions in the volumes of the CEL and T2L at 1 and 2 month follow-up scans (Table 1), and the CEL volume was associated with survival as a univariate variable [29]. However, this association was no longer significant when adjusting for clinical factors, suggesting that the CEL volume does not add value in addition to clinical factors in relation to survival. We would like to note that due to the strong anti-leakage effect of bevacizumab, over half patients demonstrated CEL volume < 1cc at 2 month, and 1/3 patients had non-enhancing progressive disease. All these motivated us to look more closely at the T2L as the region of interest for imaging biomarkers.

Regions within T2L with low ADC values are thought to correspond to regions of higher cellularity, while regions with increased ADC to correspond to vasogenic edema [32-34]. Both of these opposing effects are present within the tumor microenvironment and may therefore counteract each other. In tumors being actively treated with bevacizumab, vasogenic edema is more effectively controlled [30], resulting in a reduction in the volume of the T2L and lower ADC values that may more closely reflect the cellularity of the tumor. Our results support this hypothesis by indicating that lower ADC percentiles within the T2L at 2 months time window were significant risk factors for both PFS and OS. Two factors that could influence ADC values in the earlier and later time window and confound the interpretation of the data are ischemia that results from the surgical resection and RT-induced edema. Regions of ischemia occur around the resection cavity may result in temporarily reduced ADC values that typically return to normal within 90 days [31]. Regions of reduced ADC that are observed during this early time frame should therefore be interpreted with caution, as they may be confused with recurrent tumor. In the later time frame (e.g. post-4mon), increases in edema that occur during RT may result in higher ADC values, which could mask the presence of tumor. With bevacizumab, the confounding effects from surgery and during RT appear to have resolved at 2 month, so that the ADC values provided a more accurate representation of residual tumor. At subsequent time points, reactive edema associated with growing tumor may result in elevated ADC (Figure 2-3C). Another potential confounding factor is gelatinous necrosis, which could cause persistent restricted diffusion in bevacizumab treated patients [35-36]. Caution must be exerted in interpreting restricted diffusion because it has been reported that patients who demonstrated such bevacizumab caused necrosis had longer survival [35]. The average time of detecting such necrosis with diffusion was 8 months, therefore it is unlikely to have developed by the 2 month follow-up in our study (6 weeks into bevcizumab). We hypothesize that it is for these reasons that the 2 months (post-RT) time point appeared to be the best time point for using ADC to assess residual tumor.

Although previous studies have shown that the two normal distribution mixture curve analysis of pre-surgery ADC histograms in the CEL can predict response to bevacizumab for patients with newly diagnosed GBM [19], we were unable to detect an association for our patient population. This may have been due to our baseline data having been post-surgery and therefore lacking information about the resected tumor and/or being influenced by surgically-induced ischemia.

The fDM analysis was developed to examine voxel-wise changes in ADC in the patient over time. Our results showed that the fDM analysis of higher volumes of tissue within the CEL that showed decreased ADC were associated with worse PFS and OS when considered without adjustment for clinical factors. While this may be a less sensitive metric than others, the finding is consistent with areas of reduced diffusion corresponding to more cellular tumor and hence inferring a worse outcome. The global reduction in ADC metrics that we observed within the T2L is likely to be due to reabsorption of edema after treatment.

Despite the promising results obtained in this study using fDM analysis, there are limitations that should be taken into account in patients treated with bevacizumab in the up-front setting. First, the CEL volumes of all patients in this study were smaller than the minimum recommended size (4cc) to be considered for the traditional fDM [20]. A second limitation is in the accuracy of the image registration methods used to align serial ADC images. Significant tissue shifts were observed in some of our patients after initial of therapy, mainly because of the reduction in edema caused by the anti-angiogenic agent, which reduces the intracranial pressure. In these cases, accurate tissue matching between different time points can be challenging, even with non-linear registration.

In conclusion, our study emphasizes the value of ADC metrics for early assessment of residual tumor in patients with newly diagnosed GBM being treated with a combination of

therapy that includes bevacizumab. While there was a rapid decline of ADC percentile values immediately following onset of therapy in almost all subjects, the ADC percentile values were lower for the patients who progressed early. This suggests that tracking the changes in ADC using serial histogram analysis as shown in Figure 2-2 could potentially assist radiologists in monitoring patient response to therapy that includes bevacizumab. Our results highlighted the value of $ADC_{10\%}$ within the T2L at the post-RT exam in conjunction with standard clinical factors in predicting PFS and OS. We hypothesize that this is due to the anti-angiogenic effect of bevacizumab reducing the extent of vasogenic edema at this time point and therefore allowing the observed ADC values to more accurately reflect the residual tumor burden.

2.5 References

1. Friedman HS, Prados MD, Wen PY, Mikkelsen T, Schiff D, Abrey LE, Yung W.K., Paleologos N, Nicholas MK, Jensen R, Vredenburgh J, Huang J, Zheng M, and Cloughesy T. Bevacizumab alone and in combination with irinotecan in recurrent glioblastoma. J Clin Oncol 2009;27:4733-40.
2. Kreisl TN, Kim L, Moore K, Duic P, Royce C, Stroud I, Garren N, Mackey M, Butman JA, Camphausen K, Park J, Albert PS, Fine HA. Phase II trial of single-agent bevacizumab followed by bevacizumab plus irinotecan at tumor progression in recurrent glioblastoma. J Clin Oncol 2009;27:740-45.
3. Nghiemphu PL, Liu W, Lee Y, Than T, Graham C, Lai A, Green RM, Pope WB, Liau LM, Mischel PS, Nelson SF, Elashoff R, Cloughesy TF. Bevacizumab and chemotherapy for recurrent glioblastoma: a single-institution experience. Neurology. 2009;72:1217-22.
4. Lai A, Tran A, Nghiemphu PL, Pope WB, et al. Phase II study of bevacizumab plus temozolomide during and after radiation therapy for patients with newly diagnosed glioblastoma multiforme. J Clin Oncol. 2011 Jan 10;29(2):142-8.
5. Clarke JL, Molinaro AM, Phillips JJ, Butowski NA, Chang SM, Perry A, Costello JF, Desilva AA, Rabbitt JE, Prados MD. A single-institution phase II trial of radiation, temozolomide, erlotinib, and bevacizumab for initial treatment of glioblastoma. Neuro Oncol. 2014 Mar 16.
6. Mark R. Gilbert, James J. Dignam, Terri S. Armstrong, et al. A Randomized Trial of Bevacizumab for Newly Diagnosed Glioblastoma. N Engl J Med 2014; 370:699-708.
7. Olivier L. Chinot, Wolfgang Wick, Warren Mason, et al. Bevacizumab plus Radiotherapy–Temozolomide for Newly Diagnosed Glioblastoma. N Engl J Med 2014; 370:709-722.

8. Quant EC, Norden AD, Drappatz J, Muzikansky A, Doherty L, Lafrankie D, Ciampa A, Kesari S, Wen PY. Role of a second chemotherapy in recurrent malignant glioma patients who progress on bevacizumab. Neuro Oncol. 2009;11: 550-555.
9. Pope WB, Lai A, Nghiemphu P, Mischel P, Cloughesy TF. MRI in patients with high-grade gliomas treated with bevacizumab and chemotherapy. Neurology 2006;66:1258-60.
10. Wen PY, Macdonald DR, Reardon DA, Cloughesy TF, Sorensen AG, Galanis E, Degroot J, Wick W, Gilbert MR, Lassman AB, Tsien C, Mikkelsen T, Wong ET,Chamberlain MC, Stupp R, Lamborn KR, Vogelbaum MA, van den Bent MJ, Chang SM. Updated response assessment criteria for high-grade gliomas: response assessment in neuro-oncology working group. J Clin Oncol 2010;28:1963-72.
11. Clarke JL, Chang S. Pseudoprogression and pseudoresponse: challenges in brain tumor imaging. Curr Neurol Neurosci Rep 2009; 9:241-46.
12. Le Bihan D, Breton E, Lallemand D, Aubin ML, Vignaud J, Laval-Jeantet M. Separation of diffusion and perfusion in intravoxel incoherent motion MR imaging. Radiology 1988; 168:497-505.
13. Lu S, Ahn D, Johnson G, Cha S. Peritumoral diffusion tensor imaging of high-grade gliomas and metastatic brain tumors. AJNR Am J Neuroradiol. 2003;24:937-41.
14. Nelson SJ. Assessment of therapeutic response and treatment planning for brain tumors using metabolic and physiological MRI. NMR Biomed. 2011;24:734-49.
15. Li Y, Lupo JM, Polley MY, Crane JC, Bian W, Cha S, Chang S, and Nelson SJ. Serial analysis of imaging parameters in patients with newly diagnosed glioblastoma multiforme. Neuro Oncol. 2011;13:546-57.
16. Saraswathy S, Crawford FW, Lamborn KR, Pirzkall A, Chang S, Cha S, Nelson SJ. Evaluation of MR markers that predict survival in patients with newly diagnosed GBM prior to adjuvant therapy. J Neurooncol. 2009;91:69-81.

17. Pope WB, Kim HJ, Huo J, Alger J, Brown MS, Gjertson D, Sai V, Young JR, Tekchandani L, Cloughesy T, Mischel PS, Lai A, Nghiemphu P, Rahmanuddin S,Goldin J. Recurrent glioblastoma multiforme: ADC histogram analysis predicts response to bevacizumab treatment. Radiology 2009;252:182-89.

18. Pope WB, Qiao XJ, Kim HJ, Lai A, Nghiemphu P, Xue X, Ellingson BM, Schiff D, Aregawi D, Cha S, Puduvalli VK, Wu J, Yung WK, Young GS, Vredenburgh J,Barboriak D, Abrey LE, Mikkelsen T, Jain R, Paleologos NA, Rn PL, Prados M, Goldin J, Wen PY, Cloughesy T. Apparent diffusion coefficient histogram analysis stratifies progression-free and overall survival in patients with recurrent GBM treated with bevacizumab: a multi-center study. J Neurooncol. 2012;108:491-8.

19. Pope WB, Lai A, Mehta R, Kim HJ, Qiao J, Young JR, Xue X, Goldin J, Brown MS, Nghiemphu PL, Tran A, Cloughesy TF. Apparent diffusion coefficient histogram analysis stratifies progression-free survival in newly diagnosed bevacizumab-treated glioblastoma. AJNR Am J Neuroradiol. 2011;32:882-9.

20. Moffat BA, Chenevert TL, Lawrence TS, Meyer CR, Johnson TD, Dong Q, Tsien C, Mukherji S, Quint DJ, Gebarski SS, Robertson PL, Junck LR, Rehemtulla A,Ross BD. Functional diffusion map: a noninvasive MRI biomarker for early stratification of clinical brain tumor response. Proc Natl Acad Sci USA 2005;102:5524-5529.

21. Moffat BA, Chenevert TL, Meyer CR, McKeever PE, Hall DE, Hoff BA, Johnson TD, Rehemtulla A, Ross BD. The functional diffusion map: an imaging biomarker for the early prediction of cancer treatment outcome. Neoplasia 2006; 8:259-267.

22. Hamstra DA, Chenevert TL, Moffat BA, Johnson TD, Meyer CR, Mukherji SK, Quint DJ, Gebarski SS, Fan X, Tsien CI, Lawrence TS, Junck L, Rehemtulla A, Ross BD. Evaluation of the functional diffusion map as an early biomarker of time-to-progression and overall survival in high-grade glioma. Proc Natl Acad Sci USA 2005;102:16759-16764.

23. Hamstra DA, Galbán CJ, Meyer CR, Johnson TD, Sundgren PC, Tsien C, Lawrence TS, Junck L, Ross DJ, Rehemtulla A, Ross BD, Chenevert TL. Functional diffusion map as an early imaging biomarker for high-grade glioma: correlation with conventional radiologic response and overall survival. J Clin Oncol 2008;26:3387-3394.
24. Ellingson BM, Malkin MG, Rand SD, Connelly JM, Quinsey C, LaViolette PS, Bedekar DP, Schmainda KM.Validation of functional diffusion maps (fDMs) as a biomarker for human glioma cellularity. J Magn Reson Imaging 2010;31:538-48.
25. Ellingson BM, Cloughesy TF, Lai A, Mischel PS, Nghiemphu PL, Lalezari S, Schmainda KM, Pope WB. Graded functional diffusion map-defined characteristics of apparent diffusion coefficients predict overall survival in recurrent glioblastoma treated with bevacizumab. Neuro Oncol. 2011;13:1151-61.
26. Ellingson BM, Malkin MG, Rand SD, LaViolette PS, Connelly JM, Mueller WM, Schmainda KM. Volumetric analysis of functional diffusion maps is a predictive imaging biomarker for cytotoxic and anti-angiogenic treatments in malignant gliomas. J Neurooncol. 2011;102:95-103.
27. Saraswathy S, Crawford F, Nelson SJ. Semi-automated segmentation of brain tumor lesions in MR images. In: 14th Annual Meeting of ISMRM; 2006; Abstract 1609.
28. Therneau TM, Atkinson EJ. An introduction to recursive partitioning using the RPART routines. Technical Report. Mayo Foundation, 1997.
29. Ellingson BM1, Kim HJ, Woodworth DC, Pope WB, Cloughesy JN, Harris RJ, Lai A, Nghiemphu PL, Cloughesy TF. Recurrent glioblastoma treated with bevacizumab: contrast-enhanced T1-weighted subtraction maps improve tumor delineation and aid prediction of survival in a multicenter clinical trial. Radiology. 2014;271(1):200-10.
30. Ananthnarayan S, Bahng J, Roring J, Nghiemphu P, Lai A, Cloughesy T, Pope WB. Time course of imaging changes of GBM during extended bevacizumab treatment. J Neurooncol. 2008;88(3):339-47.

31. Smith JS, Cha S, Mayo MC, McDermott MW, Parsa AT, Chang SM, Dillon WP, Berger MS. Serial diffusion-weighted magnetic resonance imaging in cases of glioma: distinguishing tumor recurrence from postresection injury. 2005;103(3):428-38.
32. Kono K, Inoue Y, Nakayama K, et al. The role of diffusion-weighted imaging in patients with brain tumors. AJNR Am J Neuroradiol. 2001;22:1081-1088.
33. Guo AC, Cummings TJ, Dash RC, Provenzale JM. Lymphomas and high-grade astrocytomas: comparison of water diffusibility and histologic characteristics. Radiology. 2002;224:177-183.
34. Muti M, Aprile I, Principi M, Italiani M, Guiducci A, Giulianelli G, Ottaviano P. Study on the variations of the apparent diffusion coefficient in areas of solid tumor in high grade gliomas. Magn Reson Imaging. 2002;20:635-641.
35. Mong S, Ellingson BM, Nghiemphu PL, Kim HJ, Mirsadraei L, Lai A, Yong W, Zaw TM, Cloughesy TF, Pope WB. Persistent diffusion-restricted lesions in bevacizumab-treated malignant gliomas are associated with improved survival compared with matched controls. AJNR Am J Neuroradiol. 2012;33(9):1763-70.
36. Gerstner ER, Frosch MP, Batchelor TT. Diffusion magnetic resonance imaging detects pathologically confirmed, nonenhancing tumor progression in a patient with recurrent glioblastoma receiving bevacizumab. J Clin Oncol 2010;28:91–93
37. Gupta A, Young RJ, Karimi S, Sood S, Zhang Z, Mo Q, Gutin PH, Holodny AI, Lassman AB. Isolated diffusion restriction precedes the development of enhancing tumor in a subset of patients with glioblastoma. AJNR Am J Neuroradiol 2011;32:1301–06

Chapter 3

Changes in Diffusion and Anatomic Imaging Parameters and their association with Survival Vary with Treatment Regimen for Patients with Newly Diagnosed Glioblastoma

This chapter extends the ADC analysis methodology from the previous chapter to the analysis two additional clinical trials. It compares the associations of lesion volumes and ADC metrics to patient outcomes in different patient cohorts. The results highlight distinct patterns of change in lesion volumes and ADC parameters in patients who were treated with the combined therapy that included bevacizumab.

3.1 Introduction

Glioblastoma (GBM) is the most malignant primary brain tumor in adults. The standard of care for patients with newly diagnosed GBM consists of surgery, radiotherapy and temozolomide (TMZ). In a definitive phase III trial, patients treated with TMZ plus radiotherapy (RT) had significantly improved overall survival (OS), compared with patients who received RT alone [1]. Despite the use of this multi-modality treatment, the 2-year survival rate for patients treated was only 26.5%, with the median overall survival being around 15 months. A number of additional therapeutic agents are being considered with the goal of improving outcomes for patients with GBM.

Enzastaurin is a protein kinase C β-inhibitor that has been reported to have both direct antitumor effect, through suppression of tumor cell proliferation and induced apoptosis, and indirect effects, through inhibition of tumor-induced angiogenesis [2]. Although its mechanism of action is not yet fully understood, pre-clinical reports have shown that enzastaurin and radiation are synergistic and that when combined are able to induce apoptosis in glioma models [3]. These

data provided the rationale for a Phase II clinical trial of RT, TMZ and enzastaurin in patients with newly diagnosed GBM.

With the discovery that vascular endothelial growth factor (VEGF) is a major driver of tumor angiogenesis [4], recent efforts have focused on novel therapeutics that inhibit its activity. Bevacizumab is a humanized monoclonal VEGF-blocking antibody that has been shown to normalize vascular permeability and regulate angiogenesis in patients with GBM. A phase II trial of bevacizumab alone or in combination with irinotecan for patients with recurrent GBM reported a dramatic improvement in PFS and a high response rate [5]. This led to the proposal that the use of adjuvant bevacizumab in combination with standard radio- and chemotherapy would act to normalize tortuous tumor vasculature and improve delivery of chemotherapeutics and oxygen [6].

While adjuvant anti-angiogenic therapy has been associated with increased time to progression, reports from recent phase II/III trials have indicated that it is unable to improve overall survival for newly diagnosed GBM. This has highlighted the difficulties in using conventional imaging methods to evaluate response to therapy for such agents [7-9]. The assessment of response to bevacizumab is especially problematic, because it directly affects the size of the contrast-enhancing lesion (CEL) by reducing the permeability of the vasculature to gadolinium-based agents but does not necessarily signify that there is a reduction in bulk tumor [9]. Another complication is that there have been reports of increased tumor invasiveness following treatment failure in patients receiving bevacizumab, which is expressed as an increase in the size of the region of T2 hyperintensity (T2L) [11]. Although the Response Assessment in Neuro-Oncology (RANO) criteria integrate changes in the T2L into the definition of response [10], it is not clear whether such changes are specific to recurrent tumor or represent non-specific radiation-induced white matter changes. This provides strong motivation for seeking alternative imaging biomarker that can help to resolve these ambiguities.

The apparent diffusion coefficient (ADC) is a parameter derived from diffusion weighted MR imaging that reflects changes in water mobility and is therefore sensitive to the variations in tissue composition and architecture. It has been proposed as a metric for assessing changes in normal tissue, as well as monitoring treatment efficacy for patients with GBM. The ADC is sensitive to a number of structural alterations in tumor that include increase in tumor cellularity, formation of necrosis, and the presence of vasogenic edema.

Pretreatment and early changes in ADC metrics have been reported as predictors of response to therapy in human brain tumors [18-26], but the analysis of their associations with survival have been more variable. In patients with recurrent GBM, the analysis of pretreatment ADC histograms was shown to be predictive of survival after treatment with bevaciuzmab but not with temozolomide [17]. It was also shown that patients with tumors responding favorably to RT plus TMZ show an increase in ADC values shortly after treatment [20-23,18], and those that respond favorably to RT plus enzastaurin have higher ADC within the contrast-enhancing lesion [19]. In the recurrent setting, patients treated with bevacizumab who exhibit a change in ADC (either decrease or increase) have worse overall survival than those who show no change in ADC [20]. Our recent study of patients with newly diagnosed GBM being treated with RT plus TMZ, erlotinib and bevacizumab evaluated the association of different ADC metrics with survival and highlighted the value of parameters from the T2L at the post-RT examination in predicting outcome [21].

The ambiguities in findings from studies of changes in lesion volumes and ADC metrics for patient receiving different types of treatments have created uncertainties about when and how to interpret these early markers of treatment efficacy. The purpose of this study was to compare the patterns of early changes in imaging parameters for populations of patients with newly diagnosed GBM who had been treated with three different regimens using consistent data acquisition and analysis methodologies. These treatments were (1) temozolomide plus RT (TMZ), (2)

temozolomide plus RT with enzastaurin (TMZ+enza) and (3) TMZ plus RT with bevacizumab and erlotinib (TMZ+bev). The imaging time points included baseline, mid-RT and post-RT scans, with clinical outcomes of progression free survival (PFS) and overall survival (OS).

3.2 Materials and Methods

3.2.1 Study Population

A total of 96 patients with newly diagnosed GBM (WHO Grade IV) who had agreed to have research imaging examinations during the course of treatment were evaluated in this study. Patients received surgical resection and were treated with standard care of RT concurrently with TMZ (TMZ cohort, 31 patients), TMZ and enzastaurin (TMZ+enza cohort, 35 patients), or TMZ, erlotinib and bevacizumab (TMZ+bev cohort, 30 patients). Patients were required to have a Karnofsky performance score (KPS) of $\geq$ 60 in order to be treated in this manner and provide informed consent for participation in the imaging studies as approved by the Committee on Human Research at our institution. Figure 3-1B describes the baseline characteristics of these three patient populations.

A

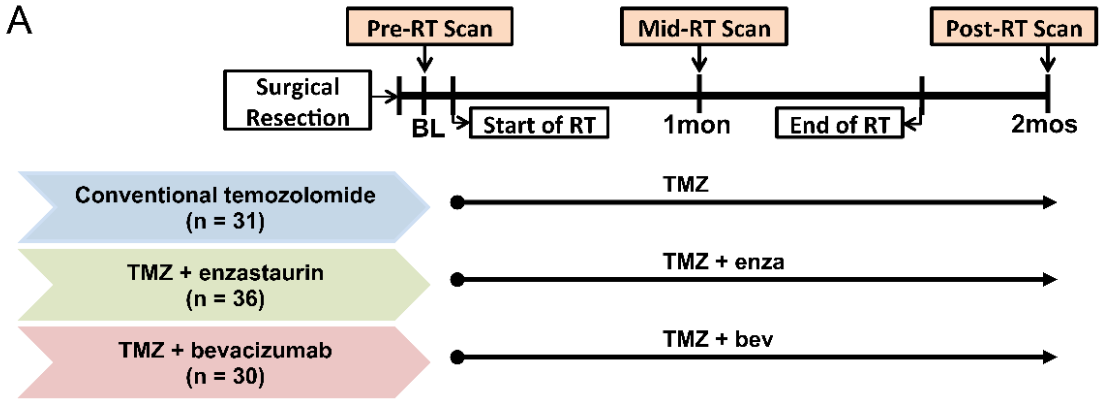

B

	#Patients	Age	Gender	Surgery			KPS
		Median (range)	M/F	Biopsy	Sub-total	Gross-total	Median (range)
TMZ	31	52 (38-77)	19/12	2	14	15	90 (80-100)
TMZ+enza	35	57 (25-70)	27/8	5	20	10	90 (70-90)
TMZ+bev	30	52 (21-76)	14/16	5	15	8	90 (60-100)

C

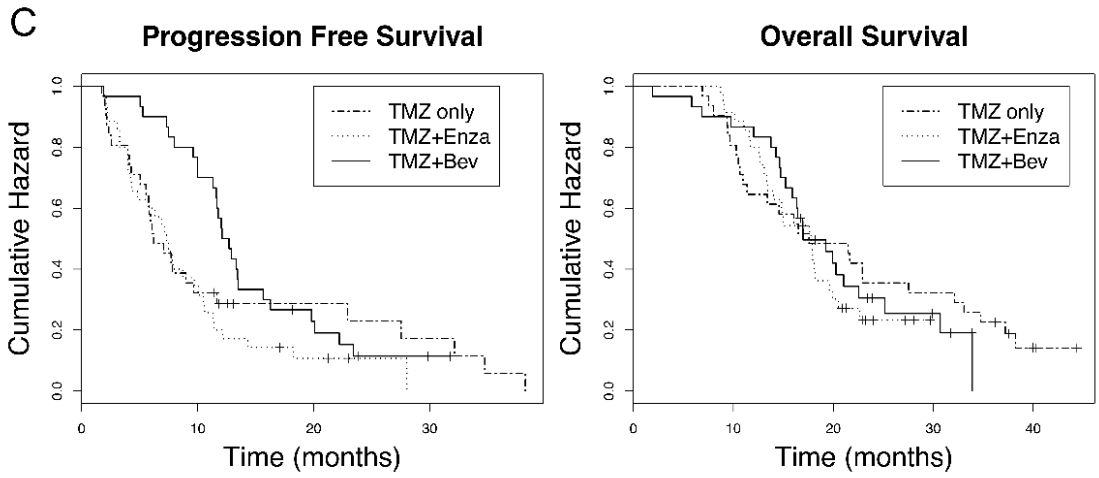

Figure 3-1 (A) Treatment schema for the three patient cohorts. (B) baseline characteristics. (C) The Kaplan-Meier curves of progression free survival (PFS) and overall survival (OS). Median PFS values were 6.2 months, 7.3 months and 12.4 months, while Median OS values were 17.6 months, 17.8 months and 17.0 months respectively. Log-rank tests showed that PFS was significantly longer in the TMZ+bev cohort than in the TMZ+enza cohort, and no significant OS differences between the three cohorts.

The treatment schema for the three separate patient cohorts is seen in Figure 3-1A. Within 5 weeks of diagnosis, patients began treatment with fractionated RT (total dose of 60 Gy) and 75

mg/m^2 of TMZ given daily over a period of 6 weeks. Patients in the TMZ+enz cohort were administered enzastaurin (250 mg daily) concurrent with the other treatments. Patients in the TMZ+bev cohort received erlotinib (150 mg/day continuously or 500 mg/day continuously if on anti-epileptic drugs) starting on day 1 of RT and received bevacizumab at a dose of 10 mg/kg IV every 14 days starting in week 2 of radiotherapy. MRI exams considered in the analysis were performed at three time-points: (1) following surgical resection or biopsy but prior to RT (pre-RT); (2) between 3 and 5 weeks into treatment (mid-RT); and, (3) within 2 weeks after completion of RT (post-RT). Patients in the TMZ cohort did not have a mid-RT scan.

Criteria for defining true progression were clinical deterioration and/or radiological progression, which was based upon changes in cross-sectional diameters of the contrast-enhancing lesion (CEL) as defined by McDonald criteria for TMZ and TMZ+enza cohorts [22], and by RANO criteria for the TMZ+bev cohort, which integrates changes in the T2-hyperintensity lesion (T2L) into the definition of response [10]. When tumor progression was suspected, patients received an additional scan at a short time interval (~1 month) to help in confirming true progression.

3.2.2 MR Imaging and Post-processing

All scans were obtained using a 3T GE MR scanner using the body coil for transmission and an 8-channel phased array coil for reception. Exams included axial T2-weighted fluid attenuated inversion recovery (FLAIR), T1-weighted pre- and post-gadolinium (Gd) spoiled gradient echo (SPGR), and six-directional axial diffusion echo-planar imaging (EPI) (b = 1000 s/mm^2, NEX=4) sequences.

The FLAIR and pre-Gd T1-weighted images were rigidly aligned to the post-Gd T1-weighted images using previously developed software [23]. CEL regions were manually defined on the co-registered post-Gd T1 SPGR images at each available time point. Any enhancement that was also

present on the pre-Gd T1 images was assumed to be indicative of acute blood products and was excluded. The T2L regions were segmented based on the hyper-intensity region of FLAIR images using a semi-automatic method [27]. The resection cavity was excluded from all ROIs.

ADC values were calculated on a voxel-by-voxel basis using software developed in-house based on previously published algorithms [25]. They were compared to anatomical imaging by rigidly aligning the T2-weighted (b=0) diffusion image to the T2-weighted FLAIR and applying the transformation to the ADC maps. ADC parameters that were selected for analysis were the median and 10^{th} percentile from the histogram of values in the T2L and CEL. This choice was based upon our prior analysis of different ADC metrics in the TMZ+bev cohort alone (see Chapter 2), which suggested that they are the most relevant for this type of analysis.

3.2.3 Statistical Analysis

3.2.3.1 Patterns of Changes Between Pre-, Mid-, and Post-RT

Volumes of the CEL and T2L were obtained by multiplying the number of pixels in the region of interest by the pixel dimensions. Histograms of ADC values were estimated within the CEL and T2L regions. Parameters that were used to summarize the shape of the histogram were the 10^{th} and 50^{th} percentiles of the distribution. The percent change in each volume and the ADC values were calculated for three periods: from pre- to mid-RT (pre-mid), as 100 x [mid-pre]/pre; from mid-post RT (mid-post), as 100 x [post-mid]/mid; and from pre- to post-RT (pre-post), as 100 x [post-pre]/pre within the CEL and T2L regions. A Kruskal-Wallis test was employed to assess differences in imaging parameters between the three cohorts. In cases where significance was found, a Wilcoxon rank-sum test was employed to assess differences between any two cohorts.

3.2.3.2 Survival Analysis

OS and PFS were evaluated using Kaplan–Meier survival curves. A log-rank test was used to compare variables among patient cohorts. OS was determined from the day of the baseline scan to the date of death or last contact at which the patient was known to be alive (censored). PFS was defined as the time from the baseline scan to disease progression or death due to any cause, whichever came first. Age, Karnofsky Performance Score (KPS) at baseline, gender and extent of resection (EOR: 0=biopsy, 1=subtotal, 2=gross total) were considered as covariates in the survival analysis.

3.2.3.3 Association of Imaging Parameters and Outcome

Cox proportional hazard (CoxPH) models were used to evaluate which parameters were associated with PFS or OS within each treatment cohort. The differences in survival between groups that were dichotomized by imaging parameters were assessed by log-rank analysis. Multivariate Cox Hazard models were employed with covariates for treatment cohort, imaging parameter, and the interaction between treatment cohort and imaging variable. These models were also adjusted for clinical factors. No formal adjustment of type I error was undertaken because of the exploratory nature of the study; in all cases, $P < .05$ was considered statistically significant. Statistical analyses were performed with R (Version 3.0.3).

3.3 Results

3.3.1 Patients Characteristics and Outcomes

Of the baseline patient characteristics that were considered, only gender was significantly different between TMZ+enza and TMZ+bev cohorts (Table 3-1; rank-sum, p=0.01). Age, KPS, and extent of surgery were not significantly different amongst the three cohorts (Kruskal-Wallis, p>0.1). Kaplan–Meier curves describing PFS and OS are displayed in Figure 3-1C. Median PFS

was 6.2 months in TMZ (95%CI: 5.53-22.9 months), 7.3 months in TMZ+enza (95%CI: 4.89-10.5 months), and 12.4 months in TMZ+bev (95%CI: 11.60-16.3 months). Median OS was 17.6 months in TMZ alone (95%CI: 11.4-33.1 months), 17.8 months in TMZ+enza (95%CI: 14.0-20.5 months), and 17.0 months in TMZ+bev (95%CI: 15.9-25.1 months). Although PFS was significantly longer in the TMZ+bev cohort than in the TMZ+enza cohort (Log-rank test, $p<0.008$), there were no significant differences in OS were among the three cohorts ($p>0.1$).

Table 3-1 Cox proportional hazard analysis of associations between baseline clinical factors, followed by anatomic lesion volumes and 10% ADC at pre-, mid-, and post-RT to progression free survival (PFS) and overall survival (OS) with adjustment for the baseline clinical factors (age, gender, KPS, extent of surgery).

		PFS						**OS**					
		TMZ		**TMZ+Enza**		**TMZ+Bev**		**TMZ**		**TMZ+Enza**		**TMZ+Bev**	
		p-value	*HR (95CI)*	*p-value*	*HR (95CI)*	*p-value*	*HR (95CI)*	*p-value*	*HR (95CI)*	*p-value*	*HR (95CI)*	*p-value*	*HR (95CI)*
Baseline Clinical Factors	*age*	0.42	1.01 [0.98 1.05]	0.27	1.02 [0.99 1.05]	0.08	1.04 [1 1.08]	0.17	1.03 [0.99 1.07]	0.15	1.03 [0.99 1.06]	0.06	1.04 [1 1.08]
	gender	0.99	0.99 [0.45 2.18]	0.57	0.78 [0.33 1.83]	0.91	0.96 [0.44 2.07]	0.63	1.22 [0.54 2.73]	0.82	0.90 [0.36 2.26]	0.86	0.93 [0.4 2.15]
	kps	-	-	0.48	1.03 [0.95 1.12]	0.10	0.96 [0.92 1.01]	0.96	1.00 [0.9 1.1]	0.86	0.99 [0.92 1.08]	0.25	0.97 [0.93 1.02]
	Surgery	0.45	1.26 [0.69 2.29]	0.06	0.53 [0.28 1.03]	***0.006***	0.36 [0.18 0.74]	0.37	1.35 [0.7 2.63]	0.15	0.6 [0.3 1.19]	***0.008***	0.35 [0.16 0.77]
pre-RT	*Vol CEL (cc)*	0.05	1.09 [1 1.2]	0.34	1.02 [0.98 1.07]	0.79	0.99 [0.91 1.07]	0.26	1.07 [0.95 1.2]	0.27	1.03 [0.98 1.08]	0.22	0.94 [0.85 1.04]
	Vol T2L (cc)	0.26	1.01 [0.99 1.03]	0.38	1.01 [0.99 1.02]	0.68	1.00 [0.99 1.01]	0.64	1.00 [0.98 1.03]	0.09	1.01 [1 1.03]	0.29	0.99 [0.98 1.01]
	10%ADC_CEL	0.55	0.92 [0.69 1.22]	0.29	1.16 [0.88 1.52]	0.38	0.9 0 [0.72 1.13]	0.19	0.83 [0.63 1.09]	0.35	1.17 [0.84 1.62]	0.63	0.94 [0.73 1.21]
	10%ADC_T2L	***0.02***	0.51 [0.29 0.9]	0.31	1.15 [0.88 1.5]	***0.02***	0.66 [0.48 0.92]	0.09	0.62 [0.36 1.07]	0.63	1.08 [0.78 1.49]	0.07	0.74 [0.53 1.02]
mid-RT	*Vol CEL (cc)*	-	-	0.19	1.07 [0.97 1.18]	0.8	1.02 [0.89 1.17]	-	-	0.1	1.10 [0.98 1.22]	0.15	1.14 [0.95 1.35]
	Vol T2L (cc)	-	-	0.46	1.01 [0.98 1.03]	0.36	0.99 [0.98 1.01]	-	-	***0.03***	1.03 [1 1.06]	0.57	1.00 [0.98 1.01]
	10%ADC_CEL	-	-	0.66	1.08 [0.78 1.49]	0.08	0.73 [0.52 1.03]	-	-	0.66	1.08 [0.76 1.55]	0.62	0.91 [0.62 1.34]
	10%ADC_T2L	-	-	0.65	0.90 [0.58 1.41]	***0.007***	0.36 [0.17 0.76]	-	-	0.44	0.82 [0.5 1.36]	0.09	0.43 [0.17 1.13]
post-RT	*Vol CEL (cc)*	***0.0001***	1.12 [1.06 1.19]	***0.03***	1.08 [1.01 1.15]	0.15	1.29 [0.91 1.84]	0.05	1.06 [1 1.13]	***0.01***	1.10 [1.03 1.19]	0.51	1.13 [0.78 1.63]
	Vol T2L (cc)	***0.004***	1.02 [1.01 1.03]	0.11	1.02 [1 1.05]	0.21	1.03 [0.98 1.07]	0.32	1.01 [0.99 1.02]	***0.02***	1.03 [1 1.06]	0.75	1.01 [0.96 1.07]
	10%ADC_CEL	0.12	0.78 [0.58 1.07]	0.86	1.03 [0.77 1.37]	0.06	0.54 [0.28 1.03]	0.41	0.88 [0.65 1.2]	0.31	1.18 [0.86 1.63]	0.05	0.45 [0.202 1.01]
	10%ADC_T2L	0.69	0.91 [0.56 1.48]	0.15	1.41 [0.88 2.26]	***0.01***	0.3 [0.13 0.7163]	0.57	0.86 [0.51 1.44]	0.21	1.36 [0.84 2.2]	***0.0005***	0.09 [0.03 0.3551]

3.3.2 Changes from Pre-RT to Post-RT

Changes in median volumes and ADC within the CEL and T2L during the course of RT are illustrated in Figure 3-2A. Mid- and post-RT data were normalized to pre-RT within each patient. The percent changes in the CEL and T2L volumes from pre- to post-RT were different between three treatment cohorts (Kruskal-Wallis, $p<0.002$, $p<0.004$). In particular, patients in the TMZ+bev cohort had a significant and more extreme percentage decrease in the CEL volume from pre- to post-RT (median -79%) than patients in the TMZ cohort (median -30%; rank-sum, $p<0.004$) and patients in the TMZ+enza cohort (median -39%; rank-sum, $p<0.001$). Patients in the TMZ+bev cohort had a marked decrease in T2L from pre- to post-RT (median -56%), which was significantly different from patients in the TMZ cohort (median -20%; rank-sum, $p < 0.003$) and patients in the TMZ+enza cohort who demonstrated an increased median change (median 25%; rank-sum, $p < 0.004$). It can also be seen in Figure 3-2A that for the TMZ+bev cohort, the largest change in CEL took place from pre- to mid-RT while the largest change in T2L was from mid- to post-RT. Patients in the TMZ cohort did not receive imaging examinations at the mid-RT time point. Figure 3-3 illustrated the patterns of changes in volumes of CEL and T2L based upon images from three representative patients.

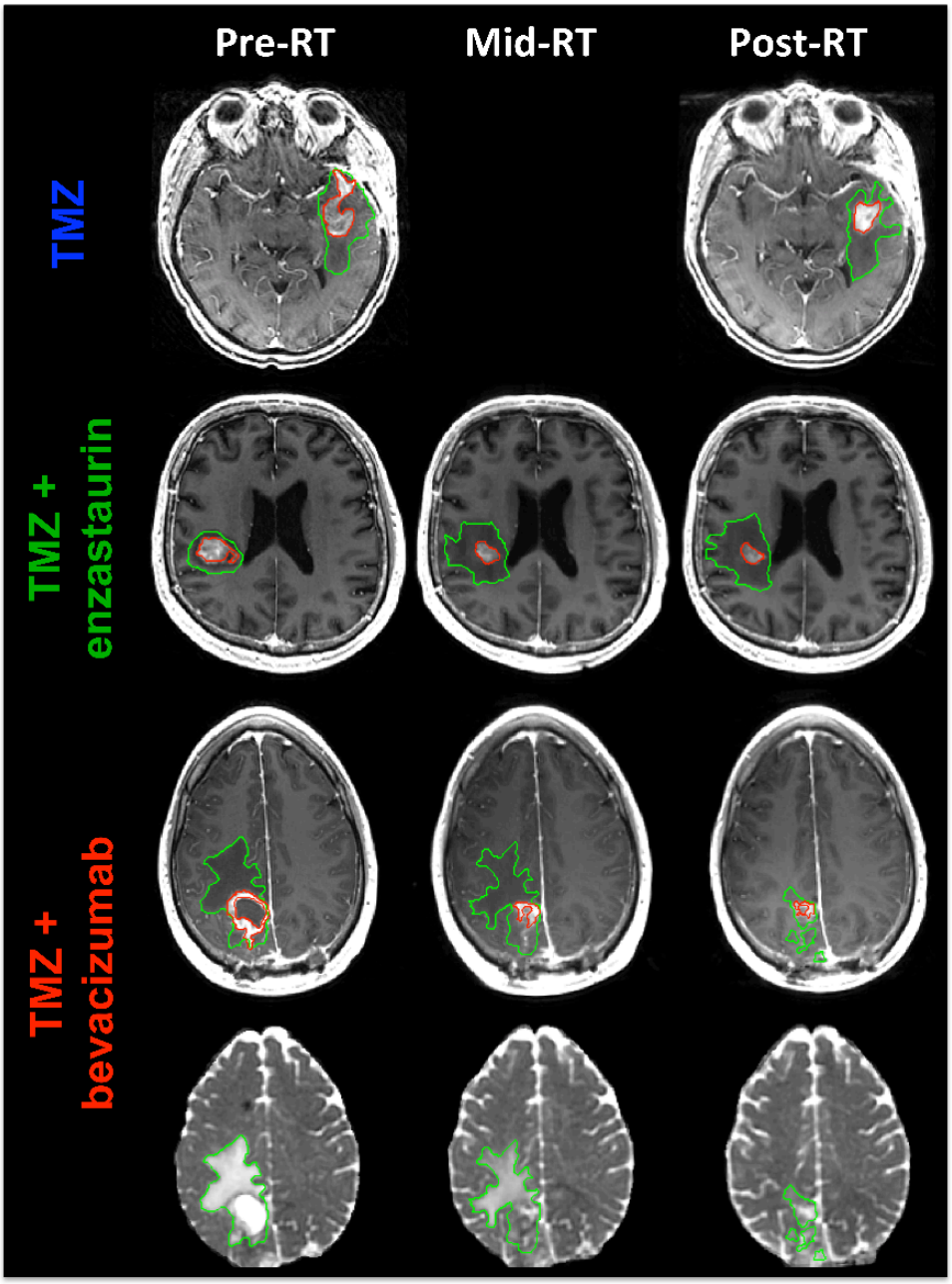

Figure 3-2 Representative T1-weighted post-Gd images at pre-, mid-, and post-RT with contrast-enhancing lesion (CEL, red) and T2-hyperintensity lesion (T2L, green) overlay. ADC images were shown for the patient in the TMZ+bev cohort. Compared to the patients in the TMZ and TMZ+enza cohorts, there was a dramatic decrease in both CEL and T2L from pre- to post-RT for the patients in the TMZ+bev cohort. While the largest change in CEL happened from pre- to mid-RT, which was only 2 weeks into bevacizumab, the largest change in T2L happened from mid-RT to post-RT.

Changes in ADC parameters from pre- to post-RT were also found to be significantly different between the three treatment cohorts within both the CEL (Kruskal-Wallis, $p<0.0002$) and the T2L (Kruskal-Wallis, $p<0.05$) (Figure 3-3Figure 3-2A). The TMZ and TMZ+enza cohorts demonstrated a ~30% increase in median ADC from pre- to post-RT, while the TMZ+bev cohort demonstrated a 2% decrease in median ADC (rank-sum, $p<0.0001$; $p<0.0001$, respectively). Similar patterns were found for median ADC within the T2L (TMZ: 5% increase; TMZ+enza: 13% increase; TMZ+bev: 5% decrease).

Figure 3-3B shows barplots of the mean and standard error of anatomical volumes and median ADC at pre-, mid- and post-RT, with significance levels highlighted. At pre-RT, the CEL was larger in the TMZ+enza cohort but no other parameters showed significantly differences amongst the three cohorts. At post-RT, the TMZ+bev cohort demonstrated significantly smaller T2L and CEL volumes, as well as lower median ADC compared to the other two treatment cohorts.

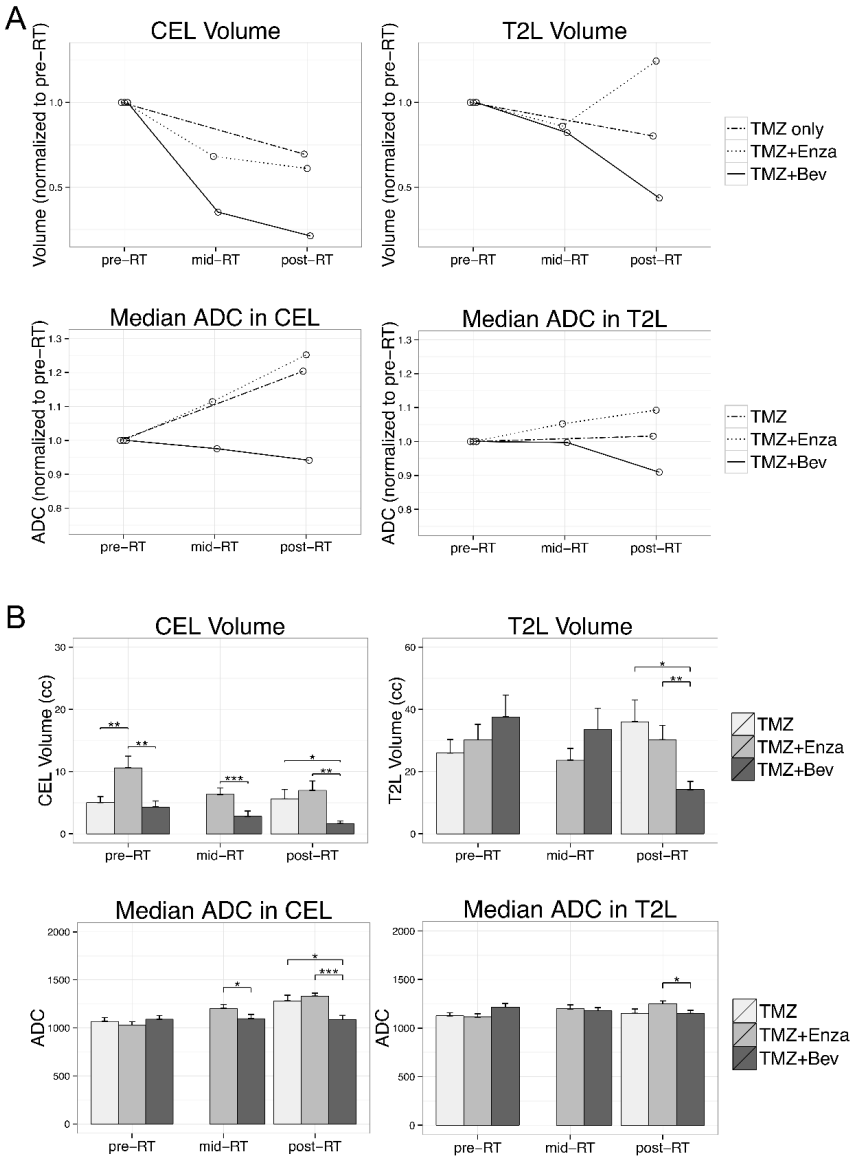

Figure 3-3 (A) Median contrast enhancing lesion (CEL) volume, T2-hyperintensity lesion (T2L) volume and median ADC within the CEL and T2L during the course of RT in the three cohorts. Parameters were normalized to values at pre-RT within each patient. In the TMZ+bev cohort, a marked decrease was observed in both CEL and T2L volumes during the course of RT (A. upper row). While ADC increased from pre- to post-RT in the TMZ and TMZ+enza cohorts, it decreased in the TMZ+bev cohort (A. lower row). (B) barplots of the mean and standard error of lesion volumes and median ADC at pre-, mid- and post-RT for the three treatment cohorts. Parameters that were significantly different between cohorts at each time point were labeled with asterisk. In the TMZ+bev cohort lesion volumes and ADC were significantly different from those in the TMZ and TMZ+enza cohorts. (* p<.05, ** p<.005, *** p<.0005)

3.3.3 Association of Imaging Parameters with Outcome

Table 3-1 summarizes the Cox proportional hazard (CoxPH) analysis of associations between baseline clinical factors (age, gender, KPS, extent of surgery) and patient outcomes, as well as CoxPH analysis of associations with imaging parameters at pre-, mid-, and post-RT with adjustment for clinical factors. Within clinical factors, more extensive surgery was a protective factor for both PFS and OS in the TMZ+bev cohort only (CoxPH, p=0.006 and p=0.008, respectively). Too few KPS values were available to perform an analysis of this parameter in the TMZ cohort.

Univariate CoxPH analysis was first performed to assess associations between imaging parameters and outcomes within each individual study. At pre-RT (post-surgery and before treatment), lesion volumes were not found to be associated with survival. Lower 10%ADC within the T2L was found to be a risk factor for PFS in the TMZ cohort (CoxPH, p=0.02) and in the TMZ+bev cohort (CoxPH, p=0.02). At mid-RT, larger T2L volume was a risk factor in the TMZ+enza cohort (CoxPH, p=0.03 for OS). Lower 10%ADC remained as a risk factor in the TMZ+bev cohort (CoxPH, p=0.007 for PFS). Data were not available in the TMZ cohort for this time point. At post-RT, larger CEL and T2L volumes were risk factors for PFS in the TMZ cohort and for OS in the TMZ+enza cohorts, but not in the TMZ+bev cohort. Lower 10%ADC within the T2L was a risk factor only in the TMZ+bev cohort. Specifically, larger CEL and T2L were associated with shorter PFS for the TMZ cohort (CoxPH, p=0.0001, p=0.004). Larger CEL was associated with shorter PFS (p=0.03) and OS (p=0.01) and larger T2L was associated with shorter OS (p=0.02) in the TMZ+enza cohort. In the TMZ+bev cohort, 10%ADC within the T2L was associated with both PFS (p=0.01) and OS (p=0.0004). The percent change of lesion volumes and ADC from pre- to post-RT were not found to be associated with survival.

Multivariate Cox regression further confirmed that the predictive effects of CEL or ADC were significantly different or trending towards being different between the TMZ+bev cohort and the other cohorts, as the interaction between treatments and CEL or ADC were significant predictors of OS, and of PFS between TMZ+bev and TMZ+enza cohorts (Table 3-2).

Table 3-2 Multivariate Cox Hazard models with covariates for treatment cohort (0=TMZ, 1=TMZ+enza, 2=TMZ+bev), imaging variable (at post-RT), and the interaction between treatment cohort and imaging variable with adjustment for the baseline clinical factors (age, gender, KPS, extent of surgery).

SurvType		TMZ vs TMZ+enza		TMZ vs TMZ+bev		TMZ+enza vs TMZ+bev	
		p-value	HR [95%CI]	p-value	HR [95%CI]	p-value	HR [95%CI]
OS	**Vol_CEL**	0.79	1.01 [0.93 1.10]	***0.054*** **.**	1.153 [0.998 1.33]	***0.067*** **.**	1.29 [0.98 1.69]
	10%ADC_T2L	0.2	1.6 [0.8 3.2]	***0.07*** **.**	0.7 [0.4 1.04]	***0.0009*** **	0.17 [0.06 0.48]
		TMZ vs TMZ+enza		**TMZ vs TMZ+bev**		**TMZ+enza vs TMZ+bev**	
		p-value	HR [95%CI]	p-value	HR [95%CI]	p-value	HR [95%CI]
PFS	**Vol_CEL**	0.36	0.97 [0.9 1.03]	0.16	1.09 [0.96 1.24]	***0.025*** *	1.3 [1.04 1.7]
	10%ADC_T2L	0.15	1.6 [0.8 2.9]	0.42	0.8 [0.6 1.2]	***0.0004*** **	0.27 [0.13 0.55]

. p<0.1
* p<0.05
** p<0.005
***p<0.0005

Figure 3-4 demonstrate the relationship between dichotomized imaging parameters and survival without adjusting for clinical factors by plotting Kaplan-Meier curves for each cohort. Figure 3-4A shows Kaplan-Meier curves for PFS and OS dichotomized by the median CEL volume (Vol_{CEL}) within each treatment cohort at post-RT. For the TMZ cohort, patients with Vol_{CEL}<median had a longer PFS that trended towards significance (A. log-rank, p=0.06). In the TMZ+enza cohort, patients with Vol_{CEL}<median had both longer PFS and OS (B, E. log-rank, p=0.002 for PFS, p=0.02 for OS). In the TMZ+bev cohort, patients with Vol_{CEL}<median had no survival benefit (C, F. log-rank, p>0.1). Figure 3-4B shows Kaplan-Meier curves dichotomized by the 10%ADC within each treatment cohort at post-RT. Patients in the TMZ+bev cohort with 10%ADC>median had significantly longer OS (log-rank p=0.02) and had longer PFS that trended toward significance (log-rank p=0.08). No survival benefits were found for patients with 10%ADC>median in the TMZ or TMZ+enza cohorts.

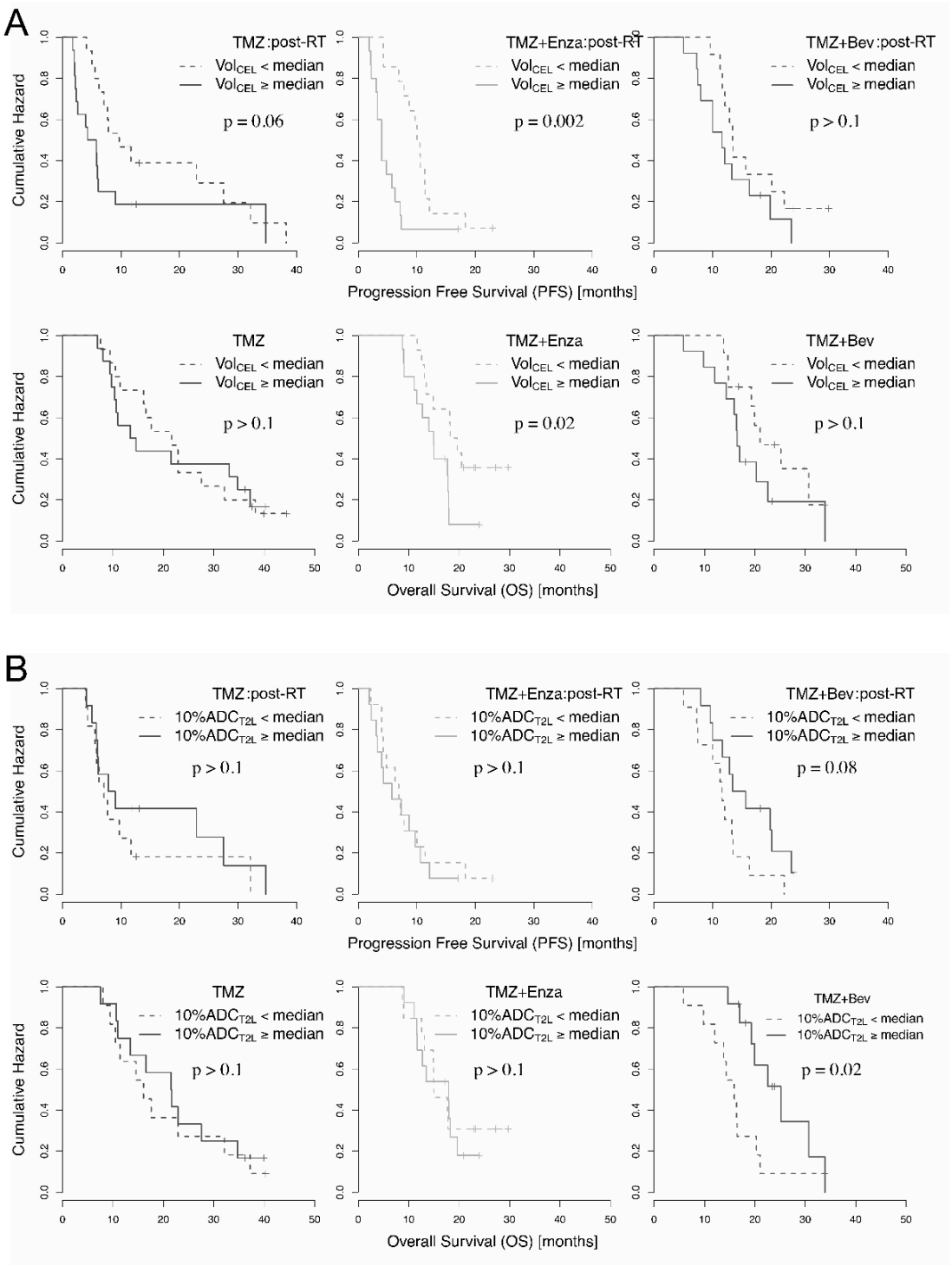

Figure 3-4 (A) Kaplan-Meier curves for progression free survival (PFS) and overall survival (OS) dichotomized by median CEL volume within each treatment cohort at post-RT. (B) Kaplan-Meier curves for progression free survival (PFS) and overall survival (OS) dichotomized by 10%ADC within the T2L at post-RT.

3.4 Discussion

Combined therapy that includes bevacizumab as the first line treatment for patients with newly diagnosed GBM was associated with improved progression-free survival but not with overall survival compared to patients in the TMZ and TMZ+enza cohorts. This is consistent with the overall results from patients in the clinical trial of radiation, temozolomide, erlotinib and bevicizumab that our cohort was selected from [7], as well as reports from multi-institutional phase III trials of patients who were receiving bevacizumab [8-9]. Factors that might contribute to the prolonged PFS are the lower incidences of pseudoprogression and increased incidence of pseudoresponse. Pseudoprogression is expressed as a transient increase in tumor enhancement that is caused by changes in permeability of the blood-brain barrier but does not imply an increase in the spatial extent of the tumor. Because bevaciuzmab can control leakage from the vasculature, it is expressed by a reduction in the volume of the CEL that may or may not be accompanied by a reduction in bulk tumor [9]. The latter is commonly referred to as "pseudoresponse" [26-11] and could compromise the use of anatomic lesion volumes as a biomarker for treatment efficacy. In this paper, we evaluated the lesion volumes and ADC parameters before and after the treatments were given, and analyzed their association with survival within each treatment cohort.

It is clear that patterns of changes in lesion volumes are different when anti-angiogenic therapy is added to standard TMZ and RT (Figure 3-2). Patients treated with bevacizumab demonstrated a marked decrease in CEL volume (median: -79%) from pre- to post-RT, while patients in the TMZ and TMZ+enza cohorts showed only a slight decrease in CEL volume. The reduction in the CEL and T2L volumes with bevacizumab is attributed to its strong anti-VEGF effect, which controls vessel permeability and reduces vasogenic edema. It is interesting to see that the timeline of changes in CEL and T2L were different, as the larger reduction in CEL occurred from pre- to mid-RT, while the larger reduction in T2L was from mid- to post-RT. Enzastaurin does not directly affect vascular permeability and its effect on CEL was less obvious.

The associations of imaging parameters with outcome also varied with treatment. Although lesion volume has been regarded as a variable that defines response, its predictive value was compromised when bevacizumab was added to the treatment. Consistent with previous reports [18-19], our analysis showed that smaller post-RT lesion volumes in the TMZ and TMZ+enza cohorts were associated with longer survival. These were not found to be associated with survival for the TMZ+bev cohort when clinical factors (age, KPS, extent of surgery) were taken into account. We would like to note that over half of the patients who received bevacizumab had a CEL volume at the post-RT exam that was less than 1cc and a third of the patients had non-enhancing progressive disease. This suggests that the CEL is not a good measure of residual/reactive tumor for patients treated with bevacizumab and provides motivation for identifying alternative parameters within the T2L that can more accurately predict treatment outcomes.

Parameters that have recently been suggested as early biomarkers for predicting subsequent progression following treatment with anti-angiogenic agents are derived from histogram analysis of the ADC and the manner in which these parameters change before and during treatment [18,17,19]. When examining the time course of changes in ADC, it was not surprising that bevacizumab-treated patients demonstrated a distinct pattern (Figure 3-2). While the median ADC increased (30%) from pre- to post-RT in TMZ and TMZ+enza cohorts, it decreased in both CEL (3%) and T2L (5%) for the TMZ+bev cohort. The increase of ADC shortly after TMZ plus RT has been reported previously [28-29] and was associated with the disruption of tissue architecture and decreased cellularity caused by treatment–induced necrosis and/or apoptosis. With bevacizumab, ADC metrics decreased due to a reduction in vasogenic edema.

Although ADC metrics were reduced from pre- to post-RT in almost all patients in the TMZ+bev cohort, our results showed that patients with lower 10% ADC at post-RT also had shorter survival (Figure 3-4B). This association was further confirmed in the Cox survival

analysis when adjusted for clinical factors (Table 3-1). ADC was not found to be associated with survival for the TMZ or TMZ+enza cohorts. Tumor and vasogenic edema are two factors that are commonly present but have opposing effects within the tumor microenvironment [32-31]. Vasogenic edema often accompanies effective RT, but can also be symptomatic of tumor [32]. This compromises the potential of using ADC as a measurement of tumor cellularity, as vasogenic edema may mask the existence of recurrent tumor, and may explain why ADC was not associated with survival for TMZ and TMZ+enza cohorts when adjusted for clinical factors. In tumors being actively treated with bevacizumab, the vasogenic edema is more effectively controlled [30], resulting in lower ADC values, which may more closely reflect the cellularity of the tumor. Our results support this hypothesis by indicating that lower ADC percentiles within the T2L were significant risk factors for both PFS and OS for the TMZ+bev cohort when adjusted for clinical factors. The multivariate Cox analysis that took into account the interaction of ADC and treatment indicated that it was only predictive of outcome for the TMZ+bev cohort.

While the 10% ADC in the T2L at the post-RT exam can be a metric for evaluation of residual tumor in treatment that includes bevacizumab, caution should be taken in interpreting low ADC values within the lesion at both earlier and later time windows. Low ADC within the T2L that is observed immediately after surgery may be due to ischemia, which typically returns to normal within 90 days [31]. These abnormalities are replaced by contrast enhancement on follow-up imaging and can be identified on the immediate postoperative diffusion-weighted scan. Another issue that can confound the interpretation of low ADC is gelationous necrosis. This can occur in patients who are treated with bevacizumab but not until several months after RT [35-36]. Patients who demonstrate this type of necrosis were shown to have longer survival [35].

Other studies in the literature have reported that fDM and other ADC metrics that reflect pixel by pixel changes in ADC in the overlapping contrast enhancing volumes between baseline and mid-RT examinations are predictive of outcome in patients with newly diagnosed GBM

[38,39]. In Chapter 2, where we performed a detailed analysis of the fDM and single time point ADC metrics in the TMZ+bev cohort, we found that the median and 10^{th} percentile values in the T2Lwere the only ADC metrics associated with survival. The reason why the fDM and related parameters are unable to predict outcome for this patient population is likely to be due to the relatively limited volumes of the contrast enhancing volumes that were observed in comparison to other studies. This reflects both the relatively aggressive resections performed at our institution, which result in relatively low residual enhancing tumor volumes, and the anti-angiogenic effects of the treatments considered, which cause a further reduction in enhancing volumes at the 1 month time point. Future studies of ADC metrics should consider alternative strategies for defining regions of interest that take into account regions of non-enhancing tumor.

3.5 Conclusion

This study evaluated 96 patients with newly diagnosed GBM who were on three different treatment regimens and found that there were differences in the evolution of imaging parameters between cohorts. These showed that there was no overall survival benefit found when enzastraurin or bevacizumab was added to standard temozolomide treatment plus RT. The most distinct pattern of changes in lesion volumes and ADC parameters occurred in the treatment arm that included bevacizumab. There was a rapid decline of ADC percentile values immediately following onset of TMZ+bev in almost all subjects, with lower ADC percentile values observed for the patients who progressed early. We hypothesize that this is due to the anti-VEGF effect of bevacizumab, which reduced the extent of vasogenic edema at this time point and therefore allowed the observed ADC values to more accurately reflect the presence of residual tumor burden. We suggest that tracking the changes in ADC could potentially assist radiologists in monitoring response to therapy that includes bevacizumab. Of interest is that lesion volumes, which were biomarkers in cohorts treated with TMZ and TMZ+enza, were not associated with

survival for patients in the TMZ+bev cohort. This suggests that oncologists should consider the treatment regimen being used when interpreting variations in these imaging parameters.

3.6 References

1 Stupp R, Mason WP, van den Bent MJ, et al. Radiotherapy plus concomitant and adjuvant temozolomide for glioblastoma. N Engl J Med. 2005;352:987–996.

2 Teicher BA, Alvarez E, Menon K, et al. Antiangiogenic effects of a protein kinase Cbeta-selective small molecule. Cancer Chemother Pharmacol. 2002;49:69–77.

3 Tabatabai G, Frank B, Wick A, et al. Synergistic antiglioma activity of radiotherapy and enzastaurin. Ann Neurol. 2007;61:153–161.

4 Senger DR, Galli SJ, Dvorak AM, et al. Tumor cells secrete a vascular permeability factor that promotes accumulation of ascites fluid. Science 219: 983–985, 1983.

5 Friedman HS, Prados MD, Wen PY, et al. Bevacizumab alone and in combination with irinotecan in recurrent glioblastoma. J Clin Oncol. 2009;27:4733–4740.

6 Jain RK, Tong RT, Munn LL. Effect of vascular normalization by antiangiogenic therapy on interstitial hypertension, peritumor edema, and lymphatic metastasis: insights from a mathematical model. Cancer Res. 2007;67:2729–2735.

7 Clarke JL, Molinaro AM, Phillips JJ, et al. A single-institution phase II trial of radiation, temozolomide, erlotinib, and bevacizumab for initial treatment of glioblastoma. Neuro Oncol. 2014 Jul;16(7):984-90.

8 Mark R. Gilbert, James J. Dignam, Terri S. Armstrong, et al. A Randomized Trial of Bevacizumab for Newly Diagnosed Glioblastoma. N Engl J Med 2014; 370:699-708.

9 Olivier L. Chinot, Wolfgang Wick, Warren Mason, et al. Bevacizumab plus Radiotherapy–Temozolomide for Newly Diagnosed Glioblastoma. N Engl J Med 2014; 370:709-722.

10 Pope WB, Lai A, Nghiemphu P, Mischel P, Cloughesy TF. MRI in patients with high-grade gliomas treated with bevacizumab and chemotherapy. Neurology 2006;66:1258-60.

11 de Groot JF, Fuller G, Kumar AJ, et al. Tumor invasion after treatment of glioblastoma with bevacizumab: radiographic and pathologic correlation in humans and mice. Neuro Oncol. 2010 Mar;12(3):233-42.

12 Wen PY, Macdonald DR, Reardon DA, et al. Updated response assessment criteria for high-grade gliomas: response assessment in neuro-oncology working group. J Clin Oncol 2010;28:1963-72.

13 Pope WB, Qiao XJ, Kim HJ, Lai A, et al. Apparent diffusion coefficient histogram analysis stratifies progression-free and overall survival in patients with recurrent GBM treated with bevacizumab: a multi-center study. J Neurooncol. 2012;108:491-8.

14 Moffat BA, Chenevert TL, Lawrence TS, et al. Functional diffusion map: a noninvasive MRI biomarker for early stratification of clinical brain tumor response. Proc Natl Acad Sci USA 2005;102:5524-5529.

15 Hamstra DA, Galbán CJ, Meyer CR, et al. Functional diffusion map as an early imaging biomarker for high-grade glioma: correlation with conventional radiologic response and overall survival. J Clin Oncol 2008;26:3387-3394.

16 Ellingson BM, Malkin MG, Rand SD, et al. Volumetric analysis of functional diffusion maps is a predictive imaging biomarker for cytotoxic and anti-angiogenic treatments in malignant gliomas. J Neurooncol. 2011;102:95-103.

17 Ellingson BM, Sahebjam S, Kim HJ, et al. Pretreatment ADC histogram analysis is a predictive imaging biomarker for bevacizumab treatment but not chemotherapy in recurrent glioblastoma. AJNR Am J Neuroradiol. 2014 Apr;35(4):673-9.

18 Li Y, Lupo JM, Polley MY, Crane JC, Bian W, et al. Serial analysis of imaging parameters in patients with newly diagnosed glioblastoma multiforme. Neuro Oncol. 2011;13:546-57.

19 Khayal IS, Polley MY, Jalbert L, et al. Evaluation of diffusion parameters as early biomarkers of disease progression in glioblastoma multiforme. Neuro Oncol. 2010 Sep;12(9):908-16.

20 Paldino MJ, Desjardins A, Friedman HS, Vredenburgh JJ, et al. A change in the apparent diffusion coefficient after treatment with bevacizumab is associated with decreased survival in patients with recurrent glioblastoma multiforme. Br J Radiol. 2012 Apr;85(1012):382-9.

21 Wen Q, Jalilian L, Lupo JM, et al. Comparison of ADC metrics and their association with outcome for patients with newly diagnosed glioblastoma being treated with radiation therapy, temozolomide, erlotinib and bevacizumab. J Neurooncol. 2014 Oct 29.

22 Macdonald DR, Cascino TL, Schold SC, et al. Response criteria for phase II studies of supratentorial malignant glioma. J Clin Oncol. 1990;8:1277–1280.

23 Nelson SJ, Nalbandian AB, Proctor E, Vigneron DB. Registration of images from sequential MR studies of the brain. J Magn Reson Imaging. 1994;4:877–883.

24 Saraswathy S, Crawford F, Nelson SJ. Semi-automated segmentation of brain tumor lesions in MR images. In: 14th Annual Meeting of ISMRM; 2006; Abstract 1609.

25 Basser PJ, Pierpaoli C. Microstructural and physiological features of tissues elucidated by quantitative-diffusion-tensor MRI. J Magn Reson B. 1996;111:209–219.

26 Wen PY, Macdonald DR, Reardon DA, et al. Updated response assessment criteria for high-grade gliomas: response assessment in neuro-oncology working group. J Clin Oncol 2010;28:1963-72.

27 Clarke JL, Chang S. Pseudoprogression and pseudoresponse: challenges in brain tumor imaging. Curr Neurol Neurosci Rep 2009; 9:241-46.

28 Provenzale JM, Mukundan S, Barboriak DP. Diffusion-weighted and perfusion MR imaging for brain tumor characterization and assessment of treatment response. Radiology. 2006;239(3):632–649.

29 Chenevert TL, Stegman LD, Taylor JM, et al. Diffusion magnetic resonance imaging: an early surrogate marker for therapeutic efficacy in brain tumors. J Natl Cancer Inst. 2000;92(24):2029–2036.

30 Kono K, Inoue Y, Nakayama K, et al. The role of diffusion-weighted imaging in patients with brain tumors. AJNR Am J Neuroradiol. 2001;22:1081-1088.

31 Guo AC, Cummings TJ, Dash RC, Provenzale JM. Lymphomas and high-grade astrocytomas: comparison of water diffusibility and histologic characteristics. Radiology. 2002;224:177-183.

32 Stummer W. Mechanisms of tumor-related brain edema. Neurosurg Focus. 2007 May 15;22(5):E8.

33 Ananthnarayan S, Bahng J, Roring J, et al. Time course of imaging changes of GBM during extended bevacizumab treatment. J Neurooncol. 2008;88(3):339-47.

34 Smith JS, Cha S, Mayo MC, et al. Serial diffusion-weighted magnetic resonance imaging in cases of glioma: distinguishing tumor recurrence from postresection injury. 2005;103(3):428-38.

35 Mong S, Ellingson BM, Nghiemphu PL, et al. Persistent diffusion-restricted lesions in bevacizumab-treated malignant gliomas are associated with improved survival compared with matched controls. AJNR Am J Neuroradiol. 2012;33(9):1763-70.

36 Gerstner ER, Frosch MP, Batchelor TT. Diffusion magnetic resonance imaging detects pathologically confirmed, nonenhancing tumor progression in a patient with recurrent glioblastoma receiving bevacizumab. J Clin Oncol 2010;28:91–93

37 Gupta A, Young RJ, Karimi S, et al. Isolated diffusion restriction precedes the development of enhancing tumor in a subset of patients with glioblastoma. AJNR Am J Neuroradiol 2011;32:1301–06

38 Moffat BA, Chenevert TL, Lawrence TS, Meyer CR, Johnson TD, Dong Q, Tsien C, Mukherji S, Quint DJ, Gebarski SS, Robertson PL, Junck LR, Rehemtulla A,Ross BD.

Functional diffusion map: a noninvasive MRI biomarker for early stratification of clinical brain tumor response. Proc Natl Acad Sci USA 2005;102:5524-5529.

39 Benjamin M. Ellingson, Timothy F. Cloughesy, Taryar Zaw, Albert Lai, Phioanh L. Nghiemphu, Robert Harris, Shadi Lalezari, Naveed Wagle, Kourosh M. Naeini, Jose Carrillo, Linda M. Liau, and Whitney B. Pope. Functional diffusion maps (fDMs) evaluated before and after radiochemotherapy predict progression-free and overall survival in newly diagnosed glioblastoma. Neuro Oncol. 2012 Mar; 14(3): 333–343.

Chapter 4

Association among MR diffusion, perfusion, spectroscopy, and image-guided histophathology with special attention to treatment effect

This chapter takes the advantage of image-guided tissue samples to directly compare relationships between tissue histopathology and imaging parameters within the contrast enhancing lesion for patients with recurrent GBM and has a special focus on the differentiation of treatment effect and tumor.

4.1 Introduction

Standard therapy for glioblastoma (GBM) involves maximal safe tumor resection followed by radiotherapy with concurrent and adjuvant temozolomide [1]. Currently, changes contrast enhancement on anatomic MRI and clinical evaluation are key determinants of response to therapy and evaluation of tumor recurrence. Despite their widespread use, it is well known that changes in contrast enhancement after treatment are not specific for tumor. Chemoradiation therapy can cause early or late effects on contrast enhancement, which can manifest during the immediate post-radiation period or for months to years after treatment. It's been reported that 20% to 30% of patients show increased contrast enhancement on their first post-radiation MRI that eventually subsides without any change in therapy [2-4]. This phenomenon, termed pseudoprogression, likely results from transiently increased permeability of the tumor vasculature from chemoradiation, and complicates the determination of tumor progression. Some of these changes might represent radiation necrosis, as defined by histopathology. These treatment related effects have implications for patient management, because while true tumor progression indicates treatment failure and necessitates a change in therapy, a positive effect of the therapy may indicate that it is being successful. Mistaking treatment effects with tumor progression may

therefore result in premature discontinuation of effective adjuvant therapy or unnecessary surgery. Providing a more reliable strategy for distinguishing between treatment effects and tumor progression is vital for making informed decisions about patient care.

There has been much effort to differentiate true progression from treatment effect by using advanced MR imaging techniques such as diffusion weighted imaging (DWI), perfusion imaging, and proton spectroscopic imaging (^{1}H MRSI). As recurrent high-grade glioma is associated with a combination of hypercellularity, hypervascularity, hypermetabolism, and rapid growth, it has been widely speculated that true tumor recurrence should demonstrate lower ADC, higher cerebral blood volume (CBV) and higher Choline (Cho) to N-acetyl aspartate (NAA) ratio than pure treatment related effect. Although some success has been reported, published results have been quite mixed. First investigation on DWI showed lower ADC values in the recurrent tumor group compared to those in the treatment induced necrosis [5]. This result was mirrored by another group but there was a bigger variation in ADC values for the radiation necrosis than the recurrent tumor group [6]. Cases of radiation necrosis with low ADC values have also been reported [7]. For MRS, the Choline (Cho)/Creatine (Cr) ratios, Cho/NAA ratios, and NAA/Cr ratios that are obtained may differ between tumor recurrence and radiation necrosis [8-10], but it has been reported that there is a large overlap between the two groups [11-14]. Results obtained with MR perfusion have been relatively more consistent, with an excellent correlation between elevated rCBV values and the presence of recurrent tumor having been reported in a recent image-guided prospective study [15]. While these general findings have been corroborated by other studies [16-20], the sensitivity and specificity have been highly varied, and values of rCBV that are recommended to be used as threshold for distinguishing between the two conditions have been 0.71 [15], 1.49 [20] and 1.75 [16]. A recent study that discussed patterns of elevated rCBV and low ADC indicate that they are frequently observed in coagulation necrosis [21].

Some of the mixed results that have been observed may be due to the small sample sizes considered (usually a total of 10-30 patients), to recruiting patients with mixed glioma grades as well as metastases, and to lacking histopathological confirmation of radiation necrosis cases. In addition, most studies use ROI based analysis of values in the lesion, which suffers from limitations due to the complexity of the tissue microenvironment. High-grade gliomas are intrinsically heterogeneous and after treatment are likely to include mixed regions of tumor and treatment effects. These factors may lead to difficulties in dichotomizing patients into 'pure' tumor and 'pure' treatment effect, as well as causing there to be large variations in imaging parameters within each sub-group.

In this study, we prospectively recruited patients whose initial diagnosis was GBM and who were presenting for surgical resection due to suspected recurrence and who had agreed to have pre-surgical examination that included perfusion, diffusion and spectroscopy. This enabled us to study both variations in the entire lesion and to relate in vivo imaging parameters to histopathology obtained from image-guided tissue samples. Our goal was to evaluate the performance of advanced MR techniques in differentiating between treatment effect and tumor samples, and to understand the underlying challenges inherent in evaluating these samples based upon measures of hypoxia, microvascular morphology, axonal disruption, cell proliferation and cell density.

4.2 Materials and Methods

4.2.1 Patient Population

A total of 88 patients with an initial diagnosis of GBM, who were presenting for surgical resection due to suspected recurrence were prospectively enrolled into our study from July 2007 to November 2011. All participants had previously received standard-of-care treatments that included surgical resection, external beam radiation therapy (EBRT) and chemotherapy. The

EBRT comprised 180 cGy per day for a total dose of 5940 cGy or 200 cGy per day for a total dose of 6000 cGy over approximately 6 weeks, which is the standard protocol being used at our institution. All patients had received prior temozolomide (Temodar; Schering-Plough, Kenilworth, NJ) and some had received other adjuvant chemotherapies. This study was approved by our Institutional Review Board and informed consent was obtained for each subject for both acquiring the advanced imaging data and for the surgeon taking additional, image guided tissue samples from regions that were from would have been removed as part of the standard clinical resection.

4.2.2 Pre-operative MRI/MRS and Data Processing

Pre-operative MR imaging exams were performed on a 3T or 1.5T GE scanners. Similar MRI protocol was utilized: Anatomic imaging included sagittal T1-weighted spin echo, axial 3D T2-weighted fast spin echo (FSE), axial fluid attenuated inversion recovery (FLAIR), contrast-enhanced 3D spoiled gradient-recalled acquisition in the steady state (SPGR) T1-weighted and T1-weighted post-contrast spin echo images. Physiologic imaging included 3 or 6-directional DWI (echo-planar; repetition time (TR)/echo time (TE) = 10s/99ms, NEX=4, voxel size=1.7x1.7x3mm3, b=1000s/mm2), Gradient-echo echo-planar dynamic susceptibility contrast-enhanced (DSC) perfusion imaging acquired immediately before, during, and after an injection of 0.1 mmol/kg gadolinium diethyltriamine pentaacetic acid (Gd-DTPA) at 5ml/s (TR/TE/Flip-angle = 1250-1500/35-54 ms/35º or 60º; voxel size=1.9x1.9x3-4mm3, 60-80 timepoints). Spectroscopy was acquired in a subset of the patients using Lactate-edited 3D MR H-1 MRSI with point resolved spectroscopic selection (PRESS) for volume localization and very selective saturation (VSS) pulses for lipid signal suppression (TR/TE = 1104/144 ms, field of view = 16×16×16 cm^3, nominal voxel size = 1×1×1 cm^3, flyback echo-planar readout gradient in the SI direction).

The imaging data were then transferred to a commercially available Linux workstation and were processed to guide prospective selection of tissue sampling sites. All anatomical images were co-registered to the corresponding post-Gd 3D SPGR images [22]. The accuracy of co-registration was visually verified. In-house software was applied to derive estimates of in vivo DWI, DSC and MRSI parameters. Maps of the ADC and fractional anisotropy (FA) were generated on a pixel-by-pixel basis. DSC datasets were nonrigidly aligned using the VTK CISG software package [23]. Cerebral blood volume (CBV), percent ΔR2* signal recovery (Recov), ΔR2* peak heights (PH) were calculated for each voxel. CBV intensities were obtained by fitting the dynamic perfusion data by a modified gamma-variate function with a recirculation parameter [24]. Peak height and percent recovery values were estimated using a simple nonparametric procedure [25]. MRSI data were processed to quantify total choline (Cho), creatine (Cre), N-acetyl-aspartate (NAA), lipid (Lip), and lactate (Lac) levels, from which maps of the choline-to-N-acetyl-aspartate index (CNI) could be derived. CNI values were generated from a linear-regression-based algorithm and represent the deviation of choline and NAA levels relative to normal voxels [26].

4.2.3 Intraoperative Tumor Tissue Site Selection

Tissue sampling sites within the contrast enhancement was prospectively selected based on the processed preoperative MR images. Regions demonstrating either abnormally decreased ADC, increased CBV and/or elevated CNI values that were suspicious for viable tumor, were evaluated for the purpose of planning which tissue to samples to obtain during surgery. One to four tumor tissue samples from each patient were designated with 5-mm diameter spherical targets on co-registered MR images using surgical navigation software (BrainLAB Inc.). To minimize risks to the patient, no control tissue (normal brain) was acquired. Image-guided navigation was applied to locate tissue corresponding to planned targets and to acquire safely accessible samples. The surgeon did their best to obtain tissue from the proposed targets, but in

some cases this was not possible. An estimate of the actual location where the tissue sample came from was obtained by taking a screenshot of that location, which provided a record of the LPS coordinates to be made. Upon excision, tissue samples were immediately fixed in 10%zinc formalin, dehydrated by graded ethanols, and embedded in Paraplast Plus wax (McCormick Scientific) using standardized techniques for tissue processing and immunohistochemistry. Additional non-image guided samples were obtained for clinical diagnosis as per standard practice.

4.2.4 Quantification of MR Parameters for the Image Guided Tissue Samples

Tissue sample ROIs corresponding to 5mm diameter spheres that were centered at the location where actual sample was obtained were generated on the pre-surgical images. ROIs that corresponded to normal appearing brain (NAB), the lesion on the T2-weighted images (T2L) and the contrast-enhancing lesion (CEL) on post-Gadolinium T1-weighted images were also defined for comparative purposes. Median ADC and FA values were quantified for each ROIs. For DSC, a weighted-average model-curve was generated at each image guided sample location by determining the percentage of the tissue sample mask within each perfusion voxel and automatically excluding unquantifiable voxels of noise [25] before taking a weighted average of the remaining dynamic curves based on the percentage overlap with the mask. This process created one curve per tissue sample to quantify that resulted in an increase in SNR of the dynamic data which in turn improved the accuracy or goodness of fit of model fitting for cerebral blood volume (CBV) calculation. MR parameters were normalized by dividing estimated values in NAB for further analysis (rADC, rFA, rCBV, rPH, rCHO, rNAA, rLIP, rLAC).

4.2.5 Histopathologic Analysis

Sections from the tissue specimens were stained with hematoxylin and eosin (H&E) or immunostained using an automated immunohistochemical (IHC) tissue staining process (Ventana

Medical Systems Benchmark XT). Digital images were captured with an Olympus BX41TF microscope and an Olympus DP70 digital microscope camera. All samples were reviewed and scored by a board-certified pathologist blinded to the imaging and clinical status of the patients. All of the tissue specimens were of sufficient size and IHC staining quality to be included for analysis.

4.2.5.1 Determining Treatment Effect and Tumor Tissue Samples

For each tissue sample, the presence of tumor cells was scored based upon review of H&E-stained sections. A tumor cellularity score ranging from 0~3 was given based on the contribution of tumor cellularity to total cellularity: 0 = no tumor/neoplastic feature present. 1 = infiltrating tumor margin, 2 = infiltrating cellular tumor and 3 = highly cellular tumor involving >75% of the tissue. Tumor cells were identified based upon morphologic features, including cytologic atypia, enlarged nuclear to cytoplasmic volume ratio, and hyperchromasia. Samples with tumor score of 0 were further confirmed by pathologist as corresponding to true treatment effect if it contains one of the treatment related features including hyalinized blood vessels, reactive gliosis et al. Samples with 0 tumor score but that demonstrate no treatment effect features were excluded from the analysis (about 1%). With this definition for the purposes of our analysis the samples with "tumor score = 0" can be considered as corresponding to "treatment effect".

4.2.5.2 Other Histopathologic Analysis

The cumulative extent of necrosis was scored from H&E stain as 0 = no necrosis, 1 = focal necrosis involving <50% of the tissue area, and 2 = extensive necrosis involving ≥ 50% of the tissue area, and 2 = extensive necrosis involving ≥ 75% of the tissue area.

The degree of microvascular hyperplasia (MVH) was measured using immunohistochemistry (IHC) stained sections for factor VIII. The microvascular morphology was graded as delicate

(delicate MV) (resembling normal cerebral vessels), simple microvascular hyperplasia (simple MVH) (circumferential single cell hyperplasia with definitive lumen), or complex microvascular hyperplasia (complex MVH) (circumferential multi-layered and glomeruloid-type vessels). The relative contribution of each vascular morphology to total vascularity within the sample was qualitatively measured on a four-tiered ordinal scale (0 = no contribution, 1 = minimal, 2 = prevalent, 3 = predominant). The contribution of each type of microvascular element to the overall vascularity was scored as: 0 = delicate only, 1 = simple MVH identified, and 2 = complex MVH identified.

The degree of hypoxia was assessed by the percentage cells that were positive based on immunohistochemical (IHC) analysis with CA-9 and was scored as 0 = no positive staining, 1 ≤ 10%, 2 = 10%~25%, 3 ≥ 25%. The degree of architectural disruption was measured based on IHC analysis with SMI-31 staining, which is an antibody against a phosphorylated neurofilament epitope in thick and thin axons. This was scored as: 0 = no disruption of the normal architectural, 1 = minimal disruption, 2 = mild disruption, 3 = severe disruption with no residual SMI-31 immunostaining.

Proliferation and average cell numbers were quantified based on number of Ki-67 stained cells and total cells over 3-5 separate fields. Proliferation was calculated as a labeling index [MIB-1-positive nuclei per total tumor cells counted per 200× field) × 100%] based on the evaluation of 3-5 fields and more than 1000 cells. Note that average cell numbers not only count tumor cells but can include microglia, reactive gliosis, lymphocytes et al as well.

In selected cases, further IHC analysis was performed using CD45 and CD68 staining. CD45 is a leukocyte common antigen, which is able to confirm the presence of T and B lymphocytes, produced by acquired or adaptive immunity. CD68 is a 110 kDa transmembrane glycoprotein, expressed by monocyte/macrophage lineages and serves as a marker for macrophages and

microglia, produced by innate immunity. The score was defined as: 0 = none to <5% of tissue contains positive cell, 1 = <25%, 2 = 25%~50%, 3 = ≥50%.

4.2.6 Statistical Analysis

As tumor score defined treatment effect and tumor samples, it was the main parameter considered in the analysis. Three aspects were considered: (1) assessment of association between histopathologic features and tumor score. (2) assessment of association between MR parameters and tumor score with univariate and multivariate regression. (3) assessment of association between vivo MR parameters and histopathological features.

4.2.7 Association of Histopathological or MR Parameters and Tumor Score

This analysis focused on whether any of the features were associated with tumor score. As our observation (tumor score) is ordinal, a marginal models for correlated ordinal multinomial responses，adjusted for repeated measures, was applied to evaluate the probability of observing ordinal outcomes.

This model is written as:

$$logit\left[p\left(Y_{ij} \leq K \mid X_i, Z_i\right)\right] = \alpha_K + X'_{ij}\beta + Z'_{ij}b_i;\ \ i = 1, \cdots, N_{subjects}; K = 1, \cdots, c-1$$

where Y_{ij} is the binary outcome for subject i with biopsy measurement j (ranges from 1 to 4), c is the total levels of the ordinal variable, X_{ij} is the design matrix for the fixed effects, Z_{ij} is the design matrix for the random effects, α_K are rows corresponding to the jth biopsy specimen, and β and b_i are the vectors of fixed and random parameters. The intercepts are fixed and category dependent. The odds ratio, 95% confidence interval (95% CI) and p value for each variable are reported. The ordinal outcome mixed effect models were analyzed using ordLORgee in R.

4.2.7.1 Association of Multiple MR Parameters with Tumor Score

A multivariate mixed effects linear model was applied to evaluate whether including multiple MR parameters would improve their association with tumor score. Missing values were first filled in through imputation. Pearson correlation test was then applied to test correlations of each pair of MR parameters. Uncorrelated MR parameters (correlation coefficient<0.7) and parameters that were likely to be associated with tumor score ($p<0.2$) in the univariate analysis were included. The purpose of this analysis was to see whether combinations of these parameters would improve the association with tumor score compared with the univariate parameters.

4.2.7.2 Association of MRI Parameters with Histopathology Features

The univariate mixed effects linear models described above were used with each histopathology feature as the outcome, and the imaging parameters as a fixed predictor, adjusting for the patient effect. Models of ordinal-valued outcomes (e.g. Necrosis, MVH, et al.) were analyzed with ordLORgee in R, and models involving continuous outcomes (e.g. proliferation, average cells) were analyzed with geeglm, with the family being "Gaussian".

4.2.7.3 Comparison of Clinical Diagnosis with Whole Lesion-Based MR Parameters

In addition to the sample-wise analysis, we also evaluated whether MR parameters from the entire CEL were associated with the patient based clinical diagnosis of treatment effect or tumor recurrence. For each imaging parameter, the percentile values, as well as volumes takes on values cut off by heuristically determined thresholds were quantified (e.g. Vol(rCBV>2) calculates the volume that has rCBV>2). A logistic regression was applied to evaluate the association between each variable and the clinical diagnosis.

A p value of less than 0.05 was considered to be significant for all of the statistical tests. Field strength was adjusted for in the MRI parameters and flip angle was adjusted for in the DSC

parameters. For patients with multiple recurrences, only the first recurrence was included to avoid ambiguity in assigning independent data. Because of the exploratory nature of the study, no adjustment for type I error was included. All analysis was done in R (Version 3.0.3)

4.3 Results

Of the 88 patient enrolled in this study, 17 patients were identified based upon the clinical diagnosis as treatment effect and 71 patients were identified as recurrence GBM. This diagnosis was made on the basis of histologic findings in non-image guided surgical resection that indicated more than 5% of the sample had viable tumor.

For the image-guided analysis, a total of 106 tissue samples were taken from 62 patients. The other 26 subjects were excluded either because the planned samples were not obtained during surgery, the coordinates of their locations were unable to be recorded, they were too small for histopathology analysis, or they were taken from non-enhancing regions of the lesion. Of 106 tissue samples, 33 were characterized as treatment effect with no tumor cells present (tumor score = 0), 14 samples had a tumor score of 1, 21 had a tumor score of 2, and 38 had a tumor score of 3. Of the 33 treatment effect samples, 12 were from patients whose lesion was considered to be treatment effect based upon the clinical diagnosis and 21 were from patients with a confirmed clinical diagnosis recurrent GBM. Table 4-1 summarizes the patient and tissue sample populations.

Table 4-1 Summary of patient and tissue sample population in samples-wise and lesion-wise analysis.

Sample-wise

Patients	*Samples*	*TS=0/TE*	*TS=1*	*TS=2*	*TS=3*
62	106	33	14	21	38

Lesion-wise		
Patients	*Treatment effect*	*Tumor recurrence*
88	17	72

Abbreviations: TS=tumor score; TE: treatment effect

4.3.1 Association between Tumor Score and Other Histopathological Features

Summary statistics are shown in Figure 4-1A. The mixed effect model showed that all histopathological features were significantly associated with tumor score ($p<0.05$) with a odds ratio > 1, except for delicate MV, which indicated that a higher tumor score was associated with more necrosis, more microvascular hyperplasia, more hypoxia, more axonal disruptions, more cell proliferation, higher cell density and less delicate MV. Figure 4-1B shows the histopathological features of a tumor sample and treatment effect sample. Figure 4-2 showed the distribution of all histopathological features in relation to tumor scores with spineplots (for ordinal features) and boxplots (for continuous features). It's worth noting that despite the overall trend and the statistical significance, treatment effect samples (Tumor score=0) demonstrate bigger variation than low tumor samples (Tumor score=1) in features such as complex MVH, hypoxia, axonal disruption, CD45, CD68, cell density.

A more intuitive way for visualizing the histopathological features graded by tumor scores is the clustered colormap as shown in Figure 4-3. The high degree of heterogeneity in the features from the TS=0 group in the enhancing lesion are clearly seen.

A

	Summary Statistics						Mixed Efffect Model			
	Pt #	TS #	TS=0 #	TS=1 #	TS=2 #	TS=3 #	Odds Ratio	95% CI		P Value
Categorical Features										
Necrosis	62	104	33	14	21	36	2.66	1.10	6.42	0.029 *
Total MVH	61	105	32	14	21	38	3.18	1.58	6.42	0.0012 **
Delicate MVH	62	106	33	14	21	38	0.47	0.33	0.67	3e-05 ***
Simple MVH	62	106	33	14	21	38	2.24	1.48	3.38	0.00014 ***
Complex MVH	62	106	33	14	21	38	3.26	1.04	10.27	0.043 *
Hypoxia	62	106	33	14	21	38	2.32	1.63	3.30	2e-16 ***
AD	62	105	33	14	21	37	2.43	1.68	3.52	2e-16 ***
CD45	32	58	20	5	12	21	1.78	1.04	3.04	0.036 *
CD68	56	96	31	9	21	35	1.80	1.13	2.85	0.013 *
Continuous Features										
Proliferation	62	106	33	14	21	38	1.11	1.06	1.17	2e-16 ***
Average cell number	61	104	31	14	21	38	1.02	1.01	1.03	2e-16 ***

B

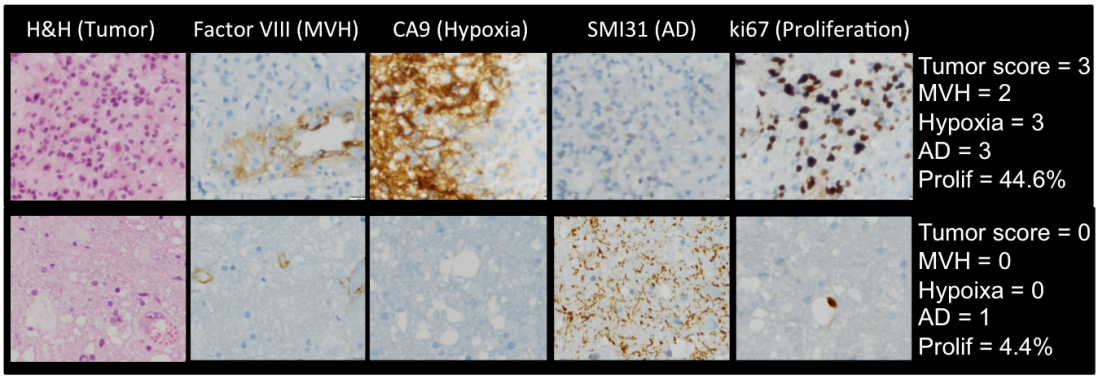

Abbreviations: TS=tumor score; Pt #, number of patients; Tiss #, number of tissue samples; AD, architectural disruption; MV(H), microvasculature (hyperplasia);

* p<0.05

** p<0.001

***p<0.0001

Figure 4-1 A. Association of histopathological parameters with tumor score. B. Comparison of histopathological features between a tumor sample (upper) and a treatment effect sample (lower).

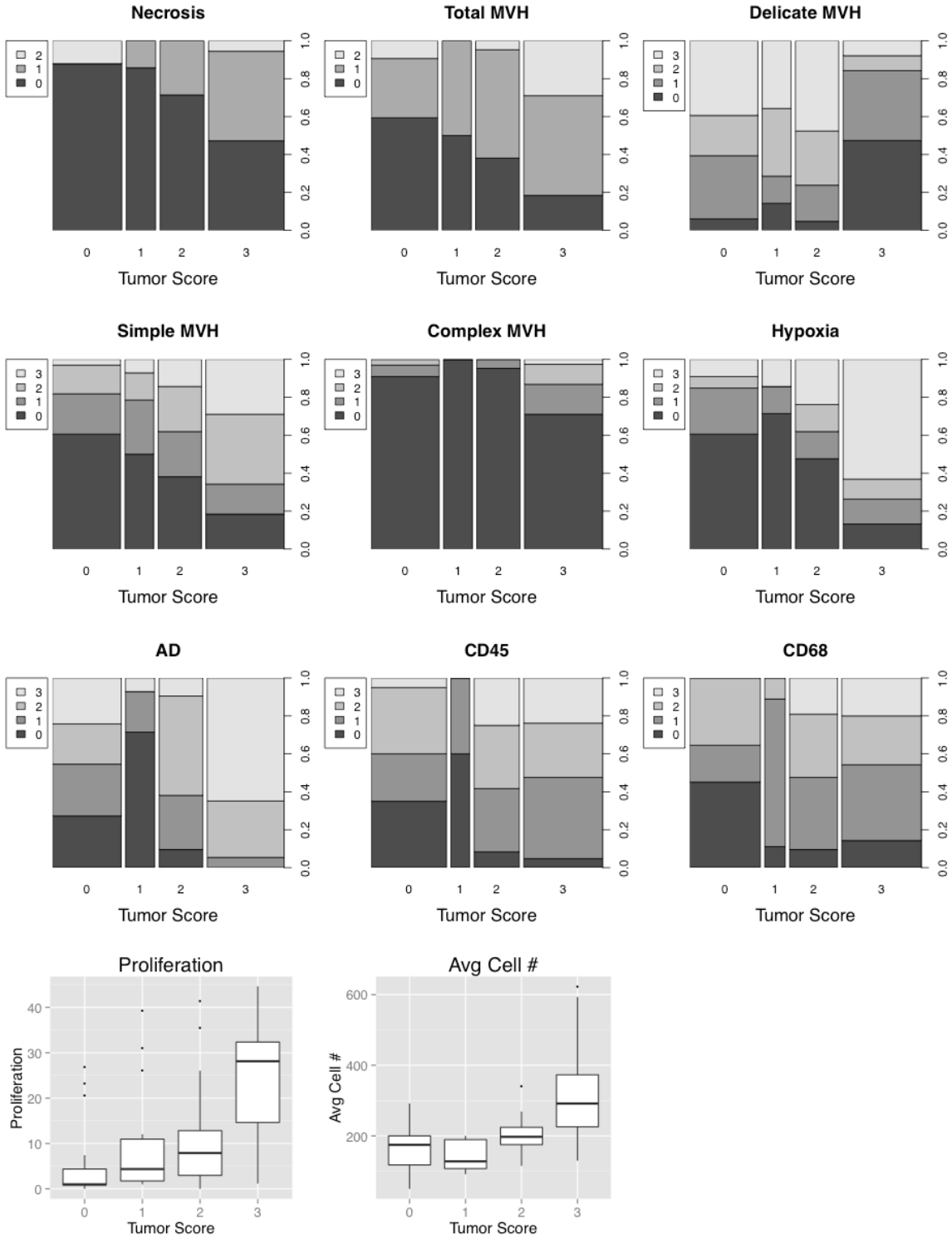

Figure 4-2 Spineplots (ordinal) and boxplots(continuous) of Histopathological parameters in relation to tumor score.

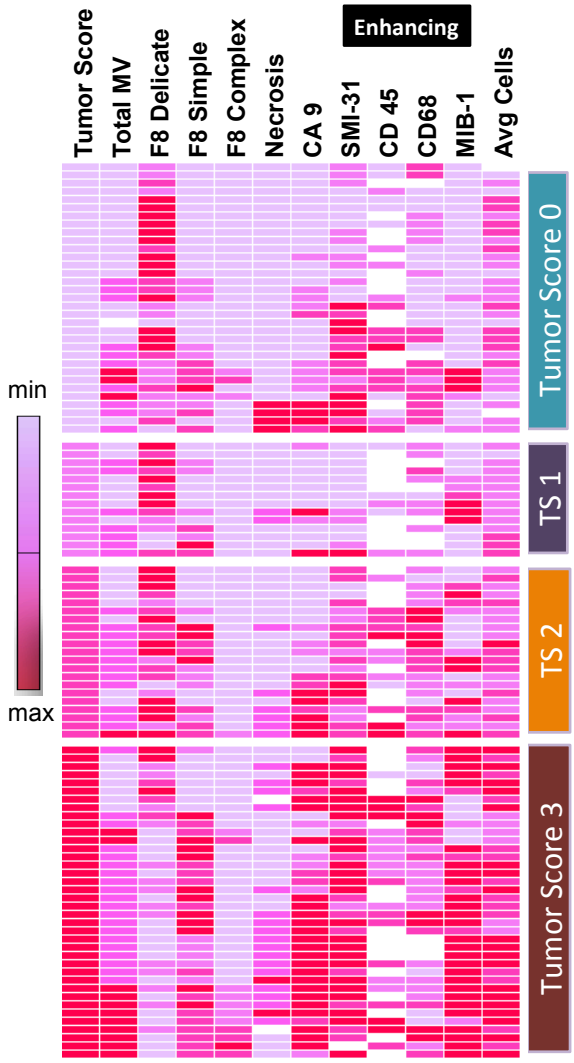

Figure 4-3 Colorcoded maps for histopathological features graded by tumor score for tissues taken from enhancing lesion (left) and non-enhancing lesion (right). Each row corresponds one tissue sample.

4.3.2 Association between Tumor Score and MRI Parameters

Summary statistics for association between tumor score and MRI parameters were shown in Table 4-2. Mixed effects model showed that only parameters extracted from DSC were significantly associated with tumor score. Higher rCBV from both nonlinear fitting and higher rPH nonparametric analysis were associated with higher tumor score (p=0.0008, p=0.002

respectively). Other than that, rADC from DWI was trending lower and CNI/rCho from MRSI were trending higher with higher tumor score, but neither of these reached statistical significance ($p>0.1$). In Figure 4-4 the distributions of these parameters are displayed as boxplots, demonstrating the large variations of all these parameters within the treatment effect group.

Multivariate analysis showed that the rCBV was the only parameter demonstrating association to the tumor score ($p=0.007$), and that adding rADC, CNI/rNAA had no contribution to the model fitting (Table 4-2).

Table 4-2 Association of *in vivo* MR parameters with tumor score within contrast-enhancing region (CE). Note that there were a much smaller number of samples that had MRSI data available for analysis.

MR	Summary Statistics						Univariate Mixed Efffect Model			
	Pt #	Tiss #	TS=0 #	TS=1 #	TS=2 #	TS=3 #	Odds Ratio	95% CI		P Value
DTI										
rADC	60	102	31	14	20	37	0.43	0.15	1.21	0.11
rFA	57	98	29	13	19	37	1.85	0.46	7.48	0.39
DSC										
rCBV_nlin	50	84	23	13	17	31	2.39	1.43	3.98	0.00082 ***
rPH_npar	50	84	23	13	17	31	2.48	1.40	4.40	0.0018 **
recov_npar	50	84	23	13	17	31	1.00	0.96	1.04	0.96
MRSI										
CNI	22	34	9	4	10	11	1.13	0.91	1.40	0.27
rCho	22	34	9	4	10	11	1.26	0.50	3.15	0.62
rCre	22	34	9	4	10	11	1.24	0.30	5.08	0.76
rNAA	22	34	9	4	10	11	0.03	0.00	3.20	0.14
rLip	22	34	9	4	10	11	0.55	0.09	3.22	0.51
rLac	22	34	9	4	10	11	0.14	0.01	2.15	0.16

Multivariate model				
MR	**Odds Ratio**	**95% CI**		**P Value**
rADC	0.62	0.18	2.11	0.44
rCBV	1.96	1.20	3.19	0.0071 **
CNI	1.06	0.87	1.30	0.56
rNAA	0.12	0.01	1.94	0.13

* $p<0.05$, ** $p<0.001$, ***$p<0.0001$

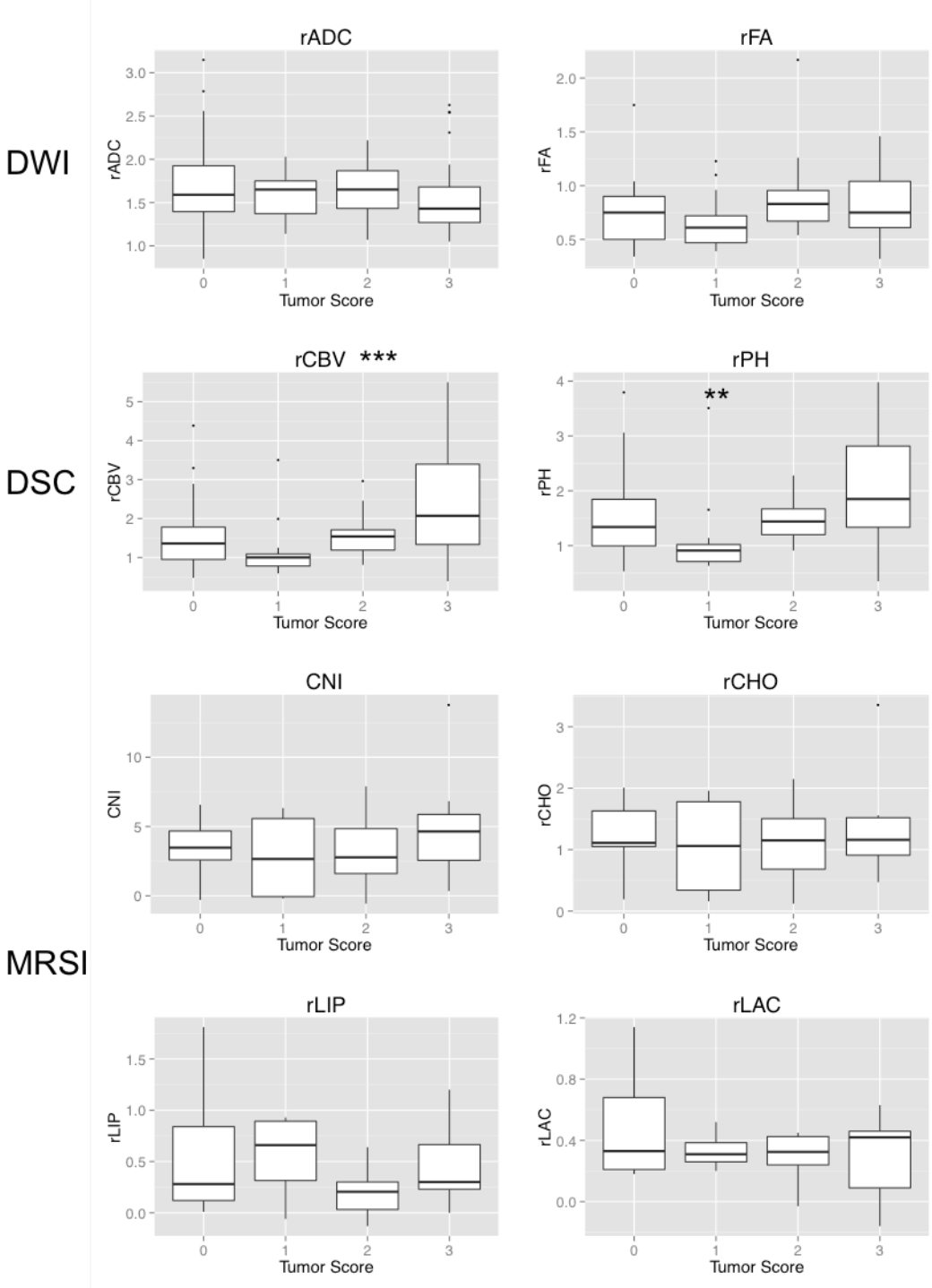

Figure 4-4 Boxplots of key MRI parameters versus tumor score in the sample-wise analysis.

4.3.3 Association between MRI Parameters and Histopathological Features

Summary statistics for association between key histology and MR parameters were shown in Table 3. Univariate mixed effects model demonstrated that higher rCBV were associated with many histopathological features including more necrosis (p=0.01), more architectural disruption (p=0.0003), less delicate MV (p=0.005), higher proliferation (p=0.002) and higher cell density (p=0.001). Higher lipid was associated with lower proliferation (p=0.01). ADC and CNI were not found to be significantly associated with any histopathological features. rLip was negatively associated with proliferation.

Table 4-3 Association among key histopathological parameters and MR parameters

	Tumor score	Necrosis	Delicate MV	Simple MVH	Complex MVH	Hypoxia	AD	Proliferation	Avg Cells
rADC									
rCBV	++	+	--			++	+++	++	++
CNI									
rLip								--	

4.3.4 Lesion-wise Analysis for MR Parameters vs Clinical Diagnosis

Boxplots of imaging variables within the entire CEL between patients with a clinical diagnosis of treatment effect vs true recurrence were shown in Figure 4-5. In general, the lesion-wise analysis showed consistent results as the biopsy-wise analysis. Logistic regression showed that only parameters from DSC were significantly associated with clinical diagnosis, with 90 percentile rPH (90% rPH), and volume of rCBV>2 (Vol(rCBV>2)) being higher for the subjects having a diagnosis of tumor recurrence (p=0.01, p=0.038). The CEL volume was in general higher for tumor recurrence, and was trending significance (p=0.08). rADC was trending lower and rCHO, rCNI, vol(rCNI>2) was trending higher in tumor recurrence, but did not reaching statistical significance (p>0.1).

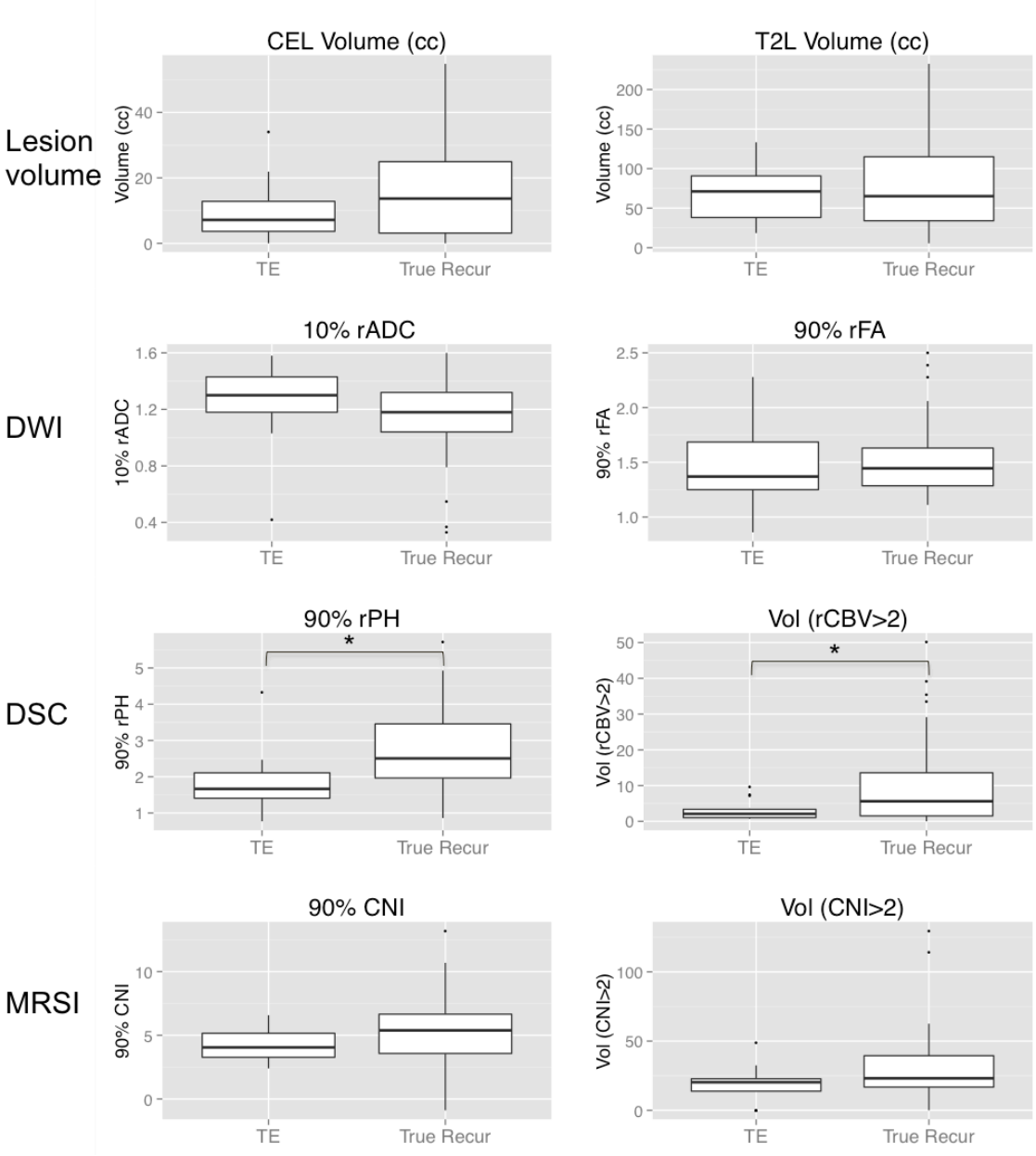

Figure 4-5 Boxplots of lesion volumes and MRI quantification within the contrast enhancement between treatment effect and tumor recurrence in the lesion-wise analysis.

Cases with a clinical diagnosis of between tumor and treatment effect are shown in Figure 4-6. The tumor case showed decreased ADC, elevated PH and elevated CNI/Cho compared to the treatment effect case. Figure 4-7 shows a case where whole lesion was confirmed treatment effect but MR imaging resembled tumor recurrence in all aspects including low ADC, high PH, high

CNI/Cho and low NAA. Despite the overall clinical diagnosis and characterization of tumor score =0 for the image guided sample from the circled region, its histopathological features demonstrated high microvasculature hyperplasia, abundant lymphocytes, macrophages and microglia. This patient had recently been treated with HSP-90 vaccine, which suggests that the explanation for the ambiguous imaging and histopathology results are that that the samples correspond to regions with a very active inflammatory response.

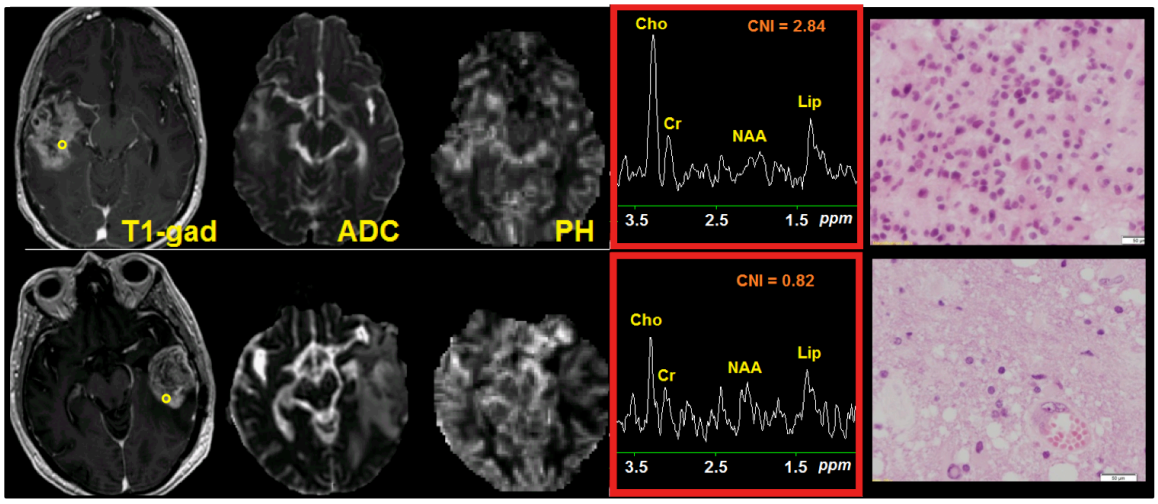

Figure 4-6 A tumor sample taken from true recurrence (upper) and a treatment effect sample taken from treatment effect lesion (lower). Comparing with treatment effect, tumor showed decreased ADC, elevated PH and elevated CNI/Cho. From left to right: T1-gad, ADC, PH, MRSI at the sample location, and H&E staining. On T1-gad image, yellow circle denotes the sample ROI.

A

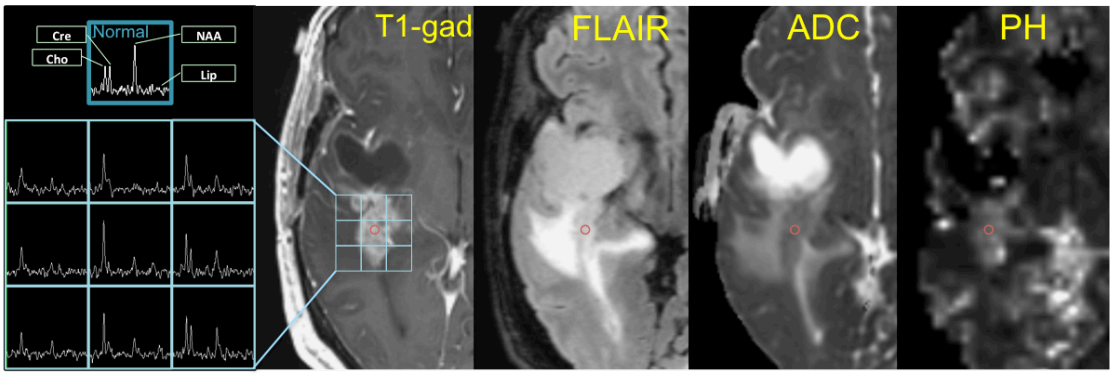

B Histopathology

Tumor Score	Factor VIII			Necrosis	Hypoxia	CD45	CD68	Proliferation	Avg Cells
	Delicate	Simple	Complex						
0	1	2	2	0	1	2	2	26.91	191

Figure 4-7 A case where the whole lesion was confirmed treatment effect but MR imaging resembled tumor recurrence with low ADC, high PH, high CNI/Cho and low NAA. Histophatological features of the biopsy-guided sample demonstrated high microvasculature hyperplasia, abundant lymphocytes, macrophages and microglia, indicating very active treatment related inflammatory response.

4.4 Discussion

Ambiguities in distinguishing tumor recurrence from treatment effects have a significant impact upon the management of patients with glioma and the interpretation of results obtained in clinical trials. Recent findings have emphasized the difficulty in differentiating true progression from pseudoprogression following treatment with radiation and temozolomide due to there being the possibility of a temporary increase in contrast enhancement that disappears in follow-up scans. The addition of anti-angiogenic treatments has further complicated the situation by providing a clear reduction in size of the contrast enhancing lesion without necessarily impacting the viability of the tumor. These issues have underlined the need for more advanced imaging techniques that are able to resolve ambiguities between treatment effect and recurrent tumor.

In the current study we evaluated 88 patients with a suspected diagnosis of recurrent GBM who presented for surgical resection and who were prepared to have image-guided tissue samples obtained from regions of contrast enhancement in order to make direct correlations of advanced imaging parameters with histological features. In contrast to other image-guided studies that have focused on samples with that were paucicellular and corresponded to regions of necrosis [11,15], we considered samples from contrast enhancing regions with more general characteristics of 'treatment effect'. This is important because radiation and chemotherapy can produce quite complicated histological features such as vascularization, demyelination and reactive cell proliferation that are caused by inflammatory responses [27-30]. Such histological findings develop, progress, and extend sporadically at different times and areas in the irradiated field of the brain for a long time after treatment and, biopsies from such lesions may demonstrate varying degrees of vascularization, cell density and demyelination [30-31]. Our histopathological findings in samples classified in treatment effect confirmed the presence of such variations. Although the overall scores were smaller than for tumor, varying degrees of necrosis, hypoxia, microvascular hypalasia, axonal disruptions, cell density and proliferation existed in the treatment effect samples.

Such complications in histopathological features in the radiation necrosis partially explains the variation we observed in the imaging parameters in the treatment effect samples. In particular there was a huge variation of rADC in the treatment effect group, with a 10 percentile of 1.23 (~984 mm^2/s) and 90 percentile of 2.5 (~2000 mm^2/s). Many factors can influence water diffusion in living tissue, including restriction (cellular compartmentalization, cell type and number, cell membrane density, and macromolecular size and type), physiochemical properties of tissue (viscosity and temperature), and perfusion [32]. Histologically, radiation induced injury has been described as an area of necrosis surrounded by a robust inflammatory cell infiltrate [33-34]. This can be seen in our results in that some of the treatment effect samples contained abundant

immune cells (CD45, CD68) and average cell count. Besides increased cellularity, high viscosity due to coagulation necrosis that contains creamy pus-like material with abundant leukocytes can contribute to ADC [35]. In previous reports of radiation necrosis that had low ADC values, the authors suggested that low ADC value could also be explained by the development of intracellular edema in the viable tumor cells during the transition to complete necrosis with liquefaction [6,7,36,37]. These observations suggest that low ADC values in regions of treatment effect can be caused by a mixed effect of high inflammatory cellular composition, high viscosity and cell swelling, while high ADC values may be reflective of simple acellular, cystic or liquefactive necrosis. Given these observations, it is not surprising that we found there was no association between ADC and cell density or other histopathological features in our analysis.

Multi-voxel 3D MRSI provides parameters that reflect cellular metabolism, and have been shown to differentiate tumor from non-tumor in patients with newly diagnosed glioma [26,44]. Based upon these and other results, we would anticipate recurrent tumor would be characterized by high Cho and low NAA levels, which corresponds to elevated CNI. [8-10,45-47]. As was the case for ADC, the main ambiguity here is expected to be in samples corresponding to treatment effect, because inflammatory cells and gliosis are also likely to have reduced NAA, increased Cho and CNI. The other complication for the MRSI data is that its inherent spatial resolution is much larger (1cc) than the size of the tissue sample that the association between in vivo and ex vivo results may be weaker than for the DWI and the DSC images. In our study, over half of the patients with a clinical diagnosis of treatment effect had elevated Cho and decreased NAA levels in the contrast enhancing lesion. This is consistent with previous reports of radiation injuries that reported the presence of inflammation, demyelination, and reactive astrogliosis [48]. Other studies indicated that Cho has exhibits a temporary increase during the first few months after radiation therapy and then decrease again as radiation necrosis begins to appear [49-51]. The presence of Lipid is indicative of necrosis, which can also result radiation injury. Lactate is most

frequently observed in high grade tumor but may also accumulate in areas of radiation injury. Neither of these was able to separate our treatment effect and recurrent tumor samples. In a recent study that we performed to compared ex vivo HRMAS spectra from samples of gliosis versus samples from recurrent GBM, our results indicated that myo-inositol/Cho was able to distinguish between them [52]. We were not able to use this metric in the current study as our MRSI data were acquired with an echo time (TE) of 144ms. Future studies will determine whether in vivo levels of myo-inositol/Cho can be used to separate these two options using 1H MRSI methods with short TE.

Of all imaging parameters analyzed in our study, the rCBV and rPH from DSC were the parameters that showed the best association with tumor scores and other histopathological features such as hypoxia, axonal disruption, proliferation, average cells. Values of rCBV have previously been shown to be associated with with tumor grade and histological findings of increased tumor vascularity, particularly in glioma [38-40]. Although they have demonstrated the potential for differentiating between treatment effect and recurrent tumor in other studies [15-21] it is not clear whether there is a single threshold that can be used to distinguish the 2 entities. We observed a big spread of rCBV values in the treatment effect that overlapped with tumor. As discussed previously, this may be due to radiation-induced cellular responses resulting in local neuroimmune and inflammatory reactions [41] that can mimic tumor progression. It is well known that inflammation is associated with neurovasculature in neurodegenerative diseases and shows increased rCBV [42,43]. Hu et al reported that rCBV between post-treatment radiation effect samples and tumor samples in a prospective image-guided study [15] but their radiation effect samples were restricted to those that were paucicellularity and lacked reactive cells. Our results showed that there was a wide range of cell counts (Avg. cells) in our treatment effect samples that also increased with rCBV ($p<0.0001$).

The multi-variate regression that we used to see whether using a combination of these imaging parameters could improve their association with outcomes was unable to improve upon the univariate analysis. One possible reason is that treatment induced inflammatory process could cause low ADC, high CBV and high Cho level at the same time, as was illustrated for the case in Figure 4-7. A three-layer pattern of low ADC and high CBV was found to be specific to radiation necrosis in a prior study [21] but was unable to be extended to the current, more general study.

Overall, there was a bigger overlap between the imaging and histological characteristics of treatment effect and recurrent tumor compared with those published by other authors. There are several reasons for these differences. First, many of the prior studies defined radiation necrosis as areas that did not progress on serial MRIs rather than having histological confirmation. Second, many studies included mixed grades of gliomas, with low grade gliomas having been treated with less aggressive therapies. One can expect that treatment induced inflammatory response of these patients were not as severe as in patients with GBM [53]. Third, we guided the selection of tissue sampling to spots that were suspicious for viable tumor with either abnormally decreased ADC, increased CBV and/or elevated CNI values. This means that we were more likely to have identified regions with ambiguous findings.

In conclusion, our biopsy-wise and lesion-wise analysis consistently demonstrated that rCBV was a useful imaging parameter in differentiating between treatment effect and recurrent tumor, and that it was associated with histopathological features that reflect malignancy. Despite these general findings, there was overlap in the values of imaging parameters between treatment effect and tumor that would make it difficult to be definitive based upon evaluating a single region of the tumor. Our studies also showed that the some of samples from the patients who had a clinical diagnosis of treatment effect had image guided tissue samples that were classified as recurrent tumor. There were also tissue samples defined as treatment effect which demonstrated similar histopathological and imaging features as the tumor samples. These ambiguities were caused by

treatment related inflammatory responses that involve vascularization and proliferation of immune cells. Finding imaging signatures of inflammation and gliosis will be critical for future progress in this field. Another factor of interest that was not considered in our comparison of imaging and histological parameters was the presence and role of non-enhancing tumor. Addressing these problems is likely to require a multi-modality approach and further analysis using image guided tissue samples.

4.5 References

1. Stupp R, Mason WP, van den Bent MJ, et al: Radiotherapy plus concomitant and adjuvant temozolomide for glioblastoma. N Engl J Med 352:987-996, 2005
2. Chamberlain MC, Glantz MJ, Chalmers L, et al: Early necrosis following concurrent Temodar and radiotherapy in patients with glioblastoma. J Neurooncol 82:81-83, 2007
3. Taal W, Brandsma D, de Bruin HG, et al: Incidence of early pseudo-progression in a cohort of malignant glioma patients treated with chemoirradiation with temozolomide. Cancer 113:405-410, 2008
4. Brandes AA, Franceschi E, Tosoni A, et al: MGMT promoter methylation status can predict the incidence and outcome of pseudoprogression after concomitant radiochemotherapy in newly diagnosed glioblastoma patients. J Clin Oncol 26:2192-2197, 2008
5. Hein PA, Eskey CJ, Dunn JF, Hug EB. Diffusion-weighted imaging in the follow-up of treated high-grade gliomas: tumor recurrence versus radiation injury. AJNR. Am. J. Neuroradiol. 25(2), 201–209, 2004.

6. Asao C, Korogi Y, Kitajima M et al. Diffusion-weighted imaging of radiationinduced brain injury for differentiation from tumor recurrence. AJNR. Am. J. Neuroradiol. 26(6), 1455-1460, 2005.

7. Tung GA, Evangelista P, Rogg JM, Duncan JA 3rd. Diffusion-weighted MR imaging of rim-enhancing brain masses: is markedly decreased water diffusion specific for brain abscess? AJR. Am. J. Roentgenol. 177(3), 709-712, 2001.

8. Zeng QS, Li CF, Zhang K, Liu H, Kang XS, Zhen JH. Multivoxel 3D proton MR spectroscopy in the distinction of recurrent glioma from radiation injury. J. Neurooncol. 84(1), 63-69, 2007.

9. Weybright P, Sundgren PC, Maly P, et al. Differentiation between brain tumor recurrence and radiation injury using MR spectroscopy. Am. J Roentgenol. 185(6):1471–1476, 2005

10. Smith EA, Carlos RC, Junck LR, et al. Developing a clinical decision model: MR spectroscopy to differentiate between recurrent tumor and radiation change in patients with new contrast-enhancing lesions. Am J Roentgenol. 192(2):W45–52, 2009.

11. Rock JP, Scarpace L, Hearshen D, et al. Associations among magnetic resonance spectroscopy, apparent diffusion coefficients, and image guided histopathology with special attention to radiation necrosis. Neurosurgery. 2004;54(5):1111.

12. Matsusue E, Fink J, Rockhill J, et al. Distinction between glioma progression and post-radiation change by combined physiologic MR imaging. Neuroradiology. 2010;52(4):297–306.

13. Huang J, Wang A-M, Shetty A, et al. Differentiation between intra-axial metastatic tumor progression and radiation injury following fractionated radiation therapy or stereotactic radiosurgery using MR spectroscopy, perfusion MR imaging or volume progression modeling. Magnetic Resonance Imaging. 2011;29(7):993–1001.

14. Elias AE, Carlos RC, Smith EA, et al. MR spectroscopy using normalized and non-normalized metabolite ratios for differentiating recurrent brain tumor from radiation injury. Academic Radiology. 2011;18(9):1101–1108.

15. Hu LS, Baxter LC, Smith KA et al. Relative cerebral blood volume values to differentiate high-grade glioma recurrence from posttreatment radiation effect: direct correlation between image-guided tissue histopathology and localized dynamic susceptibility-weighted contrast-enhanced perfusion MR imaging measurements. AJNR. Am. J. Neuroradiol. 30(3), 552–558, 2009.

16. Gahramanov S, Raslan AM, Muldoon LL et al. Potential for differentiation of pseudoprogression from true tumor progression with dynamic susceptibility weighted contrast-enhanced magnetic resonance imaging using ferumoxytol vs. gadoteridol: a pilot study. Int. J. Radiat. Oncol. Biol. Phys. 79(2), 514-523, 2011.

17. Kim YH, Oh SW, Lim YJ et al. Differentiating radiation necrosis from tumor recurrence in high-grade gliomas: assessing the efficacy of 18F-FDG PET, 11C-methionine PET and perfusion MRI. Clin. Neurol. Neurosurg. 112(9), 758–765, 2010.

18. Barajas RF, Chang JS, Segal MR, et al. Differentiation of recurrent glioblastoma multiforme from radiation necrosis after external beam radiation therapy with dynamic susceptibility-weighted contrast-enhanced perfusion MR imaging. Radiology. 2009;253(2):486-496

19. Fatterpekar GM, Galheigo D, Narayana A, Johnson G, Knopp E. Treatment-related change versus tumor recurrence in high-grade gliomas: a diagnostic conundrum – use of dynamic susceptibility contrast-enhanced (DSC) perfusion MRI. AJR. Am. J. Roentgenol. 198(1), 19-26, 2012.

20. Kong DS, Kim ST, Kim EH et al. Diagnostic dilemma of pseudoprogression in the treatment of newly diagnosed glioblastomas: the role of assessing relative cerebral blood

flow volume and oxygen-6-methylguanine-DNA methyltransferase promoter methylation status. AJNR. Am. J. Neuroradiol. 32(2), 382–387 (2011)

21. Jihoon Cha, Sung Tae Kim, Hyung-Jin Kim, Hye Jeong Kim, Byung-joon Kim, Pyoung Jeon, Keon Ha Kim, Hong Sik Byun. Analysis of the layering pattern of the apparent diffusion coefficient (ADC) for differentiation of radiation necrosis from tumour progression. European Radiology. 23(3), 879-886, 2013
22. Nelson SJ, Nalbandian AB, Proctor E, Vigneron DB. Registration ofimages from sequential MR studies of the brain. J Magn Reson Imaging. 1994; 4:877–883.
23. Hartkens T, D. R, Schnabel JA, Hawkes DJ, Hill DLG. VTK CISG Registration Toolkit: An open source software package for affine and non-rigid registration of single- and multimodal 3D images. In: BVM; 2002; Leipzig, Germany: Springer-Verlag, 2002: Abstract 185.
24. Lee MC, Cha S, Chang SM, Nelson SJ. Dynamic susceptibility contrast perfusion imaging of radiation effects in normal-appearing brain tissue: changes in the first-pass and recirculation phases. J Magn Reson Imaging. 2005; 21:683–693.
25. Lupo JM, Cha S, Chang SM, Nelson SJ. Dynamic susceptibility weighted perfusion imaging of high-grade gliomas: characterization of spatial heterogeneity. AJNR Am J Neuroradiol. 2005; 26:1446-1454
26. T. R. McKnight, S. M. Noworolski, D. B. Vigneron, S. J. Nelson, An automated technique for the quantitative assessment of 3D-MRSI data from patients with glioma. J Magn Reson Imaging. 2001; 13:167-177.
27. Skaper SD. The brain as a target for inflammatory processes and neuroprotective strategies. Ann NY Acad Sci. 2007; 1122:23–34
28. Engelhardt B. Molecular mechanisms involved in T Cell migration across the blood-brain barrier. J Neural Transm. 2006; 113:477–485

29. Schultzberg M, Lindberg C, Aronsson AF, et al. Inflammation in the nervous system: physiological and pathophysiological aspects. Physiol Behav. 2007; 92:121–128

30. Yoshii Y. Pathological review of late cerebral radionecrosis. Brain Tumor Pathol. 2008; 25:51–58

31. Julow J, Szeifert GT, Bálint K, et al. The role of microglia/macrophage system in the tissue response to 1-125 interstitial brachytherapy of cerebral gliomas. Neurol Res. 2007; 29:233–238

32. Schaefer PW, Grant PE, Gonzalez RG. Diffusion-weighted MR imaging of the brain. Radiology. 2000 Nov;217(2):331-45.

33. Jagannathan J, Bourne TD, Schlesinger D et al. Clinical and pathological characteristics of brain metastasis resected after failed radiosurgery. Neurosurgery. 2010; 66:208–217

34. Oh BC, Pagnini PG, Wang MY et al. Stereotactic radiosurgery: adjacent tissue injury and response after high-dose single fraction radiation: Part I—Histology, imaging, and molecular events. Neurosurgery 60:31–44, discussion 44–35. 2007. (book??)

35. Monabati A, Kumar PV, Kamkarpour A. Intraoperative cytodiagnosis of metastatic brain tumors confused clinically with brain abscess. A report of three cases. Acta Cytol. 2000; 44:437–441

36. Biousse V, Newman NJ, Hunter SB, Hudgins PA. Diffusion weighted imaging in radiation necrosis. J Neurol Neurosurg Psychiatry. 2003; 74:382–384

37. Kang TW, Kim ST, Byun HS et al. Morphological and functional MRI, MRS, perfusion and diffusion changes after radiosurgery of brain metastasis. Eur J Radiol. 2009; 72:370–380

38. Wong JC, Provenzale JM, Petrella JR (2000) Perfusion MR imaging of brain neoplasms. AJR Am J Roentgenol 174:1147–1157

39. Essock-Burns E, Phillips JJ, Molinaro AM, Lupo JM, Cha S, Chang SM, Nelson SJ. Comparison of DSC-MRI post-processing techniques in predicting microvascular

histopathology in patients newly diagnosed with GBM. J Magn Reson Imaging. 2013 Aug;38(2):388-400.

40. Lupo JM, Cha S, Chang SM, Nelson SJ. Dynamic susceptibility-weighted perfusion imaging of high-grade gliomas: characterization of spatial heterogeneity. AJNR Am J Neuroradiol. 2005 Jun-Jul;26(6):1446-54.

41. Gourmelon P, Marquette C, Agay D,Mathieu J, Clarencon D (2005) Involvement of the central nervous system in radiation-induced multi-organ dysfunction and/or failure. BJR Suppl/BIR 27:62–68

42. Paula Grammas. Neurovascular dysfunction, inflammation and endothelial activation: Implications for the pathogenesis of Alzheimer's disease. J Neuroinflammation. 2011; 8: 26.

43. Chen CC, Chen YC, Hsiao HY, Chang C, Chern Y. Neurovascular abnormalities in brain disorders: highlights with angiogenesis and magnetic resonance imaging studies. J Biomed Sci. 2013 Jul 5;20:47.

44. McKnight TR, von dem Bussche MH, Vigneron DB, et al. Histopathological validation of a three-dimensional magnetic resonance spectroscopy index as a predictor of tumor presence. J Neurosurg. 2002;97:794–802.

45. Schlemmer HP, Bachert P, Herfarth KK, Zuna I, Debus J, van Kaick G. Proton MR spectroscopic evaluation of suspicious brain lesions after stereotactic radiotherapy. AJNR Am J Neuroradiol. 2001 Aug;22(7):1316-24.

46. Verma N, Cowperthwaite MC, Burnett MG, Markey MK. Differentiating tumor recurrence from treatment necrosis: a review of neuro-oncologic imaging strategies. Neuro Oncol. 2013 May;15(5):515-34.

47. Clarke JL, Chang S. Pseudoprogression and pseudoresponse: challenges in brain tumor imaging. Curr Neurol Neurosci Rep. 2009 May;9(3):241-6.

48. Krouwer HG, Kim TA, Rand SD, et al. Single-voxel proton MR spectroscopy of non-neoplastic brain lesions suggestive of a neoplasm. AJNR Am J Neuroradiol 1998;19:1695–1703

49. Este`ve F, Rubin C, Grand S, et al. Transient metabolic changes observed with proton MR spectroscopy in normal human brain after radiation therapy. Int J Radiat Oncol Biol Phys. 1998;40(2):279–286.

50. Kaminaga T, Shirai K. Radiation-induced brain metabolic changes in the acute and early delayed phase detected with quantitative proton magnetic resonance spectroscopy. Journal of Computer Assisted Tomography. 2005;29(3):293–297

51. Szigety SK, Allen PS, Huyser-Wierenga D, Urtasun RC. The effect of radiation on normal human CNS as detected by NMR spectroscopy. Int J Radiat Oncol Biol Phys 1993;25:695–701

52. Srinivasan R, Phillips JJ, Vandenberg SR, Polley MY, Bourne G, Au A, Pirzkall A, Cha S, Chang SM, Nelson SJ. Ex vivo MR spectroscopic measure differentiates tumor from treatment effects in GBM. Neuro Oncol. 2010 Nov;12(11):1152-61.

53. Lawrence YR, Li XA, el Naqa I, Hahn CA, Marks LB, Merchant TE, Dicker AP. Radiation dose-volume effects in the brain. Int J Radiat Oncol Biol Phys. 2010 Mar 1;76(3 Suppl):S20-7.

Chapter 5
Clinically Feasible NODDI Characterization of Glioma Using Multiband EPI at 7T

In this chapter, we present an optimized multiband diffusion acquisition sequence at 7T. This sequence is able to accelerate diffusion acquisition by 3-fold and enables the characterization of brain tumor using the NODDI model within clinically feasible time. A SNR comparison is carried out between multiband and regular diffusion sequence at both 7T and 3T. The sequence was evaluated clinically and the variations in NODDI maps within the tumor are discussed.

5.1 Introduction

It is estimated that 68,530 new cases of primary brain and central nervous system tumors were diagnosed in the United States in 2012, and gliomas account for the majority of primary malignant brain tumors in adults [1]. Although low-grade lesions have a better prognosis, they often undergo transformation to a more malignant, higher grade at the time of progression. Both primary and recurrent gliomas infiltrate into adjacent brain tissue, making it difficult to define tumor margins. Proper diagnosis and grading, correct localization, and assessment of response to therapy are of great importance for all phases of treatment planning and selection.

Conventional T1- and T2-weighted MRI are applied in conjunction with an injection of a Gadolinium-based contrast agent to delineate structural abnormalities in the brain and assess regions where the brain–blood barrier has been compromised. However, neither are able to distinguish between the complex components within the anatomic lesion, which include, edema, gliosis, inflammation, cyst and active tumor. The specificity of conventional MRI is further compromised after treatment with radiation, temozolomide and anti-angiogenic agents [2].

Diffusion weighted imaging (DWI) is a rapidly expanding field in MRI and has been found

valuable in evaluating many neurological diseases [3]. By sensitizing MR signal to the random motion of water molecule protons at a microscopic level (of the order of 5–20μm), it is able to probe tissue microstructures in the brain such as axons, dendrites, glial cells, and extra-cellular spaces [4], in a manner that may provide valuable insights into tumor physiology. A simple and most widely used model to describe changes in signal intensity is diffusion tensor imaging (DTI), which represents water diffusion within a voxel as an ellipsoidal tensor. The apparent diffusion coefficient (ADC), which is estimated from this model, is a sensitive yet non-specific metric when evaluated in the highly heterogeneous tumor environment. A reduction in ADC may be associated with a decrease in vasognenic edema, or an increase in cell density. Increased ADC can be due to the formation of necrosis, an increase in interstitial fluid, or a decrease cell density due to effective treatment. The ability to distinguish between the mechanisms that lead to changes in ADC would be very important for treatment planning and monitoring patients. One approach to addressing this problem is to use a more sophisticated diffusion model and provides maps of parameters that represent different tissue compartments.

Neurite Orientation Dispersion and Density Imaging (NODDI) is a diffusion model that allows the quantification of specific microstructural features directly related to neuronal morphology [5]. In particular, the NODDI model assumes that water protons in neuronal tissue belong to one of three different pools: i) free water in areas such as the ventricles that contain CSF and exhibit isotropic diffusion; ii) restricted water within linear structures that represent dendrites and axons; and iii) water that is anisotropically hindered, representing diffusion within glial cells, neuronal cell bodies and extracellular environment. An orientation dispersion index (OD) is produced to describe the coherence of neurite directions, with a higher value indicating more coherent organization. Data that have been recommended to fit the NODDI model comprise a 2-shell 90-direction DWI sequence. Recent applications of NODDI that have provided encouraging results are from patients with multiple sclerosis [6,7], focal cortical dysplasia [8],

neurofibromatosis [9], neonatal encephalopathy [10], healthy newborn brain [11], as well as in spinal cord [12]. For patients with brain tumors it is anticipated that changes in vasogenic edema would be reflected in the free water compartment, and changes in cell density changes would be associated with changes in the hindered water compartment.

The availability of improved hardware and fast acquisition techniques make it possible to obtain 90-directional multi-shell DWI within a clinically feasible time. Conventional parallel imaging [13,14] results in a significant loss in SNR because the number of phase encoding steps that are acquired is reduced. For 2D multi-slice imaging, significant improvements can be achieved by exciting several slices at the same time using multiband radio frequency (rf) pulses. Since each slice is excited and sampled identically without skipping or missing k-space data, there is no loss in SNR. This technique has been successfully implemented in the human connectome project for accelerated diffusion imaging acquisition at 3T [15,16]. At higher field strengths, reduced T2 compromises the gain in SNR from the increased static magnetization, making the benefit of diffusion imaging at ultra-high field unclear. Other challenges, such as increased B0 and B1 field inhomogeneity, can also influence the quality of diffusion data. This has meant that the applications of ultra high field diffusion weighted imaging have been limited, and there has not yet been a direct comparison of the SNR between 3T and 7T.

In this paper, we report on the use of multiband DWI at 7T in order to obtain 90-directional multi-shell data within a clinically feasible acquisition time for patients with glioma. This included a comparison between the SNR for 3T and 7T, and the application of B1 mapping and distortion correction procedures for reducing the impact of variations in B0 and B1. The optimized multiband sequence was applied to generate both DTI and NODDI maps and to compare the values in tumor and normal appearing white matter (NAWM).

5.2 Data Acquisition

5.2.1 Multiband Acquisition

Multiband EPI data were obtained with 2-channel transmit and 32-channel receive head coil (Nova Medical, Wilmington, MA) on GE scanners. Three slices (40 mm apart) were simultaneously excited (multiband factor of 3, or MB=3) with a three-band RF excitation and axial spin-echo echo planner (SE-EPI) readout with phase encoding (PE) in the anterior-posterior (AP) direction, resulting in 60 slices for whole brain coverage with isotropic voxels of $2\times2\times2mm^3$ over a field of view of 256×256 mm^2. ¾ partial Fourier k-space sampling was employed to reduce TE and an in-plane acceleration factor of 3 (R=3) further shortened TE and reduced distortion due to susceptibility effects. With a 50 mT/m amplitude gradient system at $b=2000s/mm^2$, the TE obtained was 71.6ms and TR was 3200 ms. Calibration images were acquired at the beginning of the sequence with the same three-band excitation pulses but with different phase offsets applied to each band so that they could be unwrapped through a Fourier Transform (FT). This used the same SE-EPI readouts but was interleaved three times in order to fully sample the center of k-space.

A B1 mapping procedure was performed prior to the multiband acquisition, in order to determine the optimal transmit gain (TG) [17] needed to account for the B1 inhomogeneity at high field. B1 maps were generated using a gradient echo acquisition sequence (TR/TE=250/8 ms) with a 1ms adiabatic Bloch-Siegert pulse and the transmitter gain was automatically adjusted based on the median B1 of the image volume.

To correct for the susceptibility distortion, an additional b=0 image was acquired with reversed phase encoding blips using the same multiband sequence. This resulted in a pair of b=0 images with distortions going in opposite directions and allowed the susceptibility-induced off-

resonance field to be estimated with a method similar to that described in [20] and implemented in FSL [21]. The correction was then applied to the other diffusion images.

5.2.2 Volunteers Data Acquisition for SNR Comparison

Five volunteers received MR examinations with GE 3T MR 750 and GE 7T MR950 scanners (GE Healthcare, Maukesha, WI) using 32-channel receive-only head coils (Nova Medical, Wilmington, MA) and the same gradient system (50 mT/m amplitude and 200 T/m/s slew rate). Ten b=0 (T2 weighted) images were repetitively acquired with both standard EPI (MB=1) and MB=3 using the acquisition parameters described above. With the same TR, only the central slab of the brain was acquired for MB=1.

5.2.3 Phantom Data Acquisition for Determination of g factor Maps

A homogeneous spherical water phantom was used to evaluate the geometry factor (g-factor) map in order to quantify the fractional loss in SNR caused by the non-orthogonality of the array coil sensitivities [22]. Two datasets were acquired in each scanner using a gradient-recalled echo (GRE) imaging sequence (FOV = 256×256mm^2, matrix size = 64×64, slice thickness = 2mm). The first data set was used to assess the noise covariance matrix and was obtained with all RF pulses suppressed. The second data set served to determine coil sensitivity maps for each coil element and was obtained with regular RF excitation.

5.2.4 NODDI Data Acquisiton in Patients

Twenty patients with glioma (13 males and 7 females, median age = 54 years) were referred by physicians from the neuro-oncology service at our institution and recruited to this study. The characteristics of the patient population are summarized in Table 4. Tumors had been graded by histological examination of tissue samples obtained during biopsy or surgical resection: 10 had

grade II, 3 had grade III and 7 had grade IV. All patients had received prior treatment and 4 of them were showing progressive disease at the time of the scan.

Table 4. Patient Characteristics

No.	Age	Sex	Grade	RT	Chemotherapy	Disease state	image comments
1	59	M	2	yes	TMZ	recurrent	stable
2	65	M	4	yes	TMZ	recurrent	stable
3	48	M	2	YES	None	recurrent	stable
4	68	F	2	yes	TMZ	recurrent	progressive disease
5	60	F	3	yes	TMZ	recurrent	stable
6	34	M	2	no	None	recurrent	stable
7	50	M	3	no	TMZ	recurrent	stable
8	44	F	4	yes	TMZ	recurrent	progressive disease
9	48	M	4	yes	TMZ	recurrent	progressive disease
10	59	M	2	yes	TMZ	recurrent	stable
11	40	M	2	no	none	recurrent	stable
12	41	F	4	yes	TMZ	recurrent	stable
13	65	M	2	yes	RAD001	recurrent	stable
14	46	M	4	yes	TMZ	recurrent	stable
15	57	F	4	yes	none	recurrent	stable
16	55	M	4	yes	TMZ	recurrent	stable
17	27	F	2	yes	none	recurrent	stable
18	60	F	3	yes	TMZ	recurrent	stable
19	52	M	2	yes	TMZ	recurrent	stable
20	75	M	2	yes	none	recurrent	progressive disease

A two-shell diffusion imaging protocol was used for the 7T scanner with MB=3. This protocol included 7 b=0 images (and one additional b=0 image with reversed phase-encoding gradient for distortion correction), 30 directions at b=1000 s/mm^2, and 60 directions at b=2000 s/mm^2 with a total acquisition time of 5’42’’.

Anatomical images of these patients were acquired at the 3T scanner, including sagittal T1-weighted spin echo, axial 3D T2-weighted fast spin echo (FSE), axial fluid attenuated inversion recovery (FLAIR), contrast-enhanced 3D spoiled gradient-recalled acquisition in the steady state

(SPGR) T1-weighted and T1-weighted post-contrast spin echo images (T1-gad). In 14 patients, 24-directional DWI with regular SE-EPI sequence was also acquired (repetition time (TR)/echo time (TE) = 10s/99ms, voxel size=2x2x2mm^3, in-plane R=2, b=1000s/mm^2).

5.3 Post-processing and Analysis

5.3.1 Multiband Image Reconstruction

The image was aliased in both SI and AP directions, and was unfolded using the SENSE/GRAPPA procedure as described in [23]. The calibration data were first concatenated and Fourier transformed (FT) to generate the fully sampled k-space. Once the kernel has been generated, aliased images went through the reconstruction pipeline as illustrated in Figure 5-1. The under-sampled k-space data were first zero filled in the direction that no acceleration was performed (left-right, Figure 5-1B) and a standard GRAPPA/ARC procedure was applied to reconstruct the k-space data (Figure 5-1C). After an inverse Fourier Transform (ifft), the unalised images (Figure 5-1D) were individually transformed into k-space again (Figure 5-1E) in order to reconstruct the full k-space (Figure 5-1F) through a partial k-space reconstruction method called projection onto convex sets (POCS) [24]. A 2D fermi filter was then applied to reduce Gibbs ringing, and single coil images (Figure 5-1G) were combined with a sum of squares coil combination (Figure 5-1H).

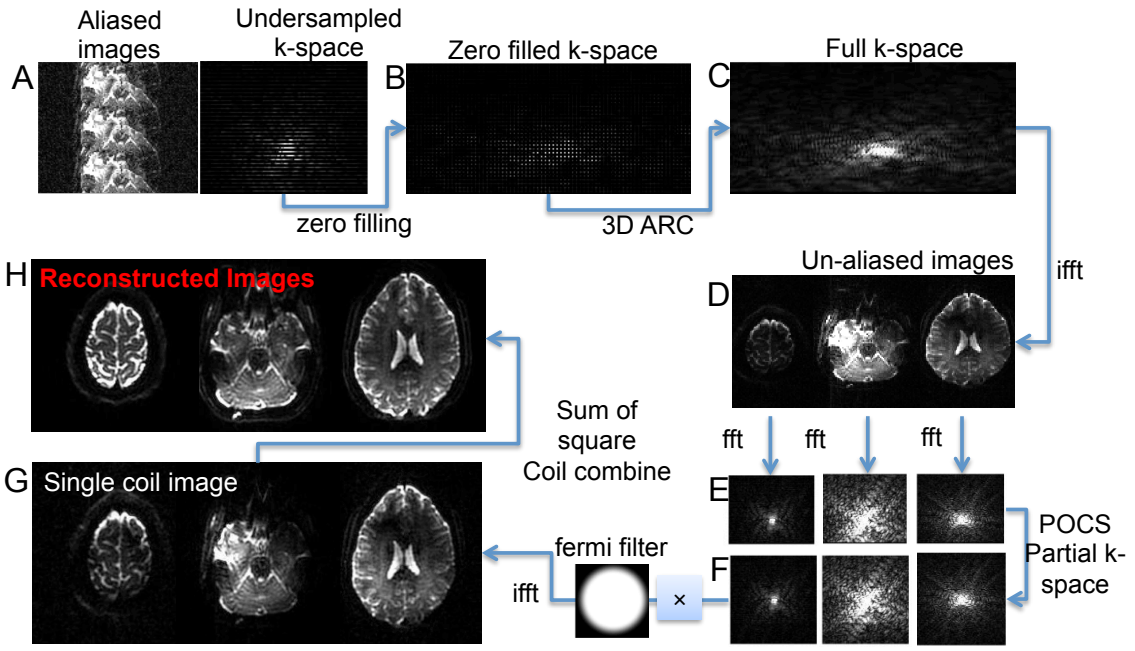

Figure 5-1 Reconstruction flowchart for a data set with MB=3 and in-plane R=3. A. Aliased image and its under-sampled k-space in PE direction. B. Zero filled k-space in the non-accelerated direction for un-folding aliased slices. C. Reconstructed full k-space with GRAPPA/ARC. D. Single coil un-aliased images. E. K-space of un-aliased slices. F. Full k-space after partial k-space reconstruction with POCS. G. Single coil images after Fermi filtering in k-space. H. Images reconstructed and combined using a sum of squares function..

5.3.2 SNR Calculation and Determination of g-factor

Each slice of the volunteer data was first smoothed with an 8-by-8 mean filter. The SNR was then calculated from Eq 5-1 for each voxel within the brain.

$$SNR = \frac{mean(voxel)}{std(voxel)} \qquad \text{Eq 5-1}$$

To calculate g-factor maps, phantom data were used to estimate relative coil sensitivity maps using the eigenvector method described by Walsh et al [25]. g-factor maps were then estimated from the sensitivity maps with the equation shown in Eq 5-2 [22] for different under-sampling schemes (MB1, R=3 and MB3, R=3).

$$g_j = \sqrt{[C_R^* \Psi^{-1} C_R]_{j,j} [(C_R^* \Psi^{-1} C_R)^{-1}]_{j,j}} \quad \text{Eq 5-2}$$

C_R is the coil sensitivity encoding matrix corresponding to an R fold accelerated acquisition. Ψ is the noise covariance matrix of the 32-channel coils, which was estimated by calculating the covariate matrix of the noise data acquired with RF excitation disabled.

5.3.3 NODDI and DTI Processing

After the multiband data were reconstructed, a susceptibility distortion correction was applied using the TOPUP method available in FSL [20,21]. Eddy current correction was followed by affine registration of the data to a reference volume image (eddy_correct, FSL).

The NODDI model was fitted within the brain mask using the NODDI MATLAB toolbox (http://www.nitrc.org/projects/noddi_toolbox/).. The two diffusivities representing the diffusion coefficient of the isotropic compartment (d_{iso}) and the intrinsic diffusivity of the intra-neurite compartments ($d_{//}$) were fixed as in the original model [5] to d_{iso}=3.00μm^2/s and $d_{//}$=1.70μm^2/s, which are the values commonly employed in literature for the free diffusivity of water particles in CSF and neural tissue in vivo at body temperature. The DTI fitting program in FSL was employed to fit DTI with weighted least squares tensor fitting (dtifit, FSL). Both models were fitted to the whole double-shell data set, and the DTI model was also applied separately to the shell acquired at b=1000s/mm^2 and a shell acquired at b=2000s/mm^2.

The following voxel-wise maps were obtained. For NODDI: the isotropic volume fraction (v_{iso}), the intra-neurite (restricted) volume fraction (v_{ic}), the extra-neurite (hindered) volume fraction (v_{ec}) and the orientation dispersion index (OD). In this study, we calculated the effective volume fraction for v_{ic} and v_{ec} so that $v_{iso}+v_{ic}+v_{ec} = 1$. For DTI, we evaluated ADC and fractional anisotropy (FA).

3T anatomical images were aligned to 7T diffusion images and resampled to the resolution of the diffusion data. Regions of interests (ROIs) included voxels within the region of T2 hyperintensity (T2L) on the FLAIR images and contrast-enhancing lesions (CEL) on the T1-gad images. NAWM, gray matter (GM) and cerebrospinal fluid (CSF) were defined from the 3D SPGR brain images. Median values of diffusion maps were analyzed within each ROIs.

5.3.4 Statistical Analysis

Statistical analysis was performed using Matlab R2012a. Nonparametric Wilcoxon rank sum tests were applied to assess difference in diffusion maps between tumor grades, or between different regions of interests (ROIs), including T2L, CEL, NAWM, GM and CSF. A P-value of 0.05 or smaller w considered to be significant. Adjustment for multiple comparisons was not applied due to the exploratory nature of this study.

5.4 Results

5.4.1 SNR Comparison between 3T and 7T

Figure 5-2A shows the center slice from two volunteers (V3 and V4) acquired with MB1 and MB3 at 3T and 7T. The median SNR of all slices was compared using a scatter plot for all 5 volunteers in Figure 5-2B. The median SNR was 68.4 and 43.9 for 3T MB1 and MB3 at 3T, and 50.2 and 46.1 for MB1 and MB3 at 7T.

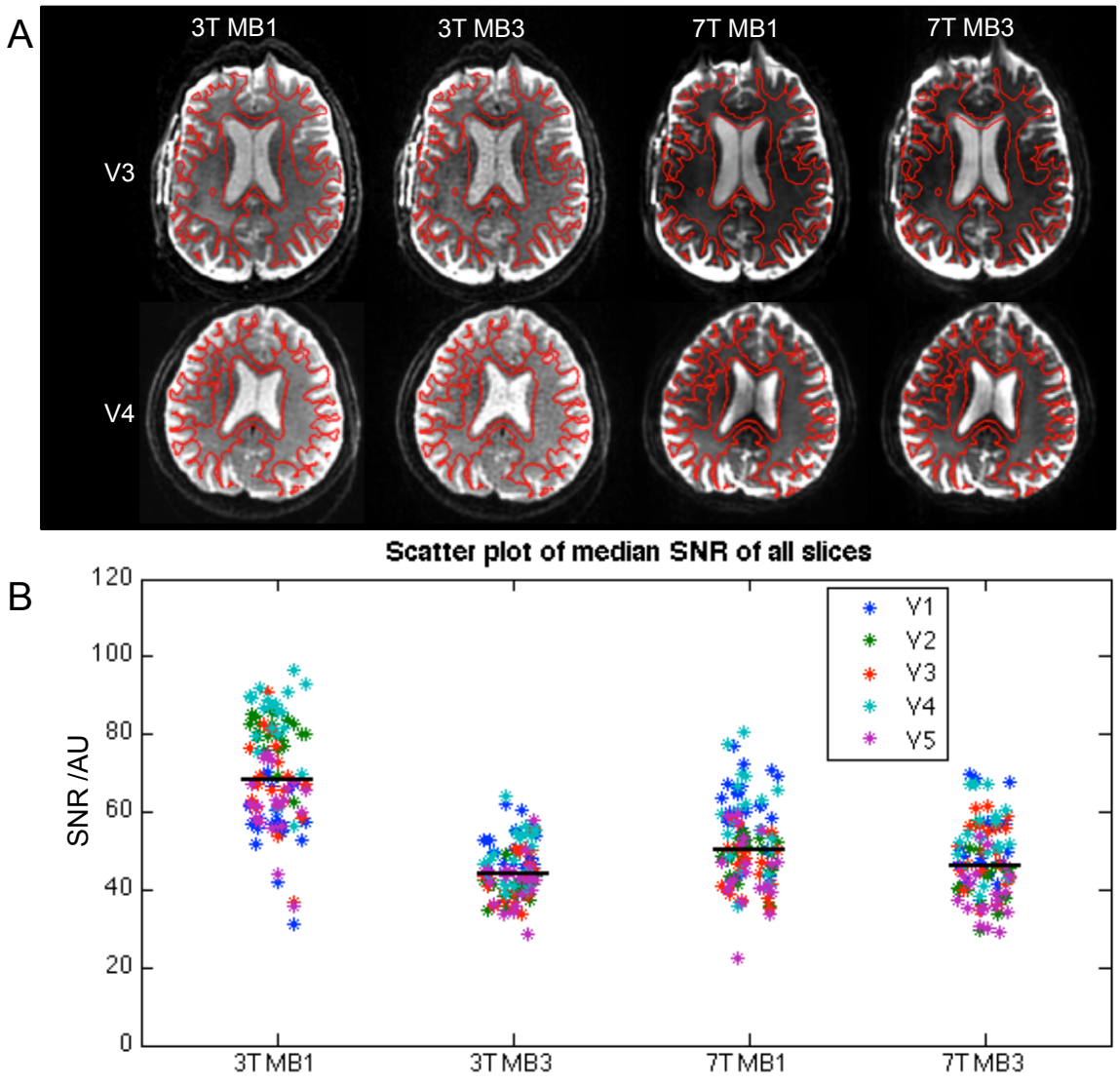

Figure 5-2 A. Center slice from two volunteers acquired with MB1 and MB3 at 3T and 7T. White matter is outlined in red. B. Scatter plot of median SNR values of all slices of 5 volunteers (V1-V5). Median SNR of each method was highlighted with a black line, with median SNR=68.4 and 43.9 for 3T MB1 and MB3, 50.2 and 46.1 for 7T MB1 and MB3.

5.4.2 g-factor Maps

g-factor maps (center slice and slices 40mm above and below) at 3T and 7T for different under-sampling schemes are shown in Figure 5-3A. Median 1/g values of all slices are shown in the scatter plot in Figure 5-3B, with the black line indicating the median value of each method. Median 1/g was 0.97 and 0.57 for 3T MB1 and MB3, 0.98 and 0.71 for 7T MB1 and MB3. The noise correlation matrix of the 3T 32-channel coil and 7T 32-channel coil are shown in Figure 5-3C, with the median value of off-diagonal correlation coefficients being 0.06 for 3T and 0.03 for 7T.

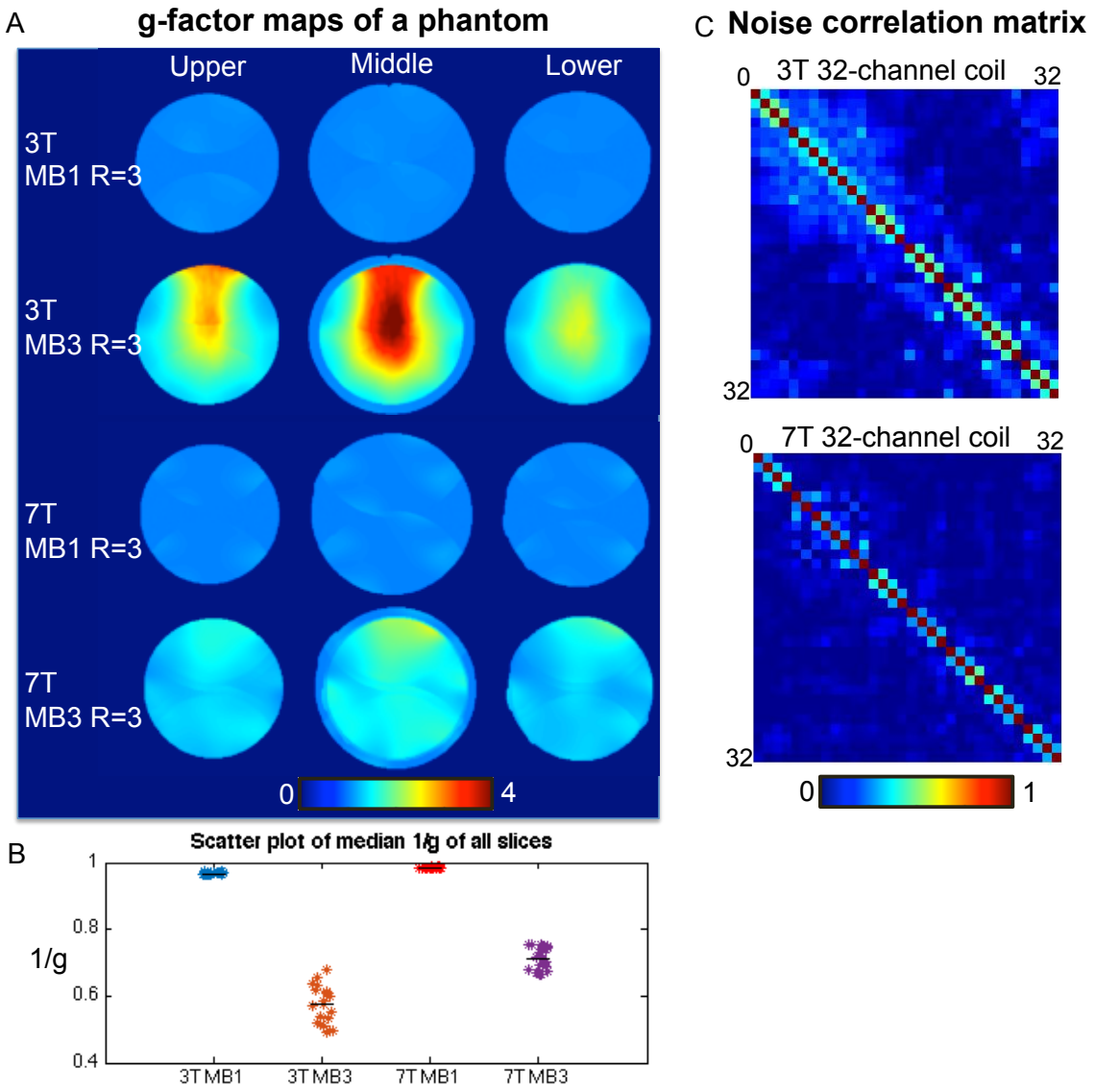

Figure 5-3 A. g-factor maps at 3T and 7T when under-sampling in one direction (MB1, in-plane, R=3), or in two directions (MB3, in-plane R=3) . g-factor maps were calculated from sensitivity maps estimated from a phantom data acquired at different field strength with 32-channel coils. B. Scatter plot of median 1/g value of all slices. Median 1/g of each method were shown in black line, with median 1/g=0.97 and 0.57 for 3T MB1 and MB3, 0.98 and 0.71 for 7T MB1 and MB3.

5.4.3 DTI and NODDI Results in Patients

5.4.3.1 Quality of Fit of DTI

14 out of 20 patients had 3T DTI data acquired with the product sequence. 3T and 7T DTI data were compared for this population, which included: (1) 3T regular DTI with b=1000, 24dir (2) 7T multiband DTI with b=1000, 30dir (3) 7T multiband DTI with b=2000, 60dir (4) 7T multiband double shell, 90dir. ADC and FA maps of a patient were shown in Figure 5-4A. The median values of ADC and FA within the NAWM, GM and CSF for 14 patients from different datasets are shown as bar plots in Figure 5-4B. For b=1000, the ADC was not significantly different between 3T and 7T within the NAWM, and FA was significantly higher at 7T ($p<0.0001$). The ADC and FA contrast was higher for 7T between NAWM, GM and CSF. As expected, the ADC obtained at b=2000 was significantly lower than ADC at b=1000 ($p<0.0001$) due to the non-Gaussian nature of water diffusion in a restricted environment, and the values fitted from the double shell were inbetween the values fitted from each shell. 3T data were aligned to the 7T data prior to quantification.

Correction for the susceptibility artifact with TOPUP at 7T is shown in Figure 5-4C. It can be seen that distortions were in the opposite direction between reversed and regular phase encoding blips, and with TOPUP the distortion was well corrected.

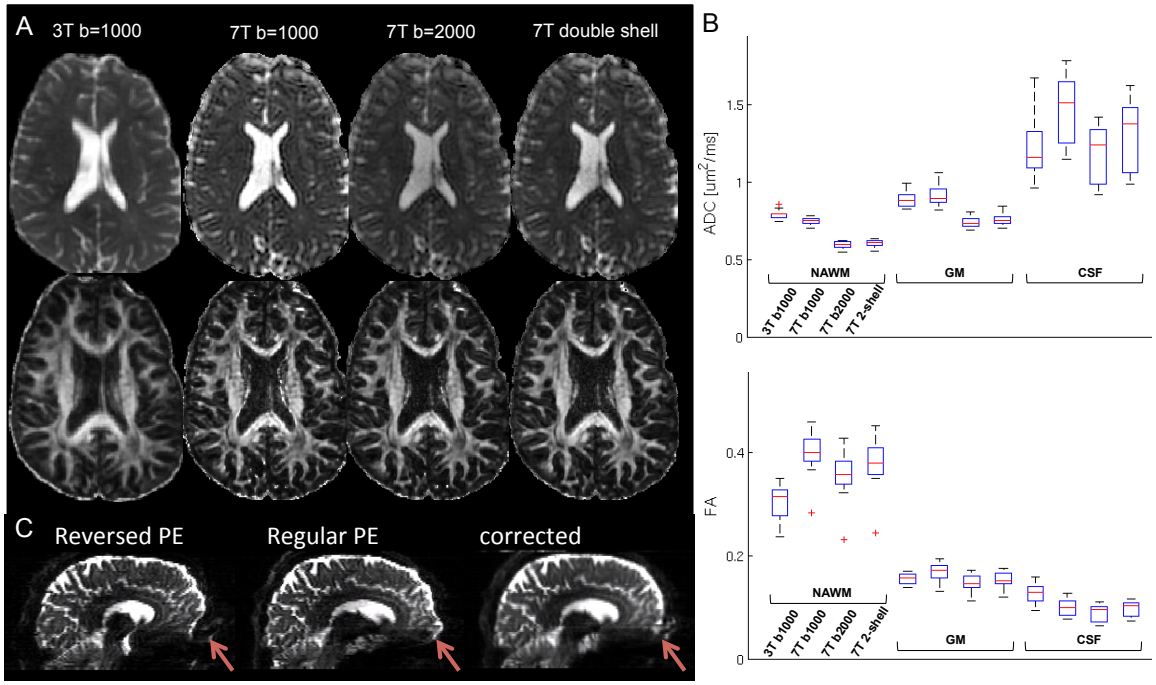

Figure 5-4 A. ADC and FA maps for patient data acquired with (1) 3T regular DTI, b=1000, 24dir (2) 7T multiband, b=1000, 30dir (3) 7T multiband, b=2000, 60dir (4) 7T multiband, double shell. B. Box plots of median ADC and FA within NAWM, GM, and CSF of 14 patients. C. Susceptibility artifact correction with TOPUP for 7T multiband acquisition.

5.4.3.2 Evaluation of NODDI Parameters

The mean and standard deviation of NODDI and DTI parameters in the NAWM, GM, CSF, T2L and CEL are summarized in Table 5 as a function of tumor grade. Within both the T2L and CEL, the ADC was significantly higher and the FA was lower than in NAWM ($p<0.0001$). Both v_{iso} and v_{ec} were significantly elevated ($p<0.0001$) compared to NAWM and v_{ic} was significantly decreased ($p<0.0001$). ADC was significantly lower in the CEL than the T2L, while OD and Vic were significantly higher ($p<0.01$, $p<0.001$), Viso was significantly lower ($p<0.05$) and Vec was not significantly different between the two lesions. These metrics were not found to be different between tumor grades ($p>0.1$).

Table 5. DTI and NODDI matrices values (Mean ± SD) in the T2L, CEL and NAWM, GM and CSF.

	T2L N=20	CEL N=11	NAWM N=20	GM N=20	CSF N=20
ADC	1.29 ± 0.21	0.97 ± 0.19	0.61 ± 0.03	0.79 ± 0.05	1.41 ± 0.20
FA	0.17 ± 0.04	0.17 ± 0.04	0.36 ± 0.05	0.15 ± 0.01	0.09 ± 0.02
OD	0.25 ± 0.08	0.35 ± 0.09	0.29 ± 0.03	0.46 ± 0.03	0.46 ± 0.03
Viso	0.37 ± 0.19	0.15 ± 0.12	0.09 ± 0.05	0.11 ± 0.08	0.66 ± 0.19
Vic	0.16 ± 0.08	0.32 ± 0.17	0.55 ± 0.06	0.38 ± 0.04	0.13 ± 0.07
Vec	0.43 ± 0.15	0.44 ± 0.21	0.28 ± 0.06	0.34 ± 0.08	0.07 ± 0.10

	G2 T2L N=10	G3 T2L N=3	G4 T2L N=7	G2 CEL N=5	G3 CEL N=1	G4 CEL N=5
ADC	1.27 ± 0.20	1.43 ± 0.22	1.24 ± 0.21	0.99 ± 0.25	1.05 ± 0.00	0.94 ± 0.16
FA	0.18 ± 0.04	0.13 ± 0.02	0.16 ± 0.04	0.18 ± 0.03	0.11 ± 0.00	0.18 ± 0.04
OD	0.23 ± 0.07	0.26 ± 0.10	0.28 ± 0.08	0.34 ± 0.08	0.44 ± 0.00	0.34 ± 0.11
Viso	0.36 ± 0.21	0.43 ± 0.23	0.35 ± 0.17	0.15 ± 0.10	0.41 ± 0.00	0.10 ± 0.10
Vic	0.15 ± 0.06	0.11 ± 0.05	0.19 ± 0.10	0.30 ± 0.24	0.24 ± 0.00	0.35 ± 0.12
Vec	0.46 ± 0.16	0.42 ± 0.19	0.39 ± 0.14	0.44 ± 0.26	0.34 ± 0.00	0.47 ± 0.19

NODDI maps of three patients who had lesions with different grades are shown in Figure 5-5, together with ADC and FA maps fitted from the same double-shell data, and 3T T1-gad and FLAIR images. All patients had received radiation therapy (RT) and were stable at the time of

scan. Within in the T2L, variations were seen in v_{iso}, v_{ic} and v_{ec}, that reflected different water mobility characteristics. Contrast enhancing lesions were present in all patients (blue arrow) and all demonstrated elevated ODI and v_{ic} compared to surrounding tissues. The white arrow indicates two regions of interest at the edge of T2L of the grade II and grade II patients. These regions could easily be missed on anatomical images and DTI maps, as their intensities were very close to NAWM, but they were highlighted in NODDI maps due to elevated v_{ec}.

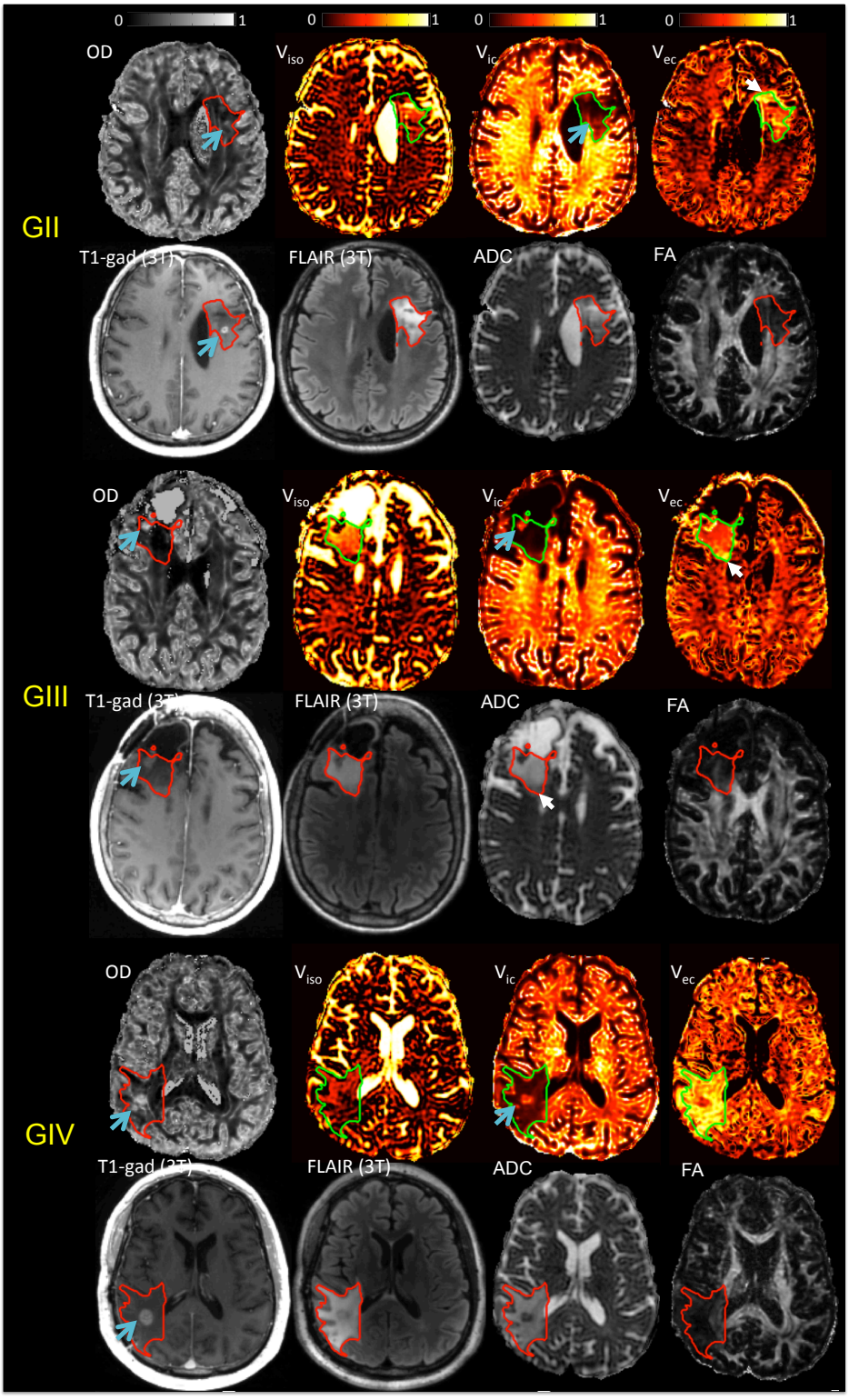

Figure 5-5. NODDI maps of three patients with lesions of different grades, together with ADC and FA maps fitted from the same double-shell data, and 3T T1-gad and FLAIR images. T2L were outlined, defined as the

hyperintensity abnormality in the FLAIR image. Within in the T2L, variations were seen in v_{iso}, v_{ic}, v_{ec}, reflecting different water mobility characteristics at different parts of the lesion. Contrast enhancing lesions were present in all patients (arrow) and all demonstrated elevated ODI and v_{ic}. The white arrow indicated two interesting regions at the edge of T2L of the grade II and grade II patients, which could easily be easily missed on anatomical images and DTI maps, but was highlighted due to elevated v_{ec}.

5.5 Discussion

The use of sophisticated diffusion models to provide improved the characterization of tissue composition is a promising technique for evaluating lesion heterogeneity in patients with glioma. The application of these models has typically been limited by the need to acquire a large number of diffusion directions at high b-values, which is not feasible in clinical settings [18,19]. In this study, we demonstrated the feasibility of acquiring multi-shell diffusion weighted data using the multiband technique within the same acquisition time that has been used to acquire routine DTI. The resulting data were fitted with both NODDI and standard DTI models. Our results showed that the NODDI maps were able to provide unique contrast within the T2L and are likely to provide information that is complementary to FA and ADC.

Major concerns for obtaining diffusion data using ultra high field strength MR scanners are increased variation in B0 and B1. In this study, we used 3-fold in-plane acceleration to shorten TE, as well as to increase the bandwidth in the phase-encoding direction in order to reduce the extent of distortion. To further correct for the susceptibility distortion, we used the TOPUP correction by adding an additional b=0 image with reversed phase encoding blips into the sequence [20-21]. The correction performed well for these data, as was illustrated in Figure 5-4. B1 inhomogeneity caused imperfect spin-echo over the entire brain, resulting in non-uniform signal intensity. To ameliorate this situation, we optimized the transmitter gain based on the median B1 of the image volume by incorporating the measured B1 field strength. It has been previously demonstrated that this technique can improve the situation by providing 82% of the

available spin echo signal [17]. The volunteer data in Figure 5-2 illustrate uniform images from central slice.

The performance of the EPI sequence at ultra-high field has been difficult to assess because the impact of the T2 values from brain tissue are unknown. We carried out a straightforward SNR comparison between 3T and 7T with the same hardware settings (gradient, coils) and acquisition parameters (TR, TE, k-space coverage and voxel size). Our results showed that without multiband, the SNR was higher at 3T (SNR≈68.4) than 7T (SNR≈50.2), indicating the shortened T2 at 7T outweighed the increased static magnetization and the total signal was reduced at the same echo time. However, when 3-fold acceleration was applied with multiband, the SNR was comparable between 3T (SNR≈43.9) and 7T (SNR≈46.1). The SNR loss after the simultaneous multi-slice acquisition is caused by the spatially dependent amplification of noise, known as the geometry factor, or 'g-factor'. Our estimation of g-factor maps showed that with MB=3 and in-plane R=3, g-factor was lower at 7T (g = 1.4) than 3T (g=1.75). This explains why the SNR is no longer superior at 3T with the multiband sequence. The improved g-factor map at 7T compared to 3T observed in our study is in agreement with the current literature [26]. It has been shown both in theory [27,28] and in experiments [26] that the g-factor is dependent upon B_0 field strength at high field (B_0>1.5T), and improves as the field increases, because the coil sensitivities grow progressively asymmetric [29] and become increasingly structured due to the shortening RF wavelength and related interference effects [30]. It has also been demonstrated that improvement in the g-factor at high field becomes more obvious as acceleration factor increases [26]. Our data demonstrated comparable SNR between 7T and 3T with 9-folder acceleration, and it can be predicted that even higher SNR would be achieved at 7T than 3T with higher acceleration.

The 3-fold acceleration that was achieved in the slice direction was the optimal that could be obtained with our current multiband technique, as the separation of aliased slices (40mm) is close to the coil size and SNR would be exacerbated if higher acceleration factors were used in that

direction. Another multiband technique, termed blipped-CAIPI can be implemented to both increase the SNR and achieve higher acceleration factor [31]. This technique can reduce the g-factor in simultaneous multi-slice acquisitions by introducing interslice image shifts and thus increase the distance between aliased voxels. This will be the target for future studies.

The multiband diffusion sequence was applied to the characterization of glioma using a 2-shell, 90-direction protocol that is straightforward to implement and sufficiently economical for clinical applications, yet sophisticated enough to distinguish three types of water diffusion in the brain. The ADC and FA maps fitted from this 7T protocol were first compared to the data acquired at 3T for patients with both data sets available (N=14). Our results showed that ADC values at b=1000mm^2/s within NAWM and GM were very close between 3T and 7T, with ADC higher in GM than NAWM, which is consistent with the trend reported in the literature [32]. It can also be seen that ADC at 7T demonstrated better contrast between different brain regions than 3T. One possible reason is that 3T data was aligned to 7T before the quantification, and the interpolation process could reduce the contrast. This may also explain why FA was lower in the 3T data in these regions. In general, ADC and FA maps acquired with multiband at 7T were comparable to those acquired with regular sequence at the 3T, and data quality was satisfying (Figure 5-4).

The NODDI model distinguishes three types of water diffusion behavior and each was quantified with a compartment fraction. When applied to tumor, it is natural to speculate that vasogenic edema would belong to v_{iso} given its isotropically fast diffusing movement. Invading tumor cells along fiber tracts should be categorized as v_{ec}, as they co-exist with glial cells in the space around the neurites. Our data were in general supportive of these assumptions by showing increased v_{iso} and decreased v_{ic} within T2L and CEL lesions compared to NAWM, consistent with increased edema and loss of neurons. The increased v_{ec} was likely to reflect the invading tumor cells. These assumptions should be validated with tissue samples, which were not available

in the current study. Patients recruited into this study were at different stage of disease and had received varying treatment, which may explain why these matrix were not found to be significant different between tumor grades.

The NODDI maps provided unique contrast across the tumor and highlighted interesting regions that could not be seen in ADC or FA maps. The different types of contrast observed may be reflective of progressive disease or of treatment effects that are worth noting for radiologists. Obtaining follow-up data at later time points would be valuable for tracking changes in these regions and may be helpful in interpreting them. Definitive verification and interpretation would require the use of image guided tissue samples and will be considered for future studies.

Another interesting finding that is observed in Figure 5 was that v_{ic} values was higher in CEL compared to the T2L. In NODDI model, v_{ic} represents neuron density, which conflicts with this finding as we know that the CEL contains less neurons than T2L and reflects either most aggressive tumor packed with dense tumor cells or non-specific changes related to treatment effect. This suggests that when applied to tumor, v_{ic} can no longer be interpreted as "neuron density". Rather, the elevated v_{ic} can be explained as the model saw restricted structures in that region with restrictions in all direction, which is consistent with the similarly elevated OD. This warned us that we should be very cautious when interpreting NODDI results in tumor, as this model was not directly built on tumor and some parameters were prefixed based on values in normal brain such as the intrinsic free diffusivity in v_{ic}.

In conclusion, we have demonstrated the feasibility of using multiband diffusion weighted imaging at 7T within 6 minutes in order to apply the NODDI model to characterize glioma. The data quality was encouraging and comparable to that acquired at 3T. We showed that NODDI maps provided unique contrast within the T2L lesion that is not seen in anatomical images or DTI maps. Such contrast may reflect the complexity of tissue compositions associated with disease

progression and treatment effects. Changes in v_{iso}, v_{ic} and v_{ec} in tumor lesions compared with NAWM were consistent with the alternations in tissue components within tumor. The histological analysis of image-guided tissue samples is needed in future studies to better understand these variations.

5.6 References

1. Dolecek TA, Propp JM, Stroup NE, Kruchko C. CBTRUS statistical report: primary brain and central nervous system tumors diagnosed in the United States in 2005–2009. Neuro Oncol 2012;14(Suppl 5):v1–v49.
2. Wen PY, Macdonald DR, Reardon DA, et al. Updated response assessment criteria for high-grade gliomas: response assessment in neuro-oncology working group. J Clin Oncol 2010;28:1963–1972.
3. A Lerner, MA Mogensen, PE. Kim, MS Shiroishi, DH Hwang, M Law. Clinical Applications of Diffusion Tensor Imaging. World Neurosurgery. 82(1-2):96-109, 2014.
4. Yablonskiy DA, Sukstanskii AL. Theoretical models of the diffusion weighted MR signal. NMR Biomed. 2010 Aug;23(7):661-81.
5. Zhang H, Schneider T, Wheeler-Kingshott CA, Alexander DC. NODDI: practical in vivo neurite orientation dispersion and density imaging of the human brain. Neuroimage. 2012 Jul 16;61(4):1000-16.
6. L. Magnollay, F. Grussu, C. Wheeler-Kingshott, V. Sethi, H. Zhang, D. Chard, D. Miller, O. Ciccarelli. An investigation of brain neurite density and dispersion in multiple sclerosis using single shell diffusion imaging. Proc 22nd Scientific Meeting of the ISMRM, Milan, Italy (2014), p. 2048
7. T. Schneider, W. Brownlee, H. Zhang, O. Ciccarelli, D. Miller, C. Wheeler-Kingshott. Application of multi-shell NODDI in multiple sclerosis. Proc 22nd Scientific Meeting of the ISMRM, Milan, Italy (2014), p. 0019

8. G.P. Winston, C. Micallef, M.R. Symms, D.C. Alexander, J.S. Duncan, H. Zhang. Advanced diffusion imaging sequences could aid assessing patients with focal cortical dysplasia and epilepsy. Epilepsy Res., 108 (2014), pp. 336–339
9. T. Billiet, B. Madler, F. D'Arco, R. Peeters, S. Deprez, E. Plasschaert, A. Leemans, H. Zhang, B.V. den Bergh, M. Vandenbulcke, E. Legius, S. Sunaert, L. Emsell. Characterizing the microstructural basis of "unidentified bright objects" in neurofibromatosis type 1: a combined in vivo multicomponent T2 relaxation and multi-shell diffusion MRI analysis. Neuroimage Clin, 4 (2014), pp. 649–658
10. P. Lally, H. Zhang, S. Pauliah, D. Price, A. Bainbridge, G. Balraj, E. Cady, S. Shankaran, S. Thayyil. Microstructural changes in neonatal encephalopathy revealed with the neurite orientation dispersion and density imaging (NODDI) model. Arch. Dis. Child Fetal Neonatal Ed., 99 (Suppl. 1) (2014), p. A14
11. N. Kunz, H. Zhang, L. Vasung, K.R. O'Brien, Y. Assaf, F. Lazeyras, D.C. Alexander, P.S. Hüppi. Assessing white matter microstructure of the newborn with multi-shell diffusion MRI and biophysical compartment models. Neuroimage, 96 (2014), pp. 288–299.
12. Grussu F, Schneider T, Zhang H, Alexander DC, Wheeler-Kingshott CA. Neurite orientation dispersion and density imaging of the healthy cervical spinal cord in vivo. Neuroimage. 2015 Jan 31.
13. Blaimer M, Breuer F, Mueller M, Heidemann RM, Griswold MA, Jakob PM. SMASH, SENSE, PILS, GRAPPA: how to choose the optimal method. Top Magn Reson Imaging. 2004 Aug;15(4):223-36.
14. Deshmane A, Gulani V, Griswold MA, Seiberlich N. Parallel MR imaging. J Magn Reson Imaging. 2012 Jul;36(1):55-72.
15. Sotiropoulos SN, Jbabdi S, Xu J, Andersson JL, Moeller S, Auerbach EJ, Glasser MF, Hernandez M, Sapiro G, Jenkinson M, Feinberg DA, Yacoub E, Lenglet C,Van Essen DC, Ugurbil K, Behrens TE. Advances in diffusion MRI acquisition and processing in the

Human Connectome Project. Neuroimage. 2013 Oct 15;80:125-43.

16. Setsompop K, Kimmlingen R, Eberlein E, Witzel T, Cohen-Adad J, McNab JA, Keil B, Tisdall MD, Hoecht P, Dietz P, Cauley SF, Tountcheva V, Matschl V, Lenz VH, Heberlein K, Potthast A, Thein H, Van Horn J, Toga A, Schmitt F, Lehne D, Rosen BR, Wedeen V, Wald LL. Pushing the limits of in vivo diffusion MRI for the Human Connectome Project. Neuroimage. 2013 Oct 15;80:220-33.
17. D Kelley, S Banerjee, W Bian, JP Owen, CP Hess, and SJ Nelson. Improving SNR and Spatial Coverage for 7T DTI of Human Brain Tumor Using B1 Mapping and Multiband Acquisition. Proc 21nd Scientific Meeting of the ISMRM, Utah, USA (2013), p. 3642
18. Assaf Y, Basser PJ. Composite hindered and restricted model of diffusion (CHARMED) MR imaging of the human brain. Neuroimage. 2005 Aug 1;27(1):48-58.
19. Panagiotaki E, Walker-Samuel S, Siow B, Johnson SP, Rajkumar V, Pedley RB, Lythgoe MF, Alexander DC. Noninvasive quantification of solid tumor microstructure using VERDICT MRI. Cancer Res. 2014 Apr 1;74(7):1902-12.
20. J.L.R. Andersson, S. Skare, J. Ashburner. How to correct susceptibility distortions in spin-echo echo-planar images: application to diffusion tensor imaging. NeuroImage, 20(2):870-888, 2003.
21. S.M. Smith, M. Jenkinson, M.W. Woolrich, C.F. Beckmann, T.E.J. Behrens, H. Johansen-Berg, P.R. Bannister, M. De Luca, I. Drobnjak, D.E. Flitney, R. Niazy, J. Saunders, J. Vickers, Y. Zhang, N. De Stefano, J.M. Brady, and P.M. Matthews. Advances in functional and structural MR image analysis and implementation as FSL. NeuroImage, 23(S1):208-219, 2004.
22. Pruessmann KP, Weiger M, Scheidegger MB, Boesiger P. SENSE: Sensitivity encoding for fast MRI. Magn Reson Med, 1999.
23. Blaimer M, Breuer FA, Seiberlich N, Mueller MF, Heidemann RM, Jellus V, Wiggins G, Wald LL, Griswold MA, Jakob PM. Accelerated volumetric MRI with a

SENSE/GRAPPA combination. J Magn Reson Imaging. 2006 Aug;24(2):444-50.

24. Yudilevich, E.; Stark, H.; Reconstruction from partial data in multislice magnetic resonance imaging. Acoustics, Speech, and Signal Processing, 1989. ICASSP-89, 1989 International Conference on 23-26 May 1989 Page(s):1488 - 1491 vol.3.
25. Walsh DO1, Gmitro AF, Marcellin MW. Adaptive reconstruction of phased array MR imagery. Magn Reson Med. 2000 May;43(5):682-90.
26. Wiesinger F, Van de Moortele PF, Adriany G, De Zanche N, Ugurbil K, Pruessmann KP. Parallel imaging performance as a function of field strength--an experimental investigation using electrodynamic scaling. Magn Reson Med. 2004 Nov;52(5):953-64.
27. Wiesinger F, Boesiger P, Pruessmann KP. Electrodynamics and Ultimate SNR in Parallel MR Imaging. Magn Reson Med 2004;52:376 –390.
28. Ohliger MA, Grant AK, Sodickson DK. Ultimate intrinsic signal-to-noise ratio for parallel MRI: Electromagnetic field considerations. MagnReson Med 2003;50(5):1018–1030.
29. Collins CM, Yang QX, Wang JH, Zhang X, Liu H, Michaeli S, Zhu XH,Adriany G, Vaughan JT, Anderson P, Merkle H, Ugurbil K, Smith MB,Chen W. Different excitation and reception distributions with a single-loop transmit-receive surface coil near a head-sized spherical phantomat 300 MHz. Magn Reson Med 2002;47(5):1026–1028.
30. Yang QX, Wang J, Zhang X, Collins CM, Smith MB, Liu H, Zhu XH,Vaughan JT, Ugurbil K, Chen W. Analysis of wave behavior in lossydielectric samples at high field. Magn Reson Med 2002;47(5):982–989.
31. Setsompop K, Gagoski BA, Polimeni JR, Witzel T, Wedeen VJ, Wald LL.Blipped-controlled aliasing in parallel imaging for simultaneous multislice echo planar imaging with reduced g-factor penalty. Magn Reson Med. 2012 May;67(5):1210-24.
32. Helenius J, Soinne L, Perkiö J, Salonen O, Kangasmäki A, Kaste M, Carano RA, Aronen HJ, Tatlisumak T. Diffusion-weighted MR imaging in normal human brains in various age groups. AJNR Am J Neuroradiol. 2002 Feb;23(2):194-9.

Chapter 6
Summary

The research being performed in this thesis has focused on the development, optimization and application of acquisition and quantification methods for diffusion imaging, with the objective of improving the interpretation of routine diffusion maps in high-grade glioma, as well as to bridge the gap between advanced diffusion models and their clinical application using fast imaging techniques.

Changes in apparent diffusion coefficient (ADC) were first analyzed with different quantification methods and their associations with clinical outcomes were examined for patients with newly diagnosed GBM being treated with a combined therapy that includes bevacizumab. Due to the strong anti-VEGF effect of bevacizumab and the reduction on vasogenic edema, there was a rapid decline of ADC percentile values immediately following onset of therapy in almost all subjects. However, the ADC percentile values were lower for the patients who progressed early. This suggests that tracking the changes in ADC using serial histogram analysis could potentially assist radiologists in monitoring patient response to therapy that includes bevacizumab. We hypothesize that this is due to the anti-angiogenic effect of bevacizumab reducing the extent of vasogenic edema at this time point and therefore allowing the observed ADC values to more accurately reflect the residual tumor burden.

To further validate this hypothesis and to determine whether ADC percentile value at early follow-up is a bevacizumab-specific biomarker, we performed similar ADC analysis methods to datasets acquired in two other clinical trials where patients were treated with RT concurrently with either temozolomide, or temozolomide and enzastaurin. Our results showed that the ADC percentile value was associated with survival for the treatment that included bevacizumab, but not for the other treatments. This supported our hypothesis, and suggests that the impact of treatment

regimen on the pattern of changes in imaging parameters must be considered when deciding patient care.

A major challenge in monitoring patient response after being treated with combined radiation and chemotherapy is the difficulty in distinguishing treatment related effect from the true tumor recurrence, both of which manifest contrast enhancement in T1-gad image. To better understand this problem, we conducted image-guided tissue sampling to directly correlate the tumor histopathology to various imaging contrasts that included diffusion weighted imaging, perfusion imaging and spectroscopic imaging. Our results demonstrated that elevated cerebral blood volume (CBV) was the best indication of true recurrence. However, overlap between the two groups were observed in all imaging parameters, as well as many of the histopathological features, including cell density, microvascular hyperplasia, level of axonal disruptions and hypoxia. One possible explanation for the big variations observed with treatment effect was presence of inflammatory responses that increase vascularization and immune cells proliferation. This makes characterizing recurrent lesions with MR measurements extremely challenging.

These results highlighted the challenges of using ADC in the management of patients with high-grade glioma. The availability of improved hardware and fast acquisition techniques make it possible to obtain more diffusion weighted directions within a clinically feasible time that allows advanced diffusion models to be applied. These models aim to disentangle specific factors contributing to the exhibited patterns of DTI indices and can potentially add specificity to the evaluations of glioma. We optimized the multiband diffusion acquisition technique at 7T with the application of B1 mapping and distortion correction procedures to reduce the impact of B0 and B1 field variations at ultra high field. This sequence allows 3-fold acceleration compared to the regular diffusion acquisition, and our SNR comparison demonstrated encouraging data quality. The optimized multiband sequence was applied in patients with glioma to generate both DTI and NODDI maps. In the NODDI model, water protons into three pools with different diffusion

characteristics and can be potentially used to distinguish tissue compartments such as edema, tumor cells and intact neuron in gliomas. Our results demonstrated that NODDI maps provided unique contrast within the tumor lesion that is not seen in anatomical images or DTI maps. Such contrast may reflect the complexity of tissue compositions associated with disease progression and treatment effects. The histological analysis of image-guided tissue samples is needed in future studies to better understand these variations.

In conclusion, this thesis has explored the value of using diffusion imaging to assess gliomas from several different perspectives. While some results are preliminary and further evaluation is needed, we have successfully demonstrated the potential of using combined advanced diffusion acquisition, post-processing and modeling techniques in adding specificity to the characterization of gliomas. These techniques are not restricted to applications in patents with brain tumor and can be extended to subjects with other brain diseases.

Appendix A Scripts

A.1 process_DTI_brain

(/netopt/share/bin/local/brain/process_DTI_brain)

To apply diffusion tensor fitting to get ADC, FA, ev1, ev2, ev3 and t2di, run this script within t-folder.

Usage: process_DTI_brain dicom_dir rootname

Example: process_DTI_brain E1234/11 t3333

This script:
1. Convert dicom images to nifti format
2. Check if TOPUP DTI is acquired, if yes, apply TOPUP correction
3. Apply eddy current correction to diffusion data
4. Apply DTI fitting with weighted least square fitting
5. Align generated diffusion maps to anatomical images by aligning t2di image to FLAIR

Notes: it extracts b-value and b-vector information from dicom header. In old datasets where these information is not available in the header then try a older script: make_diffu_brain

A.2 align_DTI

(/netopt/share/bin/local/brain/align_DTI)

To align DTI maps (ADC, FA, ev, t2di) to anatomical images, run this script within diffusion folder: e.g. /diffusion_b=1000/

Usage: align_DTI t# anatomical_root

Example: align_DTI t1234 fla (or alternatively fsea, t1va)

This script:
1. Align t2di to fla/fsea (fa to t1va) with align_tool.dev (essentially using flirt) to get the transformation
2. Apply the transformation to diffusion images

Notes: if aligning to fla doesn't work well, recommend trying t1va

A.3 process_NODDI_3T

(QB3 grid access required)

To generate NODDI on separately acquired data sets acquired with matched FOV and matrix size (no registration was performed between the two datasets), run this script within t-folder.

Usage: process_NODDI_3T dti_dicom_dir hardi_dicom_dir [o basename]

Example: process_NODDTI_3T E1234/10 E1234/8 [o test]

This script:
1. Import dicom images to nifti and combine the two datasets into one.
2. Apply eddy current correction
3. Generating NODDI on grid
4. Apply DTI fitting for the two-shell data
5. Convert nifiti results to idf/int2
6. Align results to anatomical images (through aligning t2di to fla)

Notes: if no [-o] is given, this script assumes it is running within a t-folder and will extract the t-number from the directory path and use that as the output rootname.

A.4 process_NODDI_7T

(QB3 grid access required)

To generate NODDI on a 90-direction two-shell diffusion data set acquired with multiband sequence. Run this script within t-folder.

Usage: process_NODDI_7T E_number/exam_number

Example: process_NODDTI_3T E1234/10

This script:
1. Reconstruct multiband diffusion data on grid with ‘recon_multiband_epi’
2. Apply TOPUP correction
3. Apply eddy current correction on grid
4. Apply NODDI fitting on grid with ‘generate_NODDI_grid’
5. Apply DTI fitting for the two-shell data
6. Convert nifty results to idf/int2

Notes: Raw pfiles are supposed to be in E1234/10_raw, including, t*_multiband_dti_noddi.7, t*_.ref.dat, t*_vrgf.dat. This script also assumes it is running within a t-folder and will extract the t-number from the directory path and use that as the output rootname.

A.5 eddy_correct_grid

(QB3 grid access required)

(/netopt/share/bin/local/brain/eddy_correct_grid)

To parallelize eddy_correct by diffusion directions. Run this the same way as running eddy_correct.

Usage: eddy_correct_grid 4dinput 4doutput reference_volume

Example: eddy_correct_grid data data_ec 0

This script:
1. Split 4D data into multiple 3D data with each one represents one DWI
2. Run eddy_correct on grid for each DWI
3. Combine results back into 4D

A.6 generate_NODDI_grid

(QB3 grid access required)

(/netopt/share/bin/local/brain/generate_NODDI_grid)

To parallel NODDI processing by slice. Run this in the data folder.

Usage: generate_NODDI_grid -k <filename>

Compulsory arguments (You MUST set all of):
- -i, data dti data file
- -o, out Output basename
- -m, mask Bet binary mask file
- -r, bvecs b vectors file
- -b, bvals b values file

Example: generate_NODDI_grid -i data_ec.nii.gz -o t1234 -m data.mask_mask.nii.gz -r data.bvec -b data.bval

This script:
1. Split input data into slices
2. Parallelize NODDI fitting for each slice on grid with 'NODDI_matlab_grid_single'
3. Combine results with 'NODDI_combine_results'

Notes:

1. As it runs, it will generate many temp files in the same directory, but the files to track the progress is called NODDI_grid_job.o***.#. # is the job number, or slice number. If there is error processing, check NODDI_grid_job.e***.#
2. Once the job gets finished, it will combine results of all slices to one. And all the intermediate files will be saved in tmp_files folder just in case, you can remove the folder later if find the combined results looks right. And the NODDI_gird_job.o/e files will be moved to grid_io_noddi folder.
3. The progress is recorded in NODDI_grid_job.o******.**, you can track while it's running, but once it finished running, these files will be moved to grid_io_NODDI
4. In addition to regular NODDI outputs, two more maps are generated: abs_fecvf = fecvf*(fiso_inv), abs_ficvf = ficvf*(fiso_inv). Therefore fiso + abs_ficvf + abs_fecvf = 1. This is performed because ecvf and icvf are not normalized so it's hard to compare with iso.

A.7 recon_multiband_epi

(QB3 grid access required)

(/netopt/share/bin/local/brain/recon_multiband_epi)

To parallelize multiband EPI reconstruction (diffusion, fMRI) by slice*pass. Run this in the data folder.

```
Usage:    recon_multiband_epi -s slice_num -p pass_num
     [ -o output_path ]
     [ -q queue ]
     [ -c cluster ]
     [ -h help info]
     -s slice_number         slice number to reconstruct (enter "all" for grid recon)
     -p slice_number         pass number to reconstruct (enter "all" for grid recon)
     -o output_path          output_path (default = cwd)
     --suffix suffix           suffix of output files
     -q queue                queue for grid submission
     -c cluster              options qb3(default) or rad
     -h                        print this help text

Example: recon_multiband_epi –s all –p all
              recon_multiband_epi –s 10 –p 3  (reconstruct slice 10 in pass 3)
```

This script:
1. Automatically detect input files in current directly, including: raw_file, ref_file (ref.dat file for EPI phase correction), vrgf_file (vrgf.dat file for ramp sampling correction), and one dicom_file to extract the header info for reconstructed dicom images.
2. Calculate grappa kernel by calling compiled matlab function ‘process_cal’

3. Parallelize data reconstruction on grid, Reconstruction is done with compiled matlab function 'recon_multiband_grid'
4. Clean up intermediate files.

Notes: the number of jobs = number of passes * number of slices (for 98dir 20slices, #jobs = 1960, which takes about 20min-1hr on qb3 grid)

A.8 recon_multiband_grid.m

This is the core function that takes multiband raw files and reconstruct dicom images.

Usage: recon_multiband_grid(pfile, reffile, vrgffile, dcmfile, pass, slice);

This function:
1. Import calibration data to generate grappa kernel
2. Apply grappa/ARC to reconstructed partial k-space
3. Apply POCS to reconstruct full k-space
4. Fermi filtering to reduce Gibbs ringing.
5. Sum of squares coil combination to combine images.

A.9 NODDI_matlab_grid_single.m

This is the core function that does NODDI fitting. This script is a wrapper around the NODDI toolbox online (https://www.nitrc.org/projects/noddi_toolbox/) with the following modifications:
1. inputs and outputs are customized to our dataset
2. Two repeatedly called functions in NODDI toolbox (repmat, legendre) that are time-consuming are replaced by equivalent C code written by Akash Kansagra.
3. After NODDI fitting is done, NODDI maps Vec and Vic are further normalized as abs_Vec = (1-Viso)*Vec, abs_Vic = (1-Viso)*Vic, so that Viso + abs_Vec + abs_Vic = 1

Usage: NODDI_matlab_grid_single(slice_root, slice_mask_root, bvecfile, bvalfile, sl)

This script calls functions in NODDI toolbox to apply NODDI modeling and output NODDI maps.

A.10 plot_serial_curve.m

This function displays serial data (curves & histograms) for patients with serial follow-up scans.

Preparations:
1. roi_analysis folder needs to be generated for serial exams.
2. List of t-numbers for the patient and patient directory.
3. Timelines for the t-numbers.

4. Clinical information, if available. (PFS, OS etc..)

Publishing Agreement

It is the policy of the University to encourage the distribution of all theses, dissertations, and manuscripts. Copies of all UCSF theses, dissertations, and manuscripts will be routed to the library via the Graduate Division. The library will make all theses, dissertations, and manuscripts accessible to the public and will preserve these to the best of their abilities, in perpetuity.

Please sign the following statement:

I hereby grant permission to the Graduate Division of the University of California, San Francisco to release copies of my thesis, dissertation, or manuscript to the Campus Library to provide access and preservation, in whole or in part, in perpetuity.

Ruting Wen

Author Signature

3/27/2015

Date